Isotope effects associated with soil production and uptake of molecular hydrogen

by

Qianjie Chen

Supervisors:

Prof. Thomas Röckmann & Dr. Maria Elena Popa

IMAU Institute for Marine and Atmospheric research Utrecht

Universiteit Utrecht

Abstract: Molecular hydrogen (H_2) is the second most abundant reduced gas in the atmosphere, but its biogeochemical cycle is not well understood. This thesis focuses on the soil production and uptake of H_2. The biogenic soil sink of molecular H_2 is the largest (~75% of total removal) and most uncertain term in the global atmospheric H_2 budget. With the large uncertainty, it is difficult to predict how atmospheric H_2 may respond to future changes in climate or anthropogenic emissions. The biological N_2 fixation on land is a poorly understood source of H_2, which contributes approximately 4% to the total source strength. Although it is globally a minor H_2 source, it has a large local effect on the isotopic composition of H_2, due to its very deuterium-depleted source signature. To constrain the biogenic source and sink, I collected air samples from a grass field at Cabauw and a forest site at Speuld in the Netherlands, and investigated the isotopic fractionation during H_2 soil uptake and the isotopic signature of H_2 emitted from the soil (δD_{soil}). The H_2 emitted from the soil is expected to be from the N_2 fixation within the soil. Our results show that the deposition velocity (v_d) is higher on Speuld forest soil than on Cabauw grassland. The fractionation constant α is 0.943±0.013 for Speuld forest soil and 0.977±0.051 for the Cabauw grassland. A positive correlation between α and v_d has been suggested in previous studies but is not found in our dataset. For selected experiments with strong emission and weak uptake of H_2, the isotopic composition of soil emitted H_2, δD_{soil}, obtained from a Keeling plot is -693±71‰. However, model calculations considering the influence of soil uptake on the Keeling plot suggests that this number may underestimate the actual δD_{soil}. An alternative mass balance approach suggests that the actual δD_{soil} emitted to the atmosphere varies over a range from -600‰ to +196‰. A possible reason could be strong fractionation during removal of H_2 in the soil before it escapes to the atmosphere, which should be investigated in future studies.

Keywords: hydrogen; soil production; soil uptake; fractionation constant; isotopic signature

Chapter 1
Introduction

1.1 H_2 in the atmosphere

The atmosphere, though very thin (~50 km to the top of the stratosphere) compared to the Earth's radius, is essential for the life on Earth in terms of energy and mass exchange. Its chemical composition determines climate and affects the health of humans, animals and plants. It consists of (in mol/mol) 78.08%nitrogen (N_2), 20.95% oxygen (O_2), 0.93% argon (Ar) and 0.04% trace gases including carbon dioxide (CO_2), methane (CH_4), hydrogen (H_2), nitrous oxide (N_2O), carbon monoxide (CO), ozone (O_3) etc. Fig. 1.1 shows the most abundant gases in the atmosphere as well as their relative quantities. Regardless of the small quantity in the atmosphere, the trace gases are the most active participants in atmospheric chemistry and climate variations. Among them, H_2 is the second most abundant reduced gas (after CH_4) and plays a notable role for the oxidative capacity of the atmosphere and stratospheric chemistry. The mole fraction of H_2 is about 530 parts per billion (ppb = nmole/mole) (Novelli et al., 1999; Price et al., 2007). The estimate for the lifetime of H_2 varies between 1.4 and 2.3 yr, and for the total atmospheric H_2 burden between 141 and 172 Tg (Ehhalt and Rohrer, 2009; Novelli, et al., 1999; Pieterse et al., 2011; Price et al., 2007; Rhee et al., 2006a; Xiao et al., 2007).

1.1.1 Global budget of H_2

In the present-day atmosphere, globally averaged H_2 mixing ratio is approximately 530 ppb. This number seems to be quite stable since 1920s (Ehhalt and Rohrer, 2009; Schmidt et al., 1974), though the sources of H_2 (CH_4 oxidation and fossil fuel combustion) have increased during the period. Recently, Petrenko et al. (2012) found a peak of H_2 mixing ratio during the 1970s and a decline during the following two decades from their Greenland firn air reconstruction, but they suggested that the results obtained by use of their reconstruction method might be unreliable. The reason why there is no long-term trend of tropospheric H_2 since 1920s is still unknown. It is possible that the increase of H_2 mixing ratio caused by the larger sources (CH_4 oxidation and fossil fuel combustion) was offset by the stronger soil uptake and OH scavenging of H_2. While the OH sink is well constrained, the soil sink has large uncertainty.

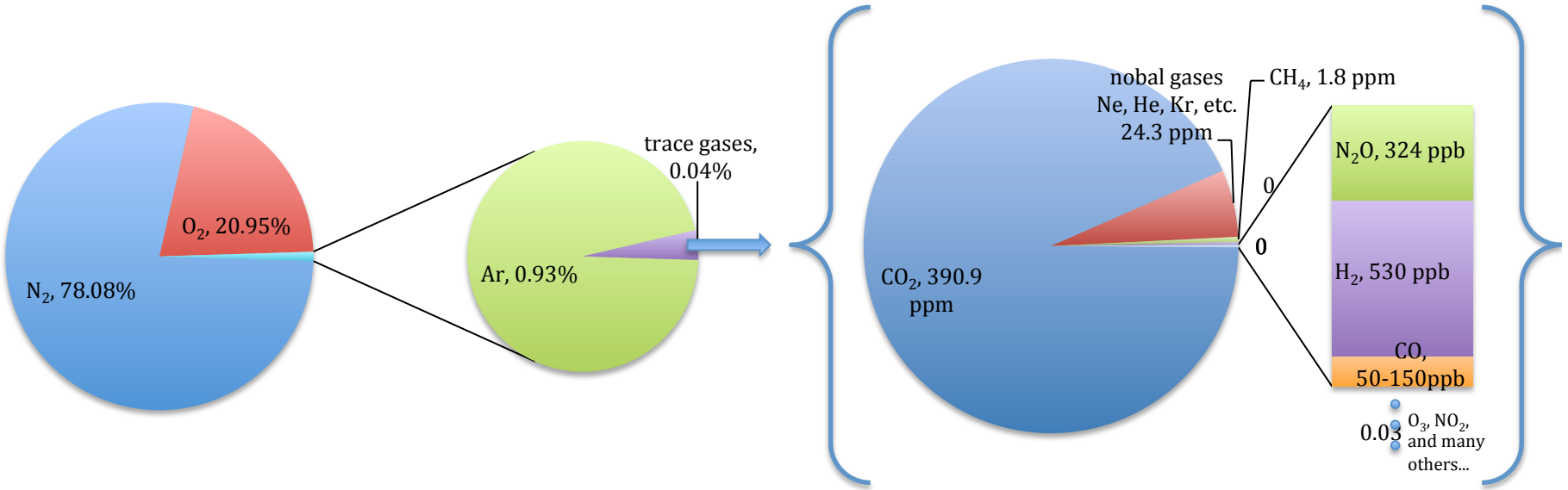

Fig. 1.1 The mixing ratio of gases in dry air, based on values provided in Jacob (1999), Price et al. (2007) and WMO (2010).

Temporal and spatial variability of H_2 mixing ratio were observed (Simmonds, et al, 2000; Novelli et al, 1999; Batenburg et al., 2011). The data published by Novelli et al. (1999) show the seasonal and spatial variation of H_2 for stations in both northern hemisphere (NH) and southern hemisphere (SH) from 1991 to 1996 (Fig. 1.2). In the northern hemisphere, the seasonal variation of H_2 is mainly governed by the soil uptake (Novelli et al., 1999; Pieterse et al., 2011). As a result, the maximum mixing ratio was found in late winter/early spring when the soil uptake is smaller and the minimum mixing ratio occurs in fall when the soil uptake is larger. In the southern hemisphere, the maximum mixing ratio occurred in late winter/spring while minimum mixing ratio occurred in late spring/early summer. The seasonal variation may be driven by tropical biomass burning, as suggested by the hydrogen isotopic composition studies by Batenburg et al. (2011) and Pieterse et al. (2011). Due to the soil uptake, the H_2 mixing ratios were typically lower in the NH than in the SH (Fig. 1.3). The highest annual average H_2 mixing ratio was found in the tropics and it drops sharply towards the Arctic as a result of the strong soil uptake in the NH while decreasing slowly towards Antarctica.

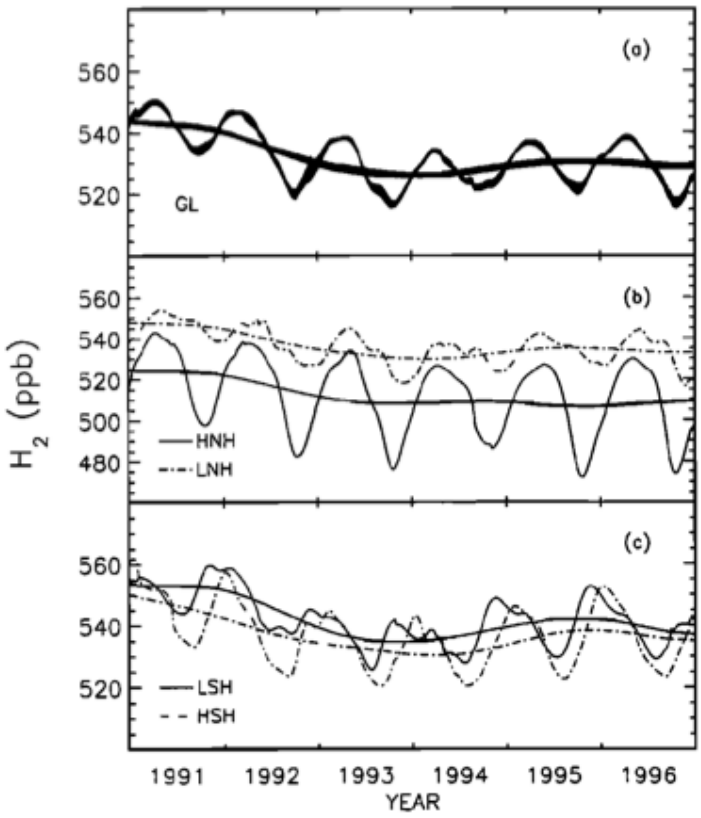

Fig. 1.2 Zonally averaged time series and trends of H_2 mixing ratio between 1991 and 1996 (Novelli et al., 1999). GL: global average; HNH: high northern hemisphere (45-90 °N); LNH: low northern hemisphere (0-45 °N); LSH: low southern hemisphere (0-45 °S); HSH: high southern hemisphere (45-90 °S).

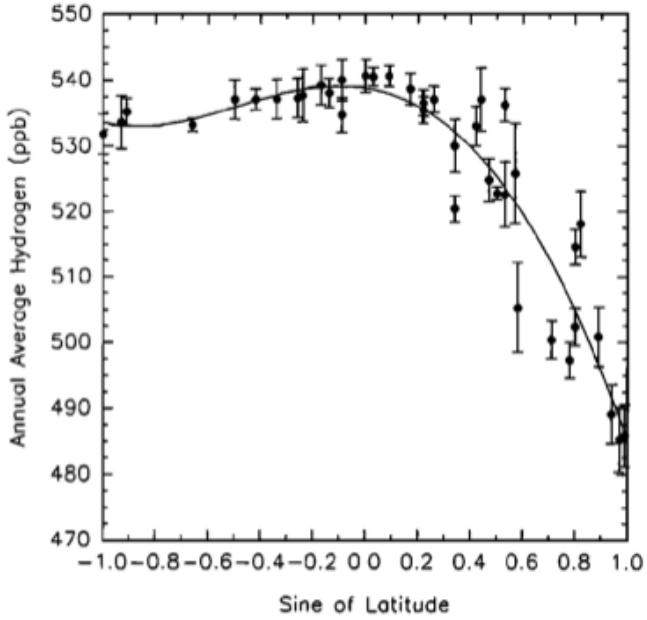

Fig 1.3 Annually averaged latitudinal gradient of H_2 mixing ratio during 1992-1995 presented by Novelli et al. (1999). Error bars represent the standard deviation of the four annual means.

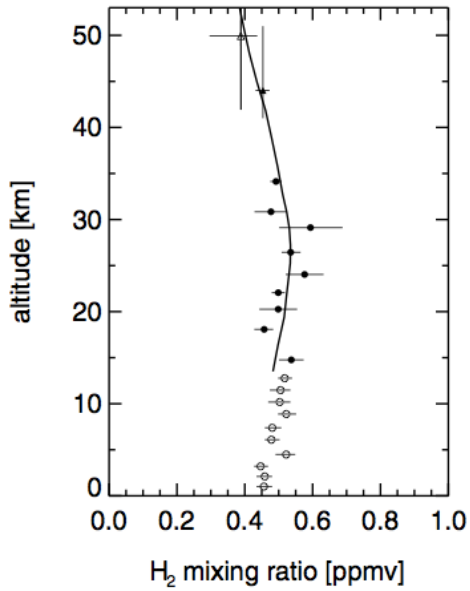

Fig. 1.4 Average vertical profile of H_2 mixing ratio in the troposphere and stratosphere presented by Ehhalt and Rohrer (2009). Full circles: Average over the measurements from 6 balloon flights between 1972 and 1975---most at Palestine, TX, 32◦N; one over Parana, Argentina, 30◦S. Open circles: Average tropospheric profile at the time, from aircraft flights. Open triangle: Result from a rocket flight on 24 September 1968. Full triangle: Result from a rocket flight on 23 May 1973. The vertical bars indicate the height interval of the rocket sampling. The error bars indicate the standard error of the measurement in the case of the rocket samples and the standard deviation of the mean in the case of balloon and aircraft samples. The heavy line is a hand drawn fit through the stratospheric data.

The vertical distribution of H_2 is quite uniform in both troposphere and stratosphere from most of the previous research (Ehhalt et al., 1977, 2009; Price et al., 2007; Schmidt et al., 1978), as shown in Fig. 1.4. However, there are some regions where strong vertical gradients of up to 10% exist in the troposphere (Ehhalt et al., 1977; Schmidt et al., 1978). Recently, Popa et al. (2011) showed the first in-situ, quasi-continuous long-term measurement series of vertical profiles of H_2 in the lower continental boundary layer, and suggested the vertical gradient of H_2 in the continental boundary layer is highly variable during short time scale because of the overlapping influences from soil uptake, anthropogenic emission, atmospheric transport and vertical mixing.

1.1.2 Sources and sinks of H_2

The sources and sinks of atmospheric H_2 were not identified until 1970s (Schmidt, 1974). Table 1.1 lists the H_2 budget estimates from different authors. The main sources of tropospheric H_2 are the oxidation of methane (~34%) and non-methane hydrocarbons (NMHC) (~18%), fossil fuel combustion (~18%) and biomass burning (~21%). Additional minor sources include biogenic N_2 fixation on land and in the ocean (Conrad and Seiler, 1980), volcanic emission (Sato et al., 1981; not shown), ocean degassing (Holloway and O'Day, 2000; not shown) and recently found abiotic degradation of organic material (Lee et al., 2012; not shown). For stratospheric H_2, which is not the focus here, 95% is transported from the troposphere and the oxidation of methane and NMHC constitutes a small source. Regarding the sinks, about three quarters of H_2 in the atmosphere is taken up by soil and one quarter consumed through the oxidation by OH. However, the sources and sinks presented have relatively large uncertainties, especially for the largest sink soil uptake (Table 1.1).

Table 1.1. The global budget of H_2 from different authors (Novelli et al., 1999; Rhee et al., 2006a; Price et al., 2007; Xiao et al., 2007; Ehhalt and Rohrer, 2009; Pieterse et al., 2011).

	Novelli et al. (1999)	Rhee et al. (2006a)	Price et al. (2007)	Xiao et al. (2007)	Ehhalt and Rohrer (2009)	Pieterse et al. (2011)
Sources (Tg yr^{-1})						
CH_4 oxidation	26±9	64±12	24.5	77±10	23 ± 8	37.3
NMHC oxidation	14±7	incl. above	9.8	incl. above	18 ± 7	incl. above
Fossil fuel	15±10	15±6	18.3	15±10	11 ± 4	17.0^{+3}_{-6}
Biofuels			4.4			
Biomass burning	16±5	16±3	10.1	13±3	15 ± 6	15.0±5
N_2 fixation, land	3±1	6±5	0		3±2	3.0±3
N_2 fixation, ocean	3±2	6±5	6		6±3	5.0^{+1}_{-2}
Sinks (Tg yr^{-1})						
Soil uptake (% of total sink)	56±41 (75%)	88±11 (82%)	55±8 (75%)	85±5 (82%)	60^{+30}_{-20}(76%)	55.8 (72%)
Oxidation by OH	19±5	19±3	18	18±3	19 ± 5	22.1
Tropospheric burden (Tg)	155±10	150[a]	141	149±23	155±10[b]	169[c]
Tropospheric lifetime (yr)	2.1	1.4	1.9	1.4	2.0	2.2[c]

[a] Calculated from sources and lifetime.
[b] From Novelli et al. (1999).
[c] The model domain for the budget calculation runs from the surface to 100 hPa. For the troposphere with a mass of 0.82 of the total atmosphere the burden would be 155 Tg H_2 and the lifetime 2.0 yr.

1.2 Effects on the atmosphere of a potential future hydrogen economy

The exploitation and combustion of fossil fuels (coal, petroleum, natural gas) have enhanced the concentration of greenhouse gases (CO_2 and CH_4), soot and sulfate in the atmosphere since the industrial revolution (IPCC, 2007), which draw the public attention to the global warming and air pollution issues. Consequently, scientists have been seeking for an alternative to fossil fuels to suppress the upward trend of greenhouse gases concentration in the atmosphere
as well as to prepare for potential energy shortage in the future. The only combustion product of H_2 is water (H_2O), which brings H_2 the fame of "clean" energy. Therefore, H_2 is proposed to replace fossil fuels to be an energy carrier (Ogden, 1999).

However, the environmental and climate impact of widespread use of H_2 as an energy carrier is still under assessment. In theory, if H_2 does not leak out during production, storage and transportation processes and it is perfectly combusted (all H_2 molecules oxidized into H_2O), the anthropogenic H_2 emission should be reduced after H_2 replacing fossil fuels, because fossil fuel combustion is a source of H_2. But on the basis of the current technology, leakage of H_2 is inevitable. Schultz et al. (2003) proposed atmospheric H_2 concentration to increase by 30~120% depending on the assumed leakage rate (3~10%), with the assumption that 50% of fossil fuel combustion at that time would be replaced by hydrogen technology. The impact on atmospheric chemistry and climate variation caused by the increase of H_2 in the atmosphere necessitates more research on the biogeochemical cycle of H_2, which is sparse at the moment.

H_2 can influence the atmospheric chemistry and composition in several ways. Firstly, though H_2 itself is not a greenhouse gas, it has an indirect greenhouse effect. In the atmosphere, H_2 is removed by reaction with the hydroxyl radical OH (Grenier, 1969; Schmidt, 1974), the "cleaning agent" in the atmosphere, as follows:

$$H_2 + OH\bullet \rightarrow H_2O + H\bullet \qquad \text{(R1)}$$

The reaction rate constant is well defined (Sander et al., 2006). Consequently, if we increase the H_2 concentration in the atmosphere by replacing fossil fuels with hydrogen fuel cells as suggested by Ogden (1999), then less OH are available for the removal of CH_4, which

increases the lifetime of the greenhouse gas CH_4 (Schultz et al., 2003; Warwick et al., 2004).

Secondly, the lifetime of the air pollutant CO would be longer and tropospheric O_3 concentration may increase since H_2 is a precursor of O_3 (R1-R5), which can further cause air quality and health issues.

$$H_2 + OH\bullet \rightarrow H_2O + H\bullet, \quad \text{(R1)}$$
$$H\bullet + O_2 \rightarrow HO_2\bullet \quad \text{(R2)}$$
$$HO_2\bullet + NO \rightarrow NO_2 + OH\bullet, \quad \text{(R3)}$$
$$NO_2 + O_2 + h\nu \rightarrow NO + O_3. \quad \text{(R4)}$$
$$\text{Net: } H_2 + 2\,O_2 + h\nu \rightarrow H_2O + O_3 \quad \text{(R5)}$$

But it should be noted that fossil fuel combustion is a large source of CO, O_3 and other air pollutants. The substitution of fossil fuels with hydrogen fuel cells would mean the reduction of fossil fuels and the associated air pollutants. Thus, whether replacing fossil fuels with hydrogen fuel cells will result in worse air quality depends on the amount of fossil fuel reduction and the method to produce H_2 (Jacobsen et al., 2005, 2008; Schultz et al., 2003; Warwick et al., 2004). The model simulation results shown by Schultz et al. (2003) suggested better air quality, by assuming that half of the fossil fuel is replaced by H_2 that is generated without producing other greenhouse gases or other air pollutants. However, Warwick et al. (2004) proposed that different scenarios of a hydrogen economy could result in different chemical composition of the troposphere. Jacobsen et al. (2008) suggested better air quality if all H_2 is to be generated by wind power.

In addition to the effects mentioned above, the water vapor (H_2O) produced through the oxidation of H_2 in the stratosphere can result in increase of humidity and cooling of the stratosphere. It will then lead to increased formation of polar stratospheric clouds and ozone depletion (Tromp, et al., 2003). But this effect may be weak (Warwick et al. 2004; Vogel et al., 2012) and is still under debate.

1.3 Soil uptake and production of H_2

The biogenic soil sink of molecular H_2 is the largest and most uncertain term (Table 1.1) in the global atmospheric H_2 budget, which contributes to around 75% to the total sink but with large uncertainty (Ehhalt and Rohrer, 2009; Hauglustaine and Ehhalt, 2002; Novelli et al., 1999;

Pieterse et al., 2011; Price et al., 2007; Rhee et al., 2006a; Sanderson et al., 2003; Xiao et al., 2007; Yashiro et al., 2011; Yver et al., 2011). With the large uncertainty, it is difficult to predict how atmospheric H_2 may respond to future changes in climate or anthropogenic emissions by the potential hydrogen economy.

Some efforts have been made during the past three decades to study the biochemical mechanism of H_2 soil uptake and to reduce the uncertainty. The sterilizing experiments of soil with high temperature carried out by Conrad and Seiler (1981) indicated that the soil uptake of atmospheric H_2 is caused by soil microorganism and/or soil enzymes. They suggested it is more likely that the free enzyme hydrogenase plays the dominant role since there were no bacteria found to be able to fix H_2 at atmospheric concentration at that time. This soil enzyme hydrogenase hypothesis was the basic hypothesis of many further soil uptake studies (Conrad et al., 1983; Conrad and Seiler, 1985; Ehhalt et al, 2011; Guo and Conrad, 2008; Häring et al., 1994; Smith-Downey et al., 2006).The hydrogenase enzymes catalyze the reversible oxidation of H_2 in the soil, following the reaction:

$$H_2 \Leftrightarrow 2H^+ + 2e^- \qquad \text{(R6)}$$

The H_2 soil uptake occurs within the upper few centimeters of the soil in the presence of oxygen (Conrad and Seiler, 1981; Conrad et al., 1983; Yonemura et al., 1999), and there seems to be an equilibrium concentration for H_2 soil uptake (Conrad, 1994; Conrad and Seiler, 1985; Schuler and Conrad, 1990; Conrad and Seiler, 1980), below which it is likely that the uptake ceases or is compensated by the soil production of H_2.Conrad (1994) suggested the equilibrium concentration for H_2 is compensation concentration (uptake compensated by production) rather than threshold concentration (uptake stops at some point and no production exists). In addition to enzymes, some microorganisms are able to decompose H_2. But most microorganisms found to utilize H_2 generally consume H_2 at high mixing ratio (hundreds of ppm) (Conrad, 1996). Constant et al. (2008) showed in their experiments the first aerobic microorganism (*Streptomyces* sp. PCB7) able to consume H_2 at tropospheric ambient concentration, and hypothesized that some bacterial strains such as streptomycetes could show high-affinity uptake of tropospheric H_2. This finding suggested that active metabolic cells are responsible for the soil uptake of H_2 rather than enzymes. Further, Constant et al. (2010) studied more streptomycetes strains isolated from temperate forest and agricultural soils, and their results showed that high-affinity H_2 uptake activity is widespread among the streptomycetes.

Hitherto, the exact mechanism of the H_2 soil uptake activity is still unknown.

One quantity to evaluate the strength of the soil uptake of H_2 is the deposition velocity v_d (unit: cm/s). The v_d is found to vary from 0.01 to 0.4 cm/s in different studies (Conrad and Seiler, 1980; Conrad and Seiler, 1985; Constant et al, 2008; Gerst and Quay, 2001; Hammer and Levin, 2009; Smith-Downey et al., 2008). Both microbial removal and diffusion can affect v_d, and the microbial removal activities and diffusion can be influenced by the temperature and moisture content of the soil. There are some studies showing that v_d depends on temperature, soil moisture and soil type (or ecosystem type) (Conrad and Seiler, 1981; Pieterse et al., 2011; Schmitt et al., 2009; Smith-Downey et al., 2006; Yashiro et al., 2011; Yonemura et al., 1999, 2000). But Conrad and Seiler (1985) suggested v_d is dependent on soil moisture but independent on soil temperature. Smith-Downey et al. (2008) found that temperature and soil type are not strong controllers of H_2 uptake, and the vertical distribution of H_2 uptake capacity and diffusive properties of soils that are dependent on soil moisture play the dominant roles. The soil moisture has multiple effects. When the soil is too dry, microbial activity is reduced and, hence the H_2 deposition velocity is smaller. However, deposition velocity can also be reduced when the soil is too wet, which reduces soil porosity. The optimal H_2 deposition velocity occurs at around 6%~11% (w/w) soil moisture (Conrad et al., 1981, Conrad and Seiler, 1985).

H_2 can be produced during the biological N_2 fixation process, for example by bacteria living symbiotically in the root nodules of legumes (Conrad and Seiler, 1980) such as clover, beans, peas and alfalfa. The overall biochemical reaction is shown:

$$\mathbf{N_2} + 8\ H^+ + 8\ e^- \rightarrow\ \ 2\ NH_3 + \mathbf{H_2} \qquad \text{(R7)}$$

Though most of the H_2 generated during this process is generally consumed by the bacteria in the soil, some is emitted into the atmosphere. Conrad and Seiler (1980) suggested that 2.4-4.9 Tg of H_2 is emitted into the atmosphere through N_2 fixation on land. This is the only estimated number from field and laboratory experiments published so far. Many authors use this number as a basic of their approximation of soil production of H_2 in their models and global H_2 budget assessment (Ehhalt and Rohrer, 2009, and the references therein; Novelli et al, 1999). The recent assessment estimates the source strength of this biogenic H_2 to be about 3 Tg yr^{-1} (Ehhalt et al., 2009), representing about 4% of the total source strength. Some estimates of the source strength of biogenic H_2 are

shown in Table 1.1. Although it is globally a minor H_2 source, it has potentially a large effect on the isotopic composition of H_2, due to its very deuterium-depleted source signature (Walter et al, 2011). Besides, as one alternative method to commercially produce H_2 is through microbial processes, the knowledge gained from the investigation of biogenic H_2 could help constrain the H_2 budget in the future.

1.4 Isotopic signature of production and uptake of H_2 by soil

1.4.1 Isotope basics

Isotopes are atoms that contain the same number of protons but differ in the number of neutrons. A chemical element can have more than one isotope. For example, in nature, hydrogen (one proton) has three isotopes including protium (^{1}H), deuterium (^{2}H or D) and tritium (^{3}H of T) that contain 0, 1, and 2 neutrons respectively. Sulfur (16 protons) has 25 known isotopes whose number of neutrons ranges from 14 to 37. Some isotopes are stable while some are radioactive. The term "stable" is relative, depending on the detection limits of the radioactive decay times. For hydrogen, H and D are stable isotopes while T is radioactive isotope. From now on, only the stable isotopes will be discussed.

The chemical behavior of an element is basically determined by its electronic structure, while the physical properties of the element are basically determined by its nucleus (Hoefs, 2009). The substitution of any atom in a molecule with one of its isotopes would result in a very small change in its chemical behavior. Therefore, different isotopologues generally undergo same chemical reactions and form same chemical compounds. However, the reaction rate coefficients can be different because of the mass differences of isotopologues, as a result of the quantum mechanical effects. In general, organisms also have a preference for certain (often the light) isotopologues. The effects caused by the mass difference of isotopologues make isotopic measurements very useful in atmospheric research. Isotope technics can be used in determining the sources, chemical processes and sinks of a chemical compound on the basic of its isotopic signature.

The isotopic composition of a substance is commonly expressed in isotopic δ-notation, which compares the isotopic ratio of the sample to the isotope ratio of a standard material. As an example, the isotopic composition for H_2 is expressed as:

$$\delta D = \frac{R_{sa}}{R_{VSMOW}} - 1$$

where R_{sa} is the D/H ratio of the sample and R_{VSMOW} is that of the standard material (Vienna) Standard Mean Ocean Water (VSMOW) with the D/H value of (155.76±0.8) ppm (de Wit et al.,1980; Gonfiantini et al., 1993).

1.4.2 Isotopic signature of sources and sinks of H_2

To better understand the sources and sinks of H_2, one possibility is to investigate the isotopic fractionation processes involved, which act as a fingerprint of H_2 for different sources and sinks. Due to the large mass difference between HH and HD (around 50%), the isotope effects are particularly large for H_2. The abundance of tritium products (HT, DT and TT) and DD are extremely small compared to that of HH and HD, and hence they are neglected in the rest of the thesis.

The deuterium content (δD) of H_2 in the atmosphere has been measured since the 1950s. Ehhalt et al. (1966) observed in for background atmospheric H_2 to be +80‰. Friedman et al. (1974) analyzed air samples collected from November 1967 to June 1969 and showed the δD for background atmospheric H_2 to be (+70±30)‰. Recent studies suggested that the global mean atmospheric δD is +120‰ ~ +130‰ (Batenburg et al., 2011; Gerst et al., 2000, 2001; Pieterse et al., 2011; Price et al., 2007; Rahn et al., 2003; Rhee et al., 2006a), which is higher than that in 1960s. The enrichment in deuterium content could be due to the increase in tropospheric CH_4 oxidation, which produced more deuterium-enriched H_2 (Gerst et al., 2001; Röckmann et al., 2003).

Table 1.2 shows the estimates of the isotopic signature of different sources and sinks of H_2 from different studies. These are mostly the isotopic signatures used in their models. Here we summarized the isotopic signature of different sources and sinks estimated by recent measurements. Röckmann et al. (2003) estimated the δD from CH_4 oxidation to be +180±50‰. The δD from VOCs oxidation is less well-constrained because of the diverse species of VOCs, and generally it is given the same δD as that from oxidation (Rahn et al., 2003). Gerst and Quay (2001) estimated globally the δD value from biomass burning could be -290±60‰. Röckmann et al. (2010) obtained more deuterium-depleted source signature and suggested that it is different for different combustion efficiency and different deuterium content of the local

precipitation. Recent estimate from the Amazonian tropical rainforest experiments by Haumann et al. (2013) suggested δD from tropical biomass burning is -280 ± 41‰. For the fossil fuels source, Rahn et al. (2002) found that the δD from traffic emission is -270‰ and Vollmer et al. (2012) found the δD from exhausts of different domestic heaters and waste incinerators is from -206‰ to -357‰. The removal fractionation factors α (=k_{HD}/k_{HH}, k_{HD} and k_{HH} are removal rate coefficient of HD and HH respectively) are 0.943±0.024 for soil uptake and 0.595±0.043 for OH oxidation respectively (Gerst and Quay, 2001), which makes it possible to distinguish soil uptake from OH oxidation with isotope techniques. In the stratosphere, the δD value for H_2 produced from CH_4 oxidation can reach +310‰ (Rhee et al., 2006b) or even up to +400‰ (Rahn et al., 2003; Röckmann et al., 2003).

1.4.3 Isotopic signature of soil production and uptake of H_2

As mentioned in Section 1.3, the uncertainty of soil uptake of H_2 is large. During the past decade, isotopic techniques started to be used in investigating the soil uptake of H_2 to reduce the uncertainty, but the studies were sparse. Table 1.3 summarizes the fractionation constant α_{soil} for soil uptake of H_2 given by previous studies. The fractionation constant α_{soil} refers to the ratio between the soil uptake rate constant of HD and that of HH. Gerst and Quay (2001) carried out the first field experiments in Seattle, United States and calculate the α_{soil} to be 0.943±0.024. Rahn et al. (2002) collected air samples from four forest sites with ecosystem of different ages in Alaska, United States in July 2001, and got a similar average value (0.94±0.01). They suggested that α_{soil} depends on the forest maturity, with larger α_{soil} for more mature forests. Since the more mature forests have larger deposition velocity of H_2, they further suggested lower uptake rates involve greater isotopic fractionation (smaller α_{soil}) than fast uptake rates. Rice et al. (2011) measured the deuterium content of the samples collected in Seattle during February, March and June 2006, and calculated α_{soil} to be 0.943±0.005 with considerable variability, which was consistent with the previous studies. They found α_{soil} to be correlated with deposition velocity, with smaller isotope effects (larger α_{soil}) occurring at higher deposition velocity, which agreed with the suggestion by Rahn et al. (2002). Hitherto, only α_{soil} values from the studies in Seattle and Alaska are available, and values from other locations and ecosystems are needed to learn more about the factors influencing α_{soil}. Additionally, some authors estimated α_{soil} in their model simulations, which are 0.943 (Rhee et al., 2006a), 0.943 (Price et al., 2007) and 0.925

(Pieterse et al., 2011). It seems that 0.94 is the most accepted value for α_{soil} at the moment.

The biological N_2 fixation on land is a poorly understood source of H_2 and contributes approximately 4% of the total source strength (Conrad and Seiler, 1980). Although it is globally a minor H_2 source, it has potentially a large effect on the isotopic composition of H_2, due to its very deuterium-depleted source signature. During the N_2 fixation, H_2 is produced biochemically in the aqueous phase in the microbes.

Therefore, we expect that the isotopic composition of the H_2 produced during N_2 fixation is related to the thermodynamic isotope equilibrium between H_2 and H_2O, similar to other biogenic sources (Bottinga et al., 1969; Walter et al., 2011). Bottinga et al. (1969) calculated theoretically the fractionation constant $\varepsilon_{H^2\text{-}H^2O}$ $(=(D/H)_{H^2}/(D/H)_{H^2O}\text{-}1)$ of H_2 relative to H_2O for this equilibrium to be between -737‰ and -693‰ for temperatures ranging from 10 to 40 °C. Thus in isotope equilibrium, D in H_2 is depleted by about –700‰ relative to the H_2O. Few measurements of various biogenic sources were conducted to confirm this calculation. Rahn et al. (2002) measured δD of -778‰ for headspace samples from a jar of termites and -690‰ for a headspace sample from a eutrophic water pond. Walter et al. (2011) studied headspace samples taken from 5 pure cultures of known H_2-producing organisms as well as a large number of biogas production experiments, and found an overall isotopic signature of biogenic H_2 to be -712±13‰. Recent models use a δ-signature of biogenic H_2 of -700‰ (Rhee et al., 2006a) or -628 ‰ (Pieterse et al., 2011; Price et al. 2007) in their simulations.

Table 1.2 Estimates of isotopic signature for different H_2 sources and sinks by different authors.

	Gerst and Quay (2001)	Rhee et al. (2006a)	Price et al. (2007)	Pieterse et al. (2011)
Source signature (‰)				
CH_4 oxidation		+190	+162±57	+116
NMHC oxidation		incl. above	+162±57	incl. above
Fossil fuel	-196±10	-270	-196	-196^{+10}_{-74}
Biofuels			-290	
Biomass burning	-290±60	-90	-290	-260±60
N_2 fixation, land		-700		-628^{+0}_{-72}
N_2 fixation, ocean		-700	-628	-628^{+0}_{-72}
Sink fractionation factor (k_{HD}/k_{HH})				
Soil uptake	0.943±0.024	0.943±0.007	0.943	0.925
Oxidation by OH	0.606±0.019, 0.595±0.043	0.58±0.07	0.568	0.524
Global average (‰)	+130±4	+126	+130	+128

Table 1.3 Estimates of soil uptake fractionation factor by different authors.

	Gerst and Quay, 2001	Rahn et al., 2002	Rhee et al., 2006a	Price et al., 2007	Rice et al., 2011	Pieterse et al., 2011	This work
Fractionation factor $\alpha_{soil}(=k_{HD}/k_{HH})$	0.943±0.024	0.94±0.01	0.943±0.005	0.943	0.943±0.005	0.925	0.943±0.013

Chapter 2
Experimental

2.1 Sampling

2.1.1 Sampling sites description

Air samples were collected from a soil chamber at two locations in the Netherlands: a grass field (Cabauw) and a forest site (Speuld). Two types of ground cover, with and without clover, were sampled at Cabauw; while three types of forest (Douglass fir, beech and spruce) were selected in Speuld.

The Cabauw site (Fig. 2.1) is a flat region consisting mainly of grasslands separated by ditches. Samplings were conducted on a grass field close to the Cabauw Tower (51°58'N, 4°55'E). The surroundings about 200 meters away consist of scattered villages, orchards, and a line of trees. The vegetation cover at our sampling site is close to 100% all year round with grass species *Loliumperenne* (55%), *Festucapratense* (15%), *and Phleümpratense* (15%) (Beljaars and Bosveld, 1997). Clover, belonging to legumes (plant order Leguminosae) that provide place for bacteria to fix N_2 (Burns and Hardy, 1975), was found in our sampling site. The soil consists in the top 60 cm of river-clay overlying a thick layer of peat. Jager et al. (1976) described the vertical structure of the soil in Cabauw as follow:

- 0-3 cm is the turf zone
- 3-18 cm is 35%-50% clay (particles ≤2 μm) and 8%-12% organic matter with high root density
- 18 - 60 cm is 45%-55% clay (particles ≤2 μm) and 1%-3% organic matter with low root density
- 60 - 75 cm is a mixture of clay and peat
- 75 - 700 cm is peat

More information on the Cabauw site, soil and vegetation type, and physical soil properties can be found in Beljaars and Bosveld (1997), Jager et al. (1976) and Wösten et al. (1994).

The Speuld forest site (52°13'N, 5°39'E) (Fig. 2.1) is located in the center of the Netherlands. It is a mature plantation of Douglas fir and other species such as beech and spruce. Different species are separated into

different zones. The soil is a well-drained Typic Dystochrept or Cambic Podzol on heterogeneous sandy loam and loamy sand textured ice-pushed river sediments (Heij and Erisman, 1997 and the references therein). The Speuld forest has a high foliage mass and an extremely high ratio of foliage to fine root mass, and is deficient with respect to phosphate and has high nitrogen concentration in the foliage (Heij and Erisman, 1997).

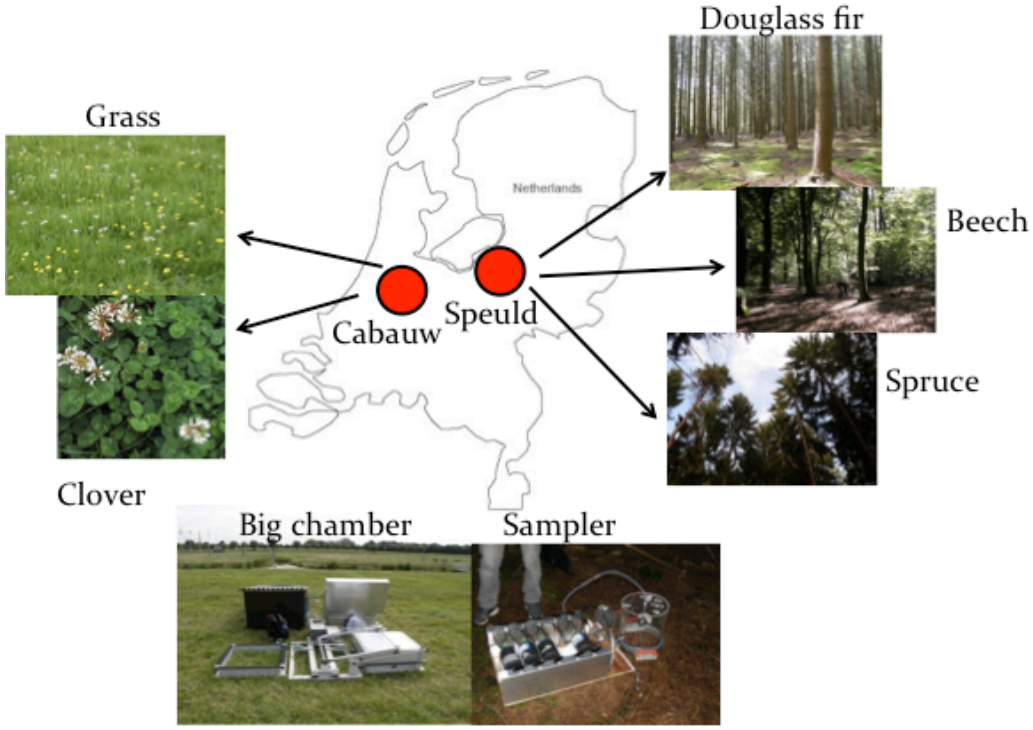

Fig. 2.1 The locations of two sampling sites (Cabauw and Speuld) as well as their plant species.

2.1.2 Sampler and sampling procedure

The closed-cycle air sampler to collect air samples was designed and constructed at the IMAU (Institute for Marine and Atmospheric research Utrecht) (Fig. 2.2). It consists of one soil chamber (22.8 L), four flasks (1 L each), one pump, one tube filled with magnesium perchlorate ($Mg(ClO_4)_2$) to dry the air, one pore-size particle filter, some two-position valves, one fan to mix the air inside the chamber, two pressure gauges, and one rotameter to control and observe the flow rate. The soil chamber consists of two parts: one metal base inserted ~2 cm into the soil, and a removable transparent lid with two connections for air sampling.

Air samples were collected from the chamber in 1 L glass flasks at 0, 10, 20 and 30 minutes after closing the chamber lid (time interval changed to 5 min in Speuld).

A set of four flasks is installed in series. In the beginning, the whole sampling unit (all lines, connections and flasks) is flushed with ambient air for about 10 minutes at a flow rate of 2 L/min, with all flasks open and the chamber lid open. Air flows from the chamber through the $Mg(ClO_4)_2$ tube before entering the flasks. This initial flushing process is designed to fill the flasks with background air. The necessary flushing time was calculated by assuming "perfect mixing" inside the chamber and flasks (Chen et al., 2012). More information about the flushing time calculation can be found in Section 2.2. The air pressure inside the flasks is increased to 2 bar (1.8 bar for Speuld samples) before chamber closing and then maintained constant during the whole sampling time. After the flushing process, the first flask is closed and then the chamber lid is as well. From now on, the air goes from the chamber through three flasks (the first flask is by-passed) and back to the chamber. After 10, 20 and 30 minutes, the second, third and fourth flasks are collected. In the end, the set of four flasks is stored and sent to IMAU for H_2 isotopic composition measurements.

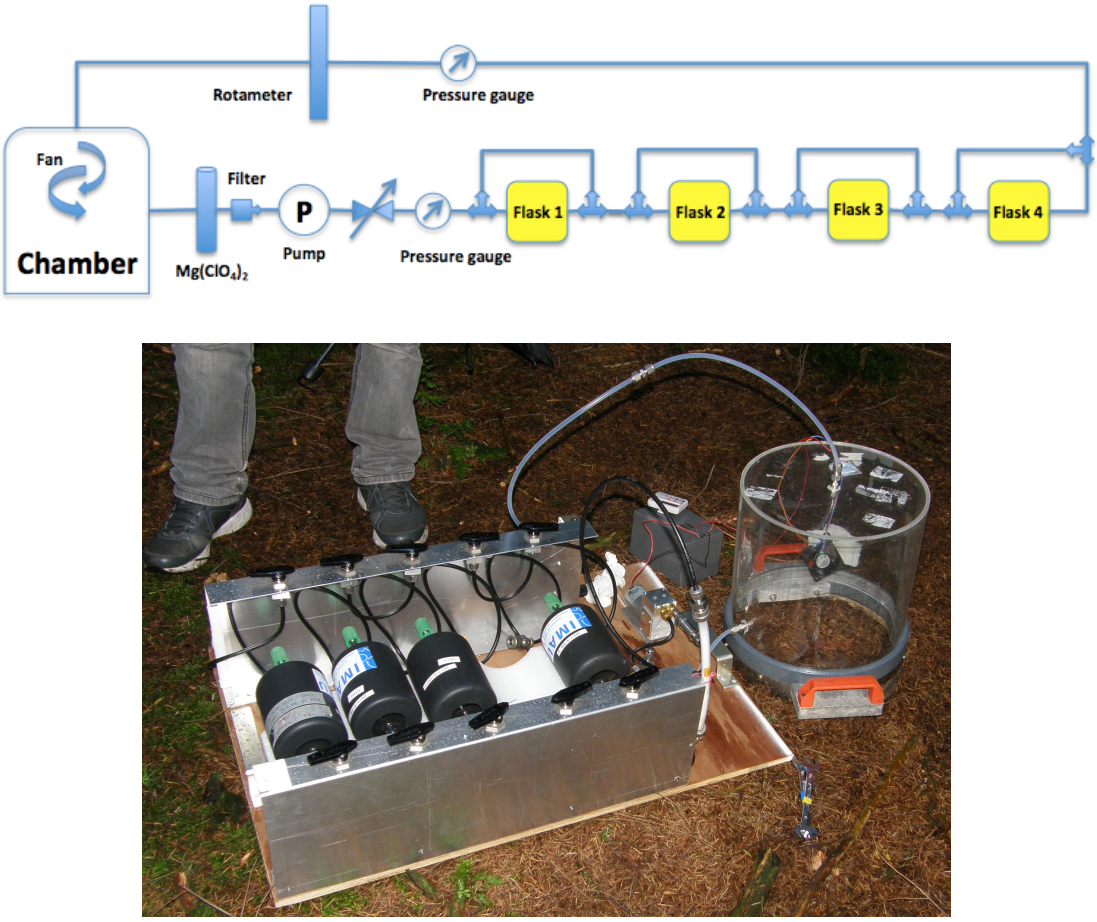

Fig. 2.2 Samper structure. The chamber is 22.8 L and each flask is 1 L in volume.

There were 36 sets of air samples collected in Cabauw during summer (June, July and August) 2012 and 12 sets collected in Speuld in September 2012. Each set contains four air samples. In total, 176 valid samples (4 were lost during sampling, transportation and measurement) were analyzed for H_2 mixing ratio and its deuterium content, which generated the largest data set for soil hydrogen isotopes studies so far.

Most experiments were conducted with a small chamber, which is 22.8 L in volume and 40 cm in height. Ten experiments were conducted with a large chamber that is 125 L in volume and 22.5 cm in height. These experiments have the following identification numbers: "CBW-4", "CBW-5", "CBW-7", "CBW-10", "CBW-14", "CBW-21", "CBW-23", "CBW-27", "CBW-30" and "SPU-6".

2.2 Model to simulate the flask sampling processes

2.2.1 Mathematical description of sampling

First, a simple method of obtaining the soil production rate (P) and uptake rate constant (k) of H_2 inside the chamber is introduced here. Based on the mass balance of HH, the time evolution of its mixing ratio inside the chamber can be expressed as:

$$\frac{\mathrm{d\,c}}{dt} = \mathrm{P} - \mathrm{kc} \qquad (1)$$

where c is the mixing ratio of H_2, P is the production rate and k is the uptake rate constant of H_2, respectively. The k is equivalent to v_d/h, where v_d is the deposition velocity of H_2 and h is the chamber height. Here it is assumed that the production rate of H_2 is constant during each sampling and the uptake rate is first-order dependent on the mixing ratio of H_2 at time t. The solution of Eq. (1) is of the form:

$$\mathrm{c} = (c_i - c_e)e^{-kt} + c_e \qquad (2)$$

where c, c_i and c_e (= P/k) are the mixing ratio of H_2 at time t, initially and at equilibrium, respectively.

Therefore, if we apply the exponential function of Eq. (2) to the time evolution of H_2 inside the chamber, then we can get P and k. The data for time evolution of H_2 can be obtained by collecting instant air samples at different time t inside the chamber. In order to have representative data,

the amount of air samples taken out of the chamber should be very small compared to the chamber volume so that the air density inside the chamber does not change, and the amount of time for collecting each sample should be very small so that we can assume H_2 mixing ratio does not change during each collection period.

However, in our case the volume of air inside the flasks (8 L of air in total) is considerable compared to the volume of air inside chamber (22.8 L). This will have two effects: (1) A significant part of the air is at each time separated from the chamber and thus from the soil production and uptake so that the total air volume is not well mixed. (2) Because of the time lag to fill the samples, the air in a flask is not the same as the air in the chamber at the same time. Therefore, it is necessary to evaluate how significant these effects will be. In this section, I present mathematical calculations and model results to give more information about the sampling and evaluate the influence of sampling processes on uptake rate constant (k) and production rate (P) calculation.

(i) Flushing: background air in the 1st flask

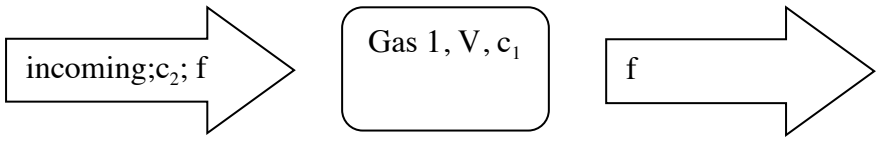

The incoming gas with mixing ratio c_2 enters the flask at flow rate f to mix with "Gas 1" with initial mixing ratio c_1. Assuming perfect mixing (Chen et al., 2012) in the flask, the mass balance relation yields:

$$\frac{d(c\,V)}{dt} = c_2\,f - c\,f \qquad (3)$$

where c is the mixing ratio for a specific gas such as CO_2, O_3 and H_2 in the flask at time t. The solution is of the form:

$$c(t) = (c_1 - c_2)e^{\frac{-f}{V}t} + c_2 \qquad (4)$$

This can be solved for the time required to exchange a certain fraction of the initial gas with the incoming gas.

$$t = \frac{-V}{f} ln \frac{c - c_2}{c_1 - c_2} \qquad (5)$$

For our sampling with f = 2 L/min and V= 2 L of air (1 L flask with 2 bar pressure), we obtain the following time intervals necessary for different proportions of incoming gas that contribute to the total volume of gas inside the flask.

① 90% mixing (c = 90% c_2+10% c_1)
t = 2.3 min = 138s

② 98% mixing (c = 98% c_2+2% c_1)
t = 3.9 min = 235s

③ 99.995% mixing (c = 99.995% c_2+0.005% c_1)
t = 9.9 min = 594s

Thus, after 10 minutes of flushing, the air inside the four flasks should essentially represent the background air.

(ii) Time evolution of the flask samples

Here we denote $c_1(t)$, $c_2(t)$, $c_3(t)$, $c_4(t)$ and $c_0(t)$ the H_2 mixing ratio for the first, second, third, forth flask and the chamber, respectively. After 10 min flushing process of the chamber and the flasks as described above, they contain background air with the H_2 mixing ratio c_1. At this moment (considered t=0) the first flask is by-passed and the chamber lid is closed. Then only the chamber, the second, third and fourth flask are connected, and the initial H_2 mixing ratio inside them is c_1.

The time evolution for the second flask can be expressed as:

$$\frac{dc_2}{dt} = \frac{f}{V}c_0 - \frac{f}{V}c_2 \qquad (6)$$

Similarly, for the third flask:

$$\frac{dc_3}{dt} = \frac{f}{V}c_2 - \frac{f}{V}c_3 \qquad (7)$$

For the fourth flask:

$$\frac{dc_4}{dt} = \frac{f}{V}c_3 - \frac{f}{V}c_4 \qquad (8)$$

For the chamber:

$$\frac{dc_0}{dt} = \frac{f}{V'}c_4 - \frac{f}{V'}c_0 + (P - kc_0) \qquad (9)$$

where V and V' are the air volumes of the flask and chamber, and f is the flow rate.

The solution for Eq. (6) is:

$$c_2(t) = \left(\int \frac{f}{V}c_0(t) * e^{\frac{f}{V}t}dt + c_1\right) * e^{\frac{-f}{V}t} \qquad (10)$$

Similarly, solutions for Eq. (7), (8), (9) are:

$$c_3(t) = \left(\int \frac{f}{V}c_2(t) * e^{\frac{f}{V}t}dt + c_1\right) * e^{\frac{-f}{V}t} \qquad (11)$$

$$c_4(t) = \left(\int \frac{f}{V}c_3(t) * e^{\frac{f}{V}t}dt + c_1\right) * e^{\frac{-f}{V}t} \qquad (12)$$

$$c_0(t) = \left(\int (\frac{f}{V'}c_4(t) + P) * e^{(\frac{f}{V'}+k)t}dt + c_1\right) * e^{(\frac{-f}{V'}+k)t} \qquad (13)$$

Then the second flask is closed, and only the chamber, the third and fourth flask are connected, and the initial H_2 mixing ratio inside them is c_0(t=10), c_3(t=10) and c_4(t=10) respectively.

Then, the time evolution for the third flask can be expressed as:

$$\frac{dc_3}{dt} = \frac{f}{V}c_0 - \frac{f}{V}c_3 \qquad (14)$$

Similarly, for the fourth flask:

$$\frac{dc_4}{dt} = \frac{f}{V}c_3 - \frac{f}{V}c_4 \qquad (15)$$

For the chamber:

$$\frac{dc_0}{dt} = \frac{f}{V'}c_4 - \frac{f}{V'}c_0 + (P - kc_0) \quad (16)$$

The solutions for Eq. (14-16) are:

$$c_3(t) = \left(\int \frac{f}{V}c_0(t) * e^{\frac{f}{V}t}dt + c_3(t=10)\right) * e^{\frac{-f}{V}t} \quad (17)$$

$$c_4(t) = \left(\int \frac{f}{V}c_3(t) * e^{\frac{f}{V}t}dt + c_4(t=10)\right) * e^{\frac{-f}{V}t} \quad (18)$$

$$c_0(t) = \left(\int (\frac{f}{V'}c_4(t) + P) * e^{\left(\frac{f}{V'}+k\right)t}dt + c_0(t=10)\right) * e^{(\frac{-f}{V'}+k)t} \quad (19)$$

Then the third flask is closed, and only the chamber and the fourth flask are connected, and the initial H_2 mixing ratio inside them is c_0(t=20) and c_4(t=20) respectively.

Then, the time evolution for the fourth flask can be expressed as:

$$\frac{dc_4}{dt} = \frac{f}{V}c_0 - \frac{f}{V}c_4 \quad (20)$$

Similarly, for the chamber:

$$\frac{dc_0}{dt} = \frac{f}{V'}c_4 - \frac{f}{V'}c_0 + (P - kc_0) \quad (21)$$

The solutions for Eq. (20-21) are:

$$c_4(t) = \left(\int \frac{f}{V}c_0(t) * e^{\frac{f}{V}t}dt + c_4(t=20)\right) * e^{\frac{-f}{V}t} \quad (22)$$

$$c_0(t) = \left(\int (\frac{f}{V'}c_4(t) + P) * e^{\left(\frac{f}{V'}+k\right)t}dt + c_0(t=20)\right) * e^{\left(\frac{-f}{V'}+k\right)t} (23)$$

The H_2 mixing ratio inside the chamber and the fourth flask at time t=30 minutes is c_0(t=30) and c_4(t=30).

In the end, a set of four data (c_1(t=0), c_2(t=10), c_3(t=20) and c_4(t=30) is obtained, corresponding to a set of H_2 mixing ratio in the first, second, third and fourth flask from our samplings. By fitting this set of four data

with an exponential function (Eq. (2)), we can obtain the apparent soil uptake rate constant (k_{app}) and production rate (P_{app}). It is difficult to calculate $c_2(t=10)$, $c_3(t=20)$ and $c_4(t=30)$) from Eq. (6-23) analytically. Thus, I made a model with Matlab to simulate the sampling process with infinitesimal time step. The simulation codes are based on Eq. (6-23). Fig. 2.3 shows an example of the model results (k=0.1 min^{-1}, P=100 ppb min^{-1} and $c_1(t=0)$=530 ppb): the evolution of H_2mixing ratio in chamber ($c_0(t)$), in flask 2 ($c_2(t)$), flask 3 ($c_3(t)$) and flask 4 ($c_4(t)$) as a function of time, and what would be expected for a chamber without flasks. The H_2 mixing ratio of the flask 1 is c_1=530 ppb. There is a time lag compared to the situation without flasks for both the chamber and the flasks after introducing four flasks in the model. The time lag for the second flask is about 2.5 minutes. It increases to 5 minutes for the third flask and even longer for the fourth flask.

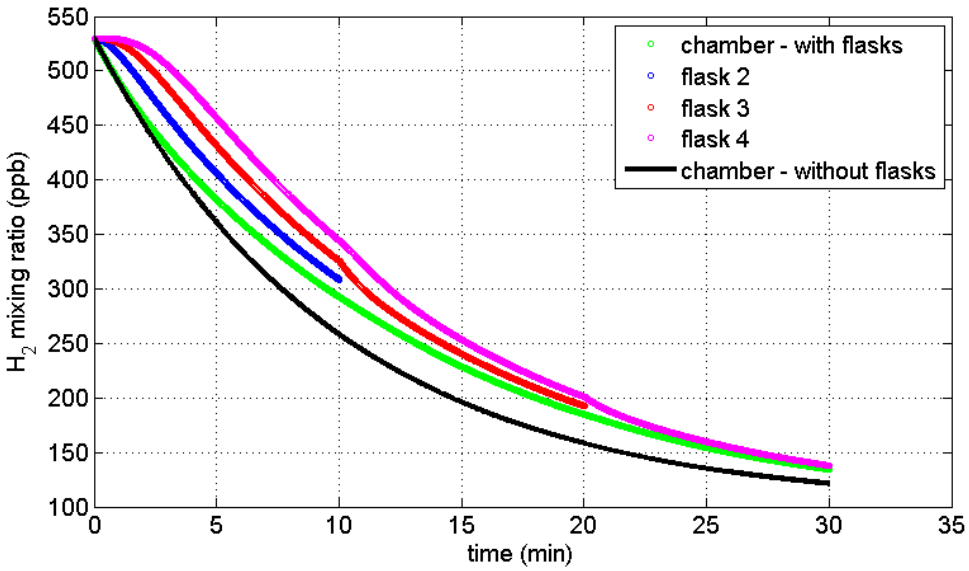

Fig. 2.3 Results of the flask sampling model (k=0.1 min^{-1}, P=100 ppb min^{-1} and $c_1(t=0)$=530 ppb): evolution of H_2 mixing ratio in chamber ($c_0(t)$) (green curve), in flask 2 ($c_2(t)$) (blue curve), flask 3 ($c_3(t)$) (red curve) and flask 4 ($c_4(t)$) (magenta curve) as a function of time, and what would be expected for a chamber without flasks (black curve).

2.2.2 Derivation of the true uptake rate constant from sample flasks

When samples are collected with the analytical system described above, the time evolution of mixing ratio and isotope value in the chamber and in the flasks is different, and it is not the same as what would be observed in the same chamber without the flask sampling (Fig. 2.3). In our simulations, each set of k (actual uptake rate constant), P (actual production rate) and c_1 (initial mixing ratio) generate four data points for

four flasks after closing the flasks at 0, 10, 20 and 30 minutes (5 minutes interval for Speuld samplings). These four points can be evaluated as shown above with the exponential function (Eq. (2)), which yields an apparent uptake rate coefficient k_{app} and an apparent production rate P_{app}, which are different from the actual k and P that operate in the chamber only (Fig. 2.3). Our aim is to find out how k_{app} and P_{app} are related to actual k and P, so that actual k and P can be derived from k_{app} and P_{app}.

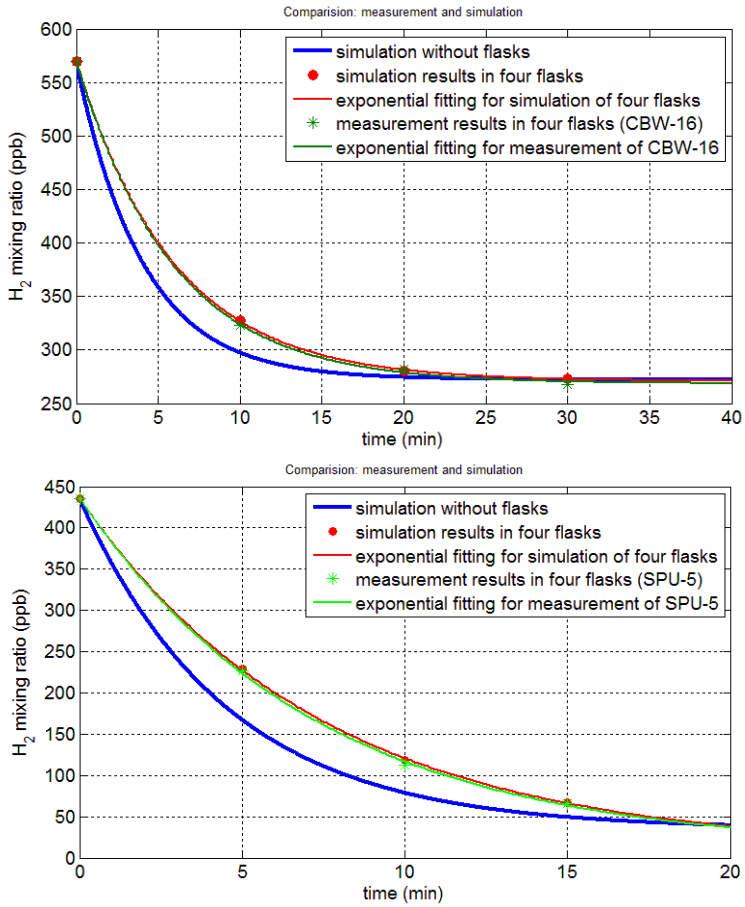

Fig. 2.4a-b Two examples of results from the flask sampling model, one from Cabauw (CBW-16) and one from Speuld (SPU-5). Green asterisks: the experimental results of H_2 concentration for the four flasks; the exponential fit to the data is shown as green curve. Red circles: the model simulation results in the flasks after applying Eq. (24-27) to derive k_{exp} and P_{exp} with exponential fit (red curve). Blue curve: time evolution of H_2 concentration inside the chamber without flasks with the reconstructed actual k and P.

Here we discuss the derivation of the function that expresses the relation between k and k_{app} for Cabauw experiments. As indicated in Section 2.2.1, the difference between k_{app} and k, P_{app} and P can be large since the air volume inside the flasks (8 L) is considerable compared to the air volume of the chamber (22.8 L). Fig. 2.4a shows one of the simulation results of the time evolution of H_2 mixing ratio inside the chamber without flasks (blue curve) with an initial H_2 mixing ratio (c_1) of 570 ppb, k = 0.246

min^{-1} and P = 67 ppb min^{-1} (this k corresponds to deposition velocity of 0.164 cm s^{-1} and P corresponds to emission flux of 1.1 μmol min^{-1} m^{-2}) as well as the simulation results of four flasks after introducing the flasks into the model (red curve). The calculated k_{app} and P_{app} are 45 ppb $min^{-1}$and k = 0.169 min^{-1}. By running the model with a wide range of values for k and P, a database can be built up, where each set of k_{app}, P_{app} and c_1 corresponds to a specific set of k, P and c_1.

Fig. 2.5 shows the relationship between k_{app} and k when P=10 ppb min^{-1} and c_1=500 ppb: $k=1.145k_{app}^2+1.203k_{app}+0.013$. For a fixed initial mixing ratio c_1 (500 ppb) and different P between 0 and 400 ppb min^{-1}, k and k_{app} fit very well with a quadratic function (Fig. 2.6). The coefficients in the function do not significantly depend on P and the overall function is: $k=1.148k_{app}^2+1.203k_{app}+0.013$. Fig. 2.7 assesses the influence of initial mixing ratio c_1 on the relation between k and k_{app}. When P is fixed, which is 10 ppb min^{-1} here as an example, the functions for different initial mixing ratio from 200 to 700 ppb show almost the same result, with an overall fitting function $k=1.146k_{app}^2+1.203k_{app}+0.013$. Thus, the function for the uptake rate constant is independent of P and initial c_1.

In conclusion, the relation between actual uptake rate coefficient k and apparent uptake rate coefficient k_{app} used in this thesis is:

$$k = 1.15k_{app}^2 + 1.20k_{app} + 0.01 \qquad (24)$$

It should be noted that the first term on the right hand side of the equation $1.15k_{app}^2$ is one order of magnitude smaller than the second term $1.20k_{app}$, since k_{app} from our experiments is about 0.1 min^{-1}. Therefore, the actual uptake rate coefficient k is about 20% higher than the k_{app} obtained from the four-flask experiment. This function is valid for both HH and HD. For Speuld samples that are collected at 5-minute time interval rather than 10 minutes, the correction function is found to be:

$$k_{SPU} = 0.95k_{app}^2 + 1.28k_{app} + 0.03 \qquad (25)$$

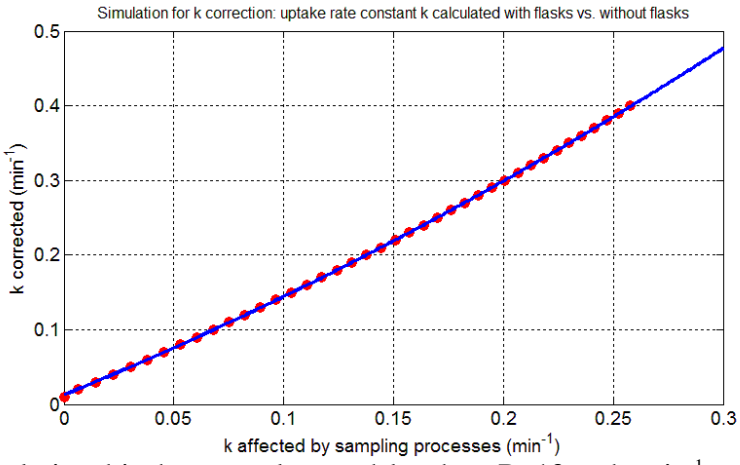

Fig. 2.5 The relationship between k_{app} and k when P=10 ppb min^{-1} and c_1=500 ppb. The correction function for k_{app} is: $k=1.145k_{app}^2+1.203k_{app}+0.013$.

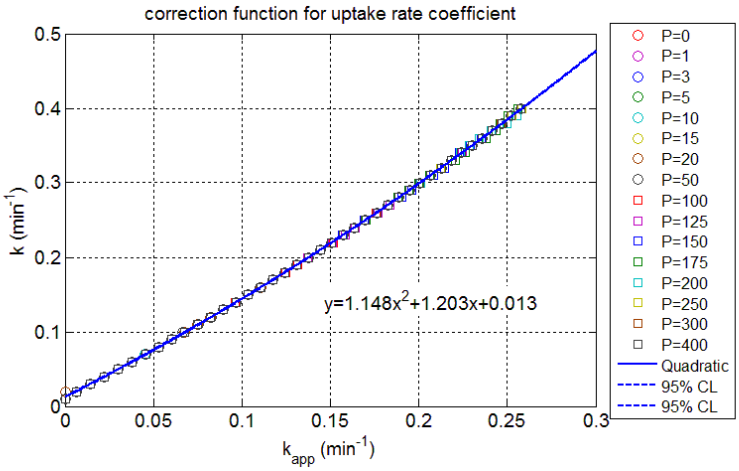

Fig. 2.6 The relationship between k_{app} and k when c_1=500 ppb and P varies from 0 to 400 ppb min^{-1}. The correction function for k_{app} is: $k=1.148k_{app}^2+1.203k_{app}+0.013$.

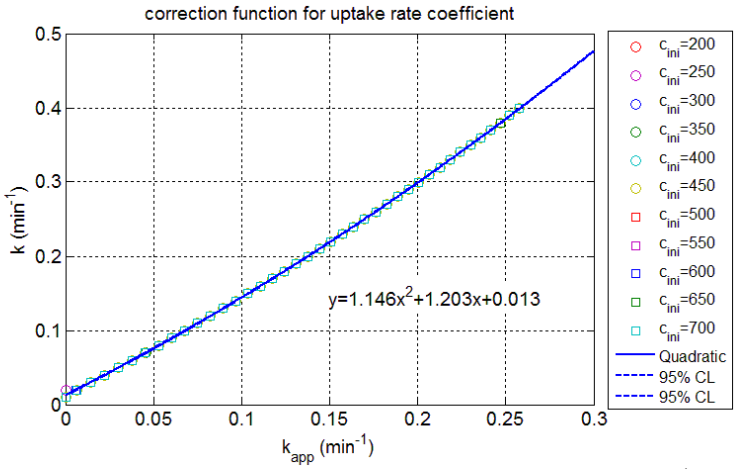

Fig. 2.7 The relationship between k_{app} and k when P=10 ppb min^{-1} and $c_1$varies from 200 to 700 ppb. The correction function for k_{app} is: $k=1.146k_{app}^2+1.203k_{app}+0.013$.

2.2.3 Derivation of the true production rate from sample flasks

Similar to the derivation of the correction function of k and k_{app}, this section discusses that for P and P_{app}. At first, we discuss the derivation of the function that expresses the relation between P and P_{app} for Cabauw experiments. Fig. 2.8 shows the relationship between P_{app} and P when c_1=400 ppb and k varies from 0.02 to 0.4 min^{-1}. P and P_{app} show linear correlation, but the linear correction functions ($P=a\times P_{app}+b$) are slightly different for different k, with different slope "a" and intercept "b". The slope "a" is found to depend on k only, with the relation: $a=0.768k^2+0.112k+1.386$ (Fig. 2.9). The intercept "b" depends on both uptake rate coefficient k and initial mixing ratio c_1. It decreases exponentially with k, with the function: $b = 5.176e^{-9.469k}$ (Fig. 2.10) when c_1= 400 ppb. For different c_1, b can be calculated as: $b_{c_1} = \frac{c_1}{400} 5.176e^{-9.469k}$ (Fig. 2.10 and Fig. 2.11).

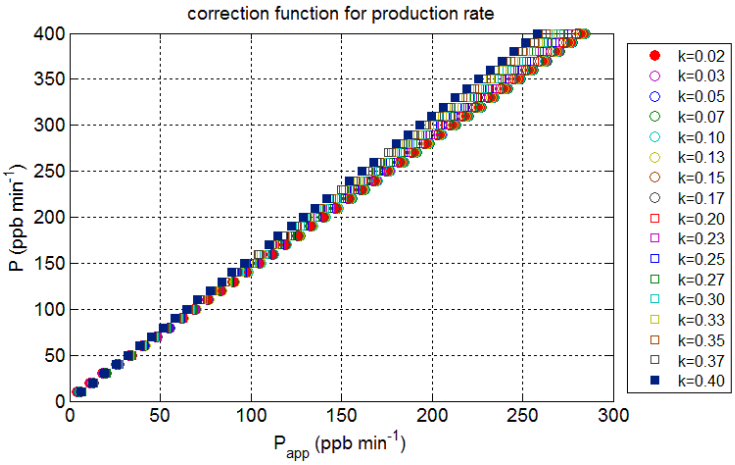

Fig. 2.8 The relationship between P_{app} and P when c_1=400 ppb and k varies from 0.02 to 0.4 min^{-1}.

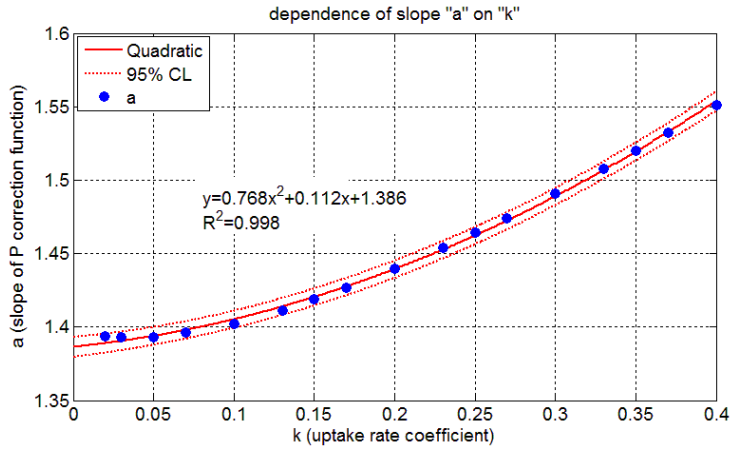

Fig. 2.9 The relationship between slope "a" of the P correction function ($P=a\times P_{app}+b$) and k: $a=0.768k^2+0.112k+1.386$.

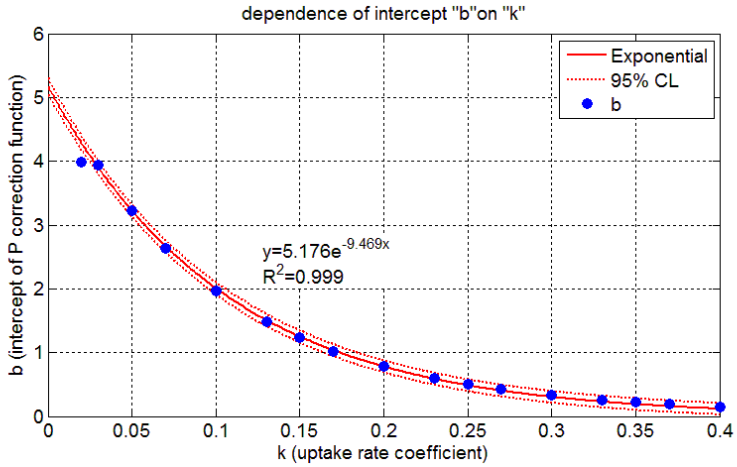

Fig. 2.10 The relationship between intercept "b" of the P correction function (P=a×P_{app}+b) and k: $b = 5.176e^{-9.469k}$.

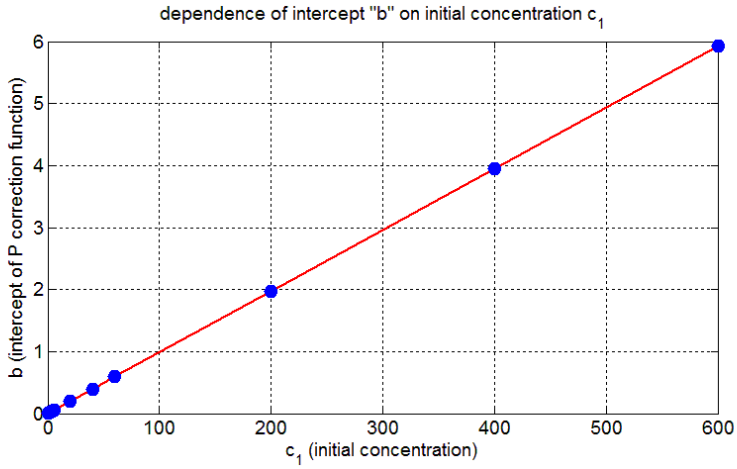

Fig. 2.11 The relationship between intercept "b" of the P correction function (P=a×P_{app}+b) and c_1: $b_{c_1} = \frac{c_1}{400}5.176$.

In conclusion, the relation for P and P_{app} is:

$$P = (0.768\mathrm{k}^2 + 0.112\mathrm{k} + 1.386)P_{app} + 0.013c_1e^{-9.469k} \quad (26)$$

For Speuld samples that are collected at 5-minute time interval rather than 10 minutes, the correction function is:

$$P_{SPU} = (0.037\mathrm{k}^2 + 0.177\mathrm{k} + 1.486)P_{app} + 0.036c_1e^{-4.570k} \quad (27)$$

As discussed above, the actual k and P can be retrieved from Eq. (24-27) if k_{app} and P_{app} are known. Ideally, k_{app} and P_{app} can represent the uptake rate coefficient k_{exp} and production rate P_{exp} from our experiments if the samplings and measurements are perfectly done. Though the samplings and measurements are always not perfect, here we assume k_{app}=k_{exp} and P_{app}=P_{exp}. The difference between k_{app} and k_{exp}, P_{app} and P_{exp} are not

discussed in this thesis. Fig. 2.4a-b shows two examples of the comparison between experiment results and model simulation results by retrieving k and P from k_{exp} and P_{exp}, with one in Cabauw (CBW-16) and one in Speuld (SPU-5). For these two examples, the experiment results of H_2 mixing ratio for the four flasks (green asterisk) seem to be quite similar to the ideal model simulation results (red circle) in the flasks after applying Eq. (24-27) to k_{exp} and P_{exp}. The difference between k_{app} and k_{exp}, P_{app} and P_{exp} is within 0.1%. These are just two examples that compare the experiment results (green asterisk) with ideal model simulation results (red circle) after applying Eq. (24-27) to retrieve actual k and P from k_{exp} and P_{exp}.

2.3 Laboratory determination of H_2 mixing ratio and D content of air samples

The mixing ratio and deuterium (D) content of hydrogen (H_2) are measured with a gas chromatography isotope-ratio mass spectrometer (GC/IRMS) at IMAU. For H_2 mixing ratio, the laboratory working standards are linked to the MPI2009 scale developed at the MPI-BGC (Jordan and Steinberg, 2011). Most of the samples collected from Cabauw were measured within two months after sampling, while samples from Speuld were kept in the dark storage room for around four months before measuring.

The main idea of the GC/IRMS system is to separate H_2 from the air matrix at extremely low temperature (about 36 K) and measure the HH and HD content with a mass spectrometer. The schematic processes of the measurement with GC/IRMS are shown in Fig. 2.12 (Batenburg, 2012). The measurement includes four main steps:

(1) The glass sample volume (~750ml) is evacuated and subsequently filled with ~700 mbar of sample air, which is then exposed to a cold head (~36K) of a closed-cycle helium compressor for 9 min. During this stage, all gases except H_2, helium (He) and neon (Ne) are condensed.

(2) The remainder in the cold head is then flushed with He carrier gas to a pre-concentration trap where H_2 is collected on a 25 cm in length, 1/8'' (3.2 mm) o.d. (outer diameter) stainless steel tube filled with fine grains (0.2~0.5 mm) of 5 Å molecular sieve, for 20 min. The pre-concentration trap is cooled down to the triple point of nitrogen (63 K) by pumping on the headspace above liquid N_2.

(3) After the collection of H_2, the pre-concentration trap is warmed up to release the absorbed H_2, which is then cryo-focused on a capillary (25 cm in length, 0.32 mm i.d. (inner diameter)) 5 Å molecular sieve column at 77 K for 4 min. After that, the 5 Å molecular sieve is warmed up to ambient temperature and the H_2 sample is flushed with He carrier gas onto the 5 Å molecular sieve GC column (~323 K,) where H_2 is chromatographically purified from potential remaining interferences.

(4) In the end, the purified H_2 is carried with He carrier gas via an open split system into the isotope-ratio mass spectrometer for D/H ratio determination.

More details about the GC/IRMS system and measurement steps can be found in Batenburg et al. (2011), Rhee et al. (2004) and Röckmann et al. (2010).

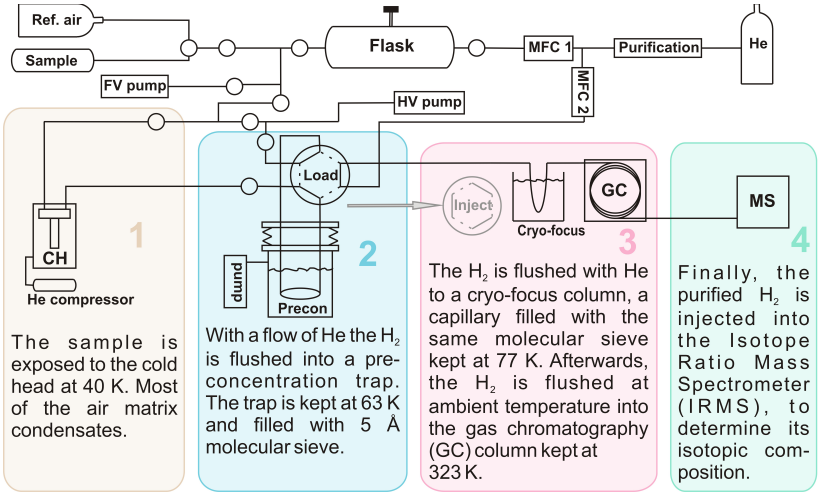

Fig. 2.12 Schematic processes of measuring H_2 mixing ratio and its D content with a GC/IRMS (taken from Batenburg, 2012), described by Batenburg et al. (2011), Rhee et al. (2004) and Röckmann et al. (2010).

Chapter 3
Data processing

3.1 Non-linearity of the GC/IRMS system

The δD of H_2 measured with GC/IRMS should not depend on the total amount of H_2 used for analysis, but in practice a dependency of the isotopic composition on the total peak area detected in the instrument (which is proportional to the mole fraction in an air sample of a certain volume) is observed. This is called a non-linear behavior, and it is a particularly severe limitation for soil uptake studies, since the mixing ratio in an air sample can decrease by more than an order of magnitude. For comparison, in ambient background air the variations are usually of the order of 20%.

This section discusses experiments carried out with the GC/IRMS to determine a suitable correction for the non-linear behavior. When samples of different size, but from the same air cylinder, are analyzed for isotopic composition, the δD value is relatively stable for air samples that produce a H_2 peak area larger than 1 V s (Fig. 3.1) in the instrument. However, for peak areas smaller than 1 V s, we observe an increase in the instrument noise (random error) and a systematic decrease or increase in the δD value (systematic error) (Fig. 3.1). It is expected that this effect also happen when measuring the flask samples with low mole fractions at normal sample pressure. Since about 30% of our forest samples lie in the 0.2~1.0 V s peak area region, it is necessary to find determine a suitable correction method to retrieve the δD values for these samples, i.e. a method or function is needed to correct for the systematic error, while keeping the noise as small as possible.

The large uncertainty for low-peak-area (LPA) measurements can be caused by: (1) influence of the background signal (instrument blank); (2) increase in the signal to noise ratio of the GC/IRMS at small amount of hydrogen; and (3) the integration method used to calculate HH and HD peak areas (discussed below).

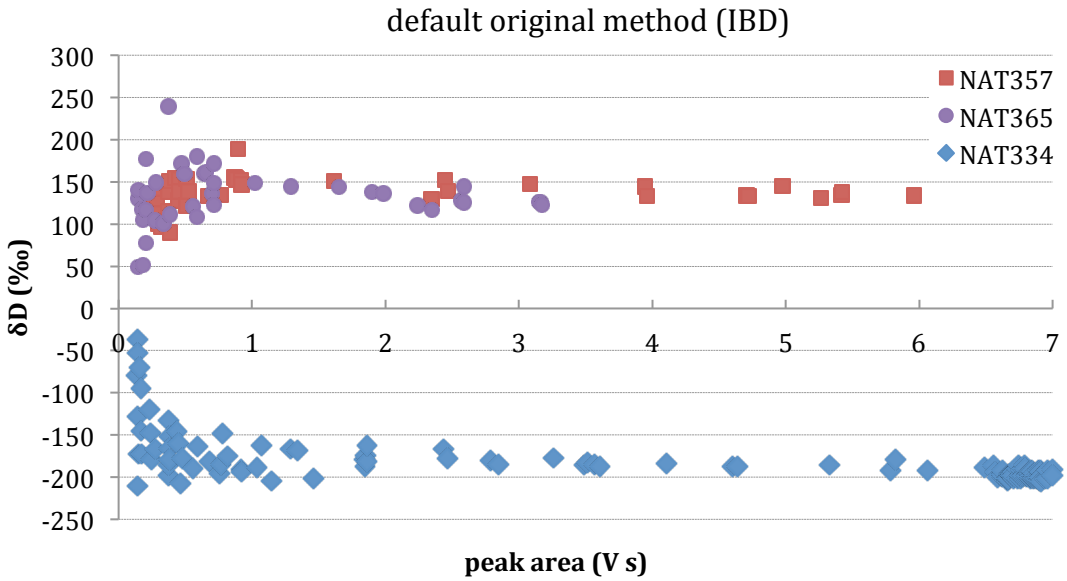

Fig. 3.1 The variation of δD with peak area for three reference gases by use of default original method "IBD". NAT334, NAT357 and NAT365 are three reference gases used in our laboratory with different H_2 mixing ratio and deuterium content.

The peak area of H_2 for a blank measurement (i.e. a measurement without injecting a samples) is 0.023±0.011 V s during the measurement period. For our air samples, the peak area of H_2 is larger than 0.2 V s. Thus, the influence of the blank can be significant for our LPA samples. For example, when the peak area of H_2 in our sample is 0.2 V s, the peak area of the blank is about 10% of that of the air sample. Both the blank (background signal of the system) and the signal to noise ratio of the GC/IRMS at small amounts of H_2 are limited by the instrument, so that we cannot get rid of these two effects unless we develop new technology. Therefore, the focus was on optimizing the data processing method, in particular the peak integration routine for the HH and HD peaks, for the low peak area samples from the soil uptake experiments. The goal was to find a peak integration method that minimizes random noise and is also associated with a reproducible systematic error as a function of peak area that can be used to derive a correction function. We used two different datasets to determine this correction function: (1) measuring reference gases at various peak area by injecting the same sample at various pressures in the sample volume (see Fig 3.1); (2) stepwise dilution of air samples with H_2-free "zero air" to low concentrations so that they cover a similar interval of peak areas as covered by the samples. Using these two datasets, different integration methods were used to calculate HH and HD peak areas.

3.1.1 Peak integration method

The raw signal of the IRMS system consists of two ion current peaks for HH and HD. For determination of δD, the areas for these two peaks (of near-Gaussian shape) are compared. The peak area is defined as the area above a baseline, which is the background signal from the mass spectrometer. The choice of this background value (baseline of the peak integration), as well as the choice of the peak integration boundaries (start and end point of the peak integration) influence the peak areas and thus the δD value of the injected air sample. This influence is generally larger for smaller peaks, because when the peak height is closer to the baseline, and little change in the baseline value would result in considerable change in peak area.

From the available dataset, it was apparent that the default instrument method "individual background detection" (IBD) shows large instrument noise. Furthermore, the different systematic trends for different reference gases at low peak area (< 1 V s) make correction almost impossible (Fig. 3.1). To reduce this uncertainty, different peak integration methods are used to calculate δD (Table. 3.1).

The IBD routine choses the lowest running five-point average among the data points before a peak starts during a pre-defined period (default 5 sec) before the peak start. The time-based background (TBD) is defined as the average of all data points within a selected time interval. More integration methods include Median Mean (test_e2_1), Low Pass (test_e4_1) and Calculation Mean (test_e5_1) that are not explained in detail here. Other parameters of the integration methods that we can change, such as time interval, start and end slope of the peak, spike filter, history, timeshift and detection mass, are not described in details here as well. Here we focus on the results generated by the different integration methods.

Fig. 3.2a-c shows the comparison of different methods for reference gas "NAT334" as an example. It can be seen that the original method IBD results in rather scattered δD values at low peak area. Some methods such as "test_e3_1" and "test_e4_1" also result in larger noise and are also not suitable. After this visual inspection, five methods that show performance are selected (Figure 3.2c), including three different methods with time-based background detection ("400-420s", "400-450s", "380-450s"), the Median-Mean background detection) "test_e2_1" and the Calculation Mean method "test_e5_1".

Table. 3.1 The parameters for different integration methods.

Name	Method	Time Interval (s)	End Slope	Spike Filter	History (s)	Timeshift (s)	Mass Detection
IBD	IBD	/	0.4	off	/	/	HH
TBD 400-420s	TBD	400-420	0.4	off	/	/	HH
TBD 400-450s	TBD	400-450	0.4	off	/	/	HH
TBD 380-450s	TBD	380-450	0.4	off	/	/	HH
test_e1_1	TBD	400-460	0.01	on	/	/	HH
test_e1_2	TBD	400-460	0.01	on	/	/	HD
test_e2_1	Median Mean	/	0.01	on	50	4	HH
test_e3_1	IBD	/	0.01	on	50	5	HH
test_e4_1	Low Pass	/	0.01	on	50	5	HH
test_e5_1	Calculation Mean	/	0.01	on	50	5	HH

Table. 3.2 The R^2 of the logarithmic fits (f(x)=a*ln(x)+b) for three reference gases, mean and standard deviation for corresponding residuals.

	R^2			Mean			STD		
	NAT334	NAT357	NAT365	NAT334	NAT357	NAT365	NAT334	NAT357	NAT365
400-450s	0.70	0.79	0.76	0.65	0.53	4.96	10.83	13.68	17.68
test_e5_1	0.73	0.77	0.71	1.65	0.94	3.78	8.16	14.02	18.22

The second step is the application of the correction function. The selection of the fit function will be described in detail in Section 3.1.2. Fig. 3.3 shows the residuals of δD after fitting with the logarithmic function f(x)=a*ln(x)+b for reference gases "NAT334" and "NAT357". It is difficult to tell by eye which integration method is preferable, so the residuals are analyzed to provide a quantitative measure of the goodness of the fit. If the data generated by a specific integration method can be fitted well with a certain function, then the residuals between the original data points and the corresponding values calculated from the logarithmic fit should show a normal distribution. The histograms for the residuals in Fig. 3.3 are shown in Fig. 3.4. When the confidence level is chosen to be 0.05 (2σ), all the residuals for different reference gases and integration methods lead to acceptance of the normal distribution hypothesis (h=0). However, when the confidence level 0.32 (σ) is chosen for "NAT334", the method "380-450s" and "test_e2_1" reject the normal distribution hypothesis (h=1), and the "p" values are calculated to be 0.174 and 0.237, respectively. Considering the "p-value", method "test_e5_1" is the best for "NAT334" and "400-450s" is the best for "NAT357". Thus, methods "400-450s" and "test_e5_1" are chosen for further comparison.

Fig. 3.5 shows the variation of δD with peak area for different air samples after scaling with mean δD values, by use of integration method (a-b) "400-450s" and (c-d) "test_e5_1" respectively. The scaling is done by subtracting mean δD values for peak areas > 3 V s (NAT334 and NAT357), > 2 V s (NAT365) and > 1 V s (all other air samples). Dilution flasks are "dilution S31-S36". The "NAT334" seems to follow similar trends (logarithmic) for both integration methods, when data is chosen to be between 0.2-1.0 V s. Fig. 3.6 shows the δD difference between methods "400-450s" and "test_e5_1" for three reference gases shown in Fig. 3.5. The difference is calculated as $\delta D_{test\_e5\_1} - \delta D_{400\text{-}450s}$. In general, δD calculated from integration method "test_e5_1" is larger than that of "400-450s". Though this will make small difference in the logarithmic function of the trend, it is not the criterion for choosing the integration method since δD will be corrected by the correction function in the end. The most important issue is how good the correction function is.

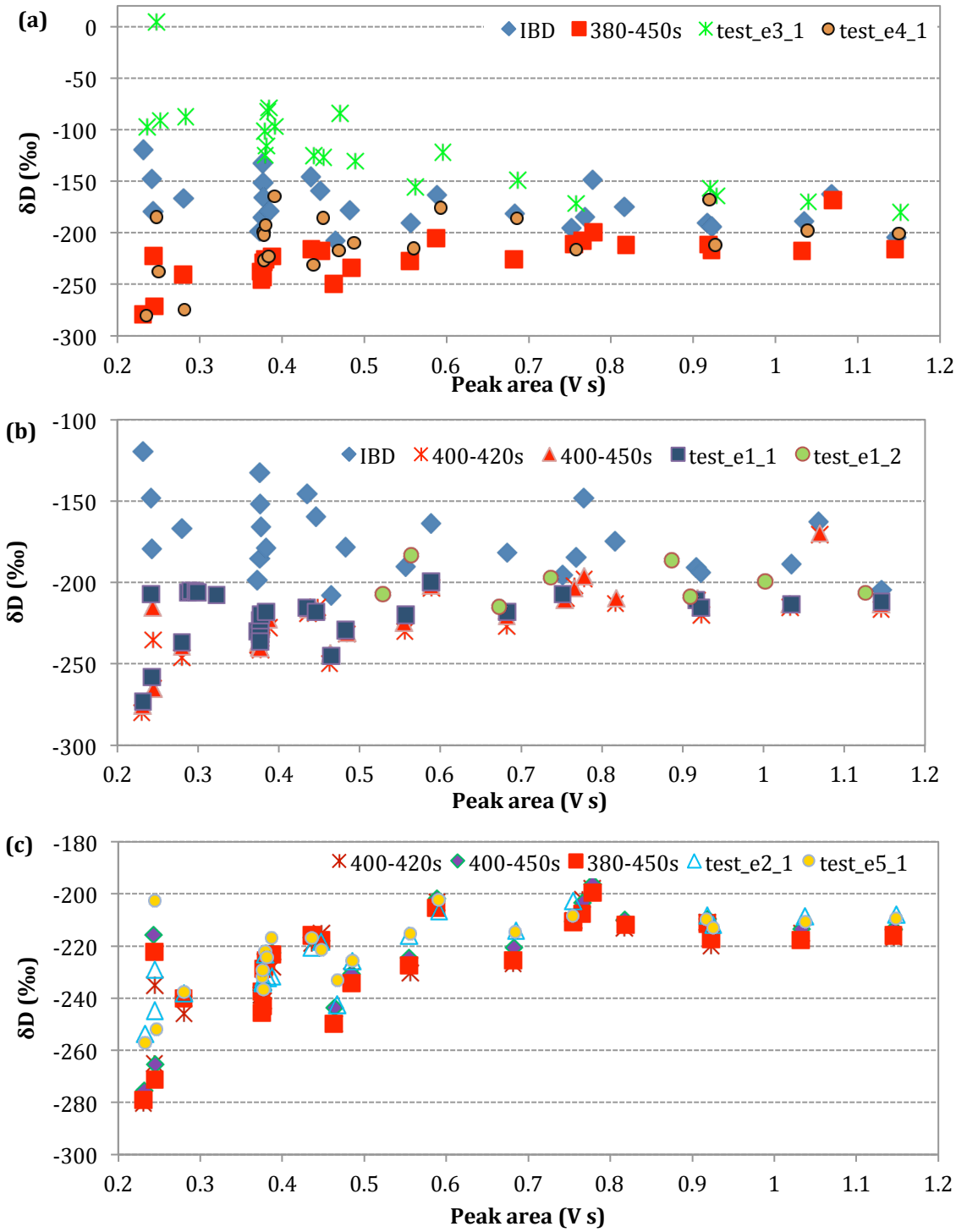

Fig. 3.2a-c The comparison of results obtained with different peak integration methods for Reference Gas "NAT334" at low peak area.

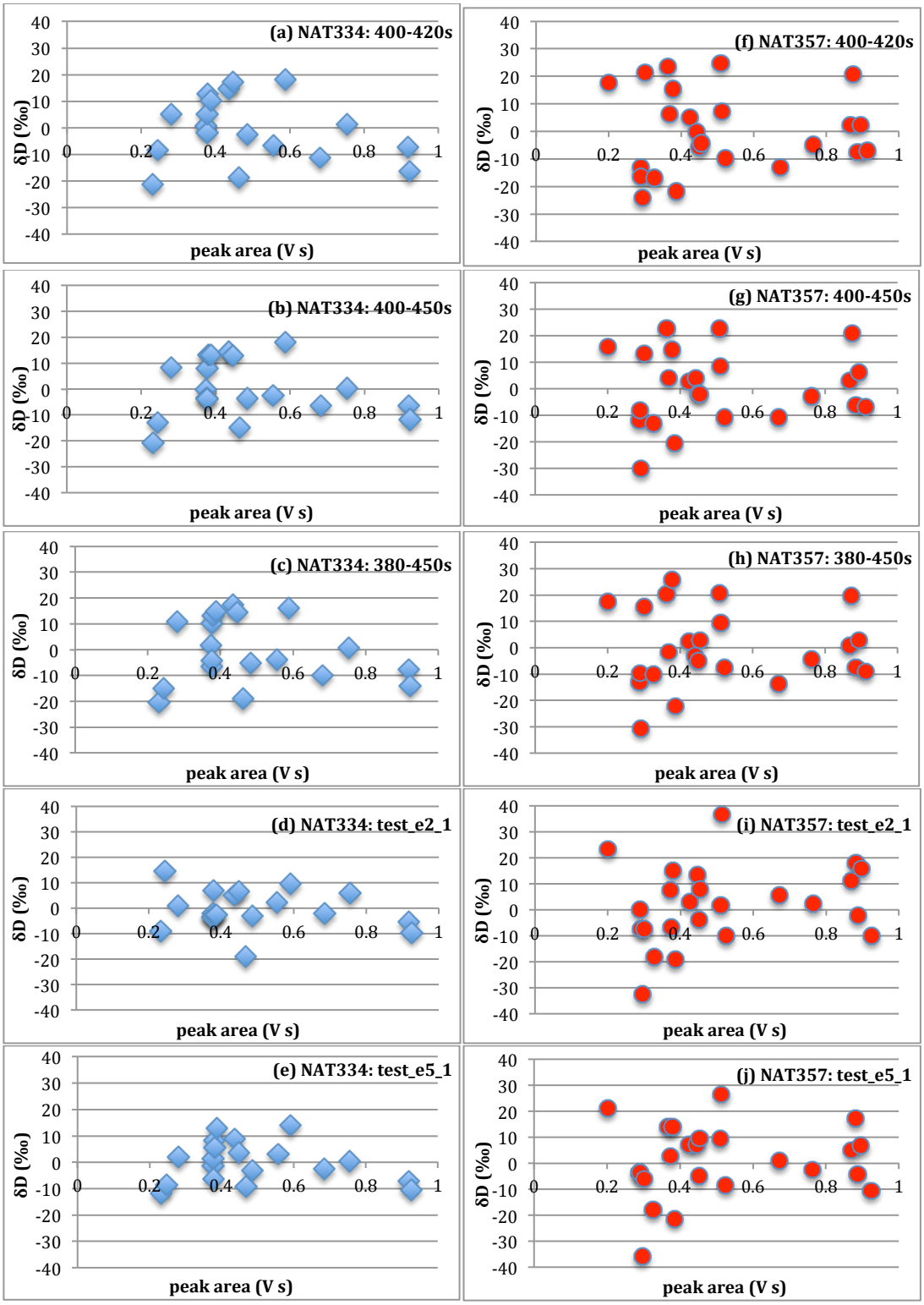

Fig. 3.3a-j The residuals between data and logarithmic fit for reference gases "NAT334" (a-e) and "NAT357" (f-j) at low peak area after fitting with logarithmic function (f(x)=a*ln(x)+b).

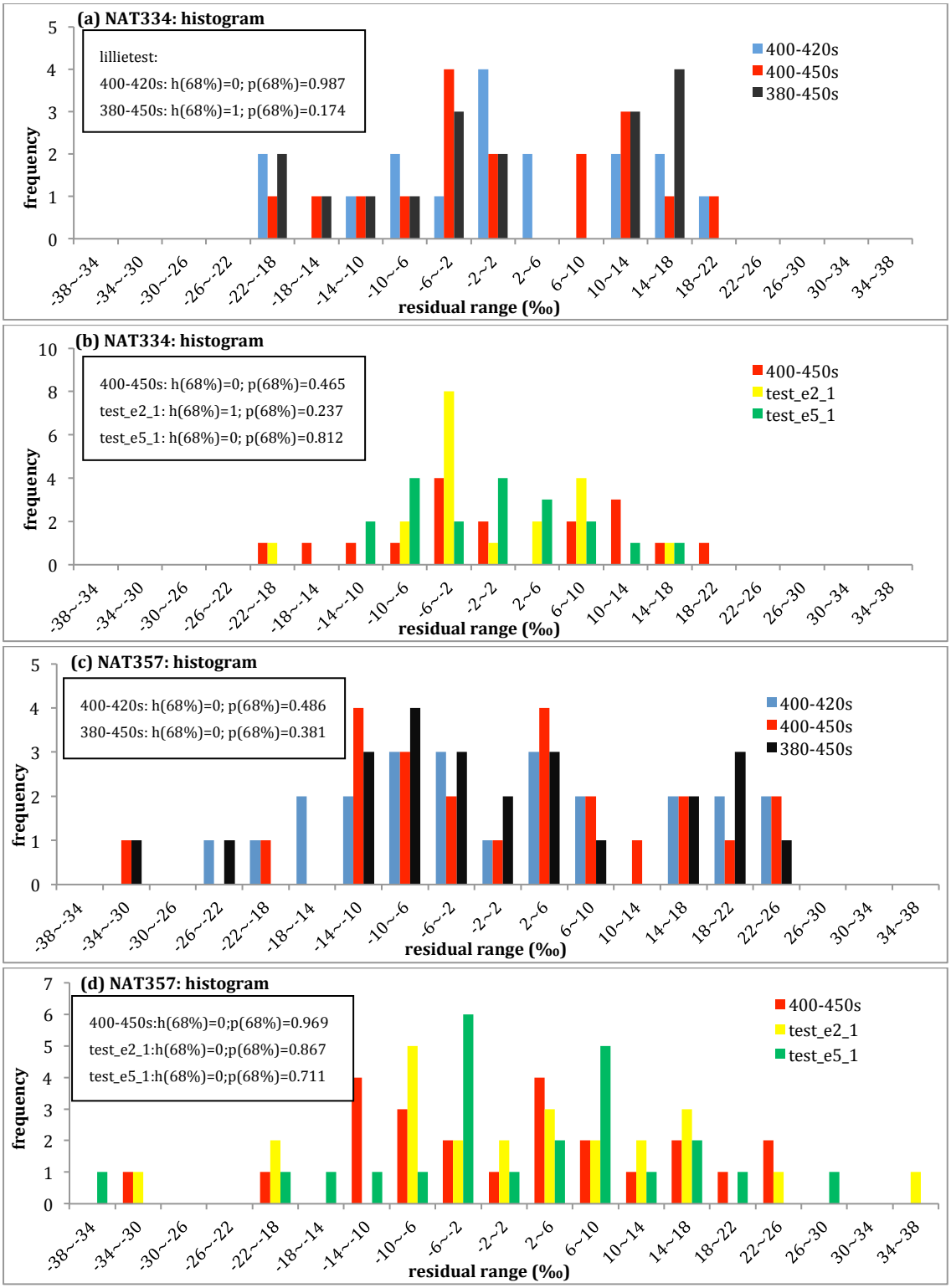

Fig. 3.4a-d The histogram (frequency) for the residuals for reference gases "NAT334" (a-e) and "NAT357" (f-j) shown in Fig. 3.3. Normal distribution tests are done on the residuals. "h=1" refers to rejecting the normal distribution hypothesis where "h=0" refers to accepting the normal distribution hypothesis. The "p-value" (from 0 to 1) is also calculated, where small values of p cast doubt on the validity of the normal distribution hypothesis. Lillietest is a test decision for the null hypothesis that the data follows normal distribution. The result h is 1 if the test rejects the null hypothesis at the 5% significance level, and 0 otherwise.

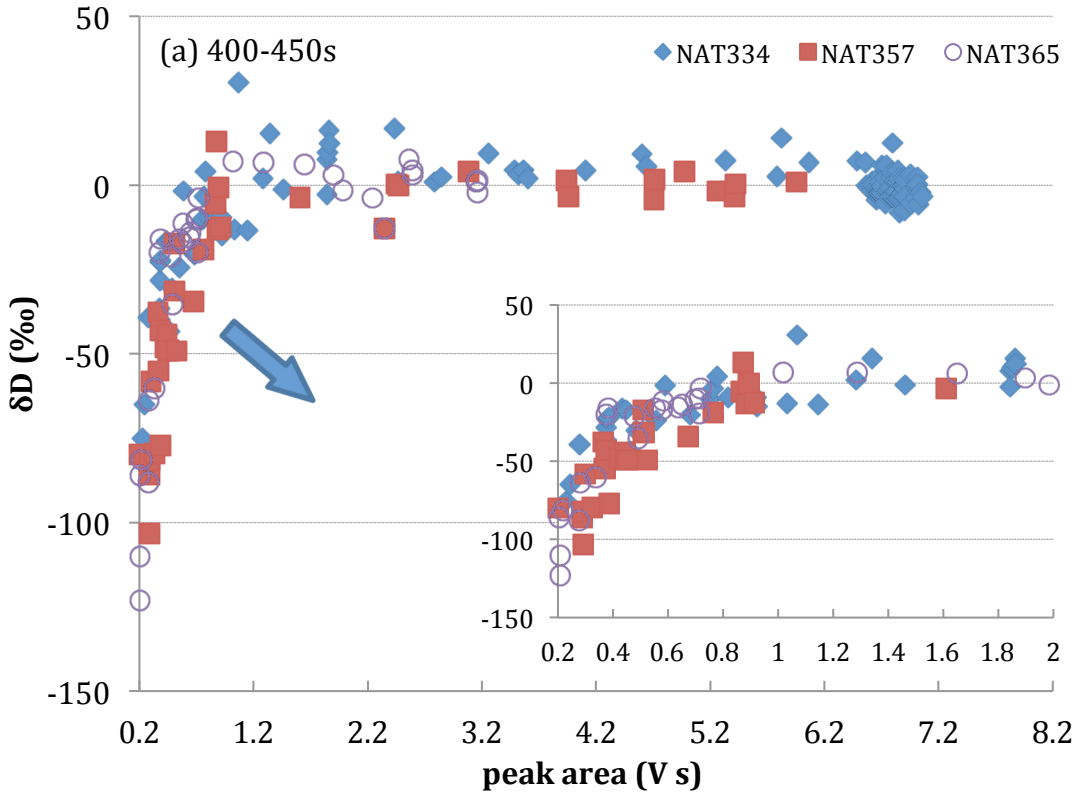
(a) 400-450s
NAT334
NAT357
NAT365
δD (‰)
peak area (V s)

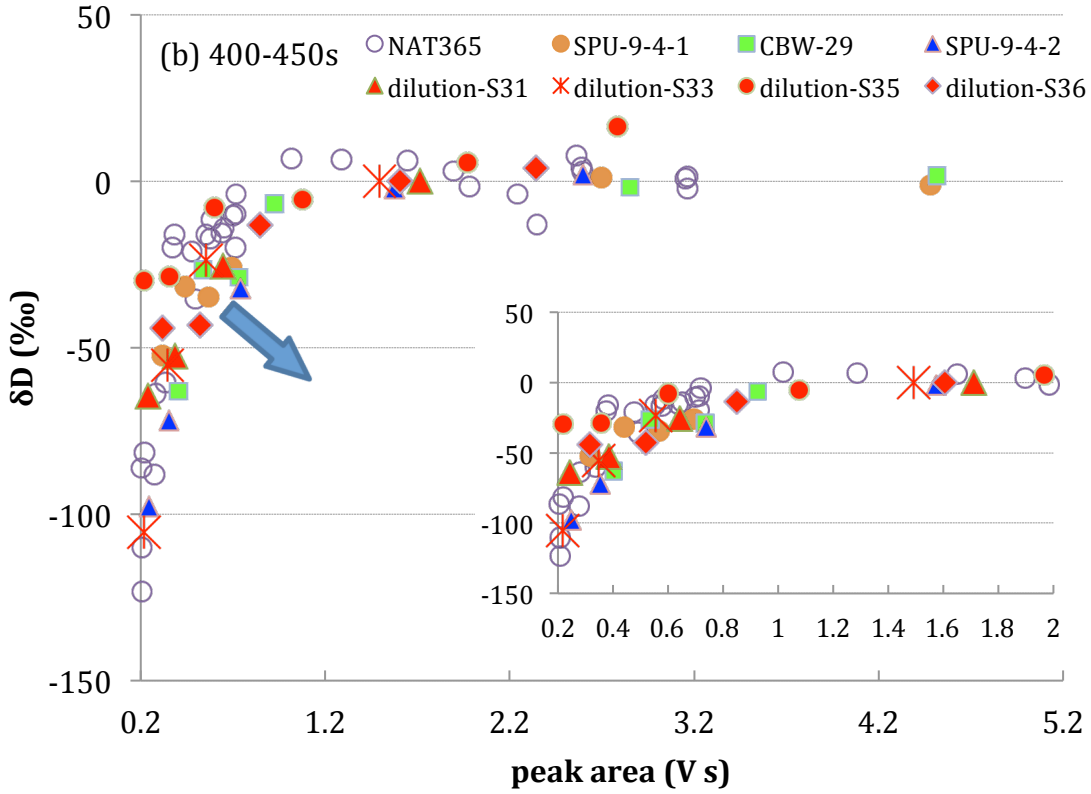
(b) 400-450s
NAT365
SPU-9-4-1
CBW-29
SPU-9-4-2
dilution-S31
dilution-S33
dilution-S35
dilution-S36
δD (‰)
peak area (V s)

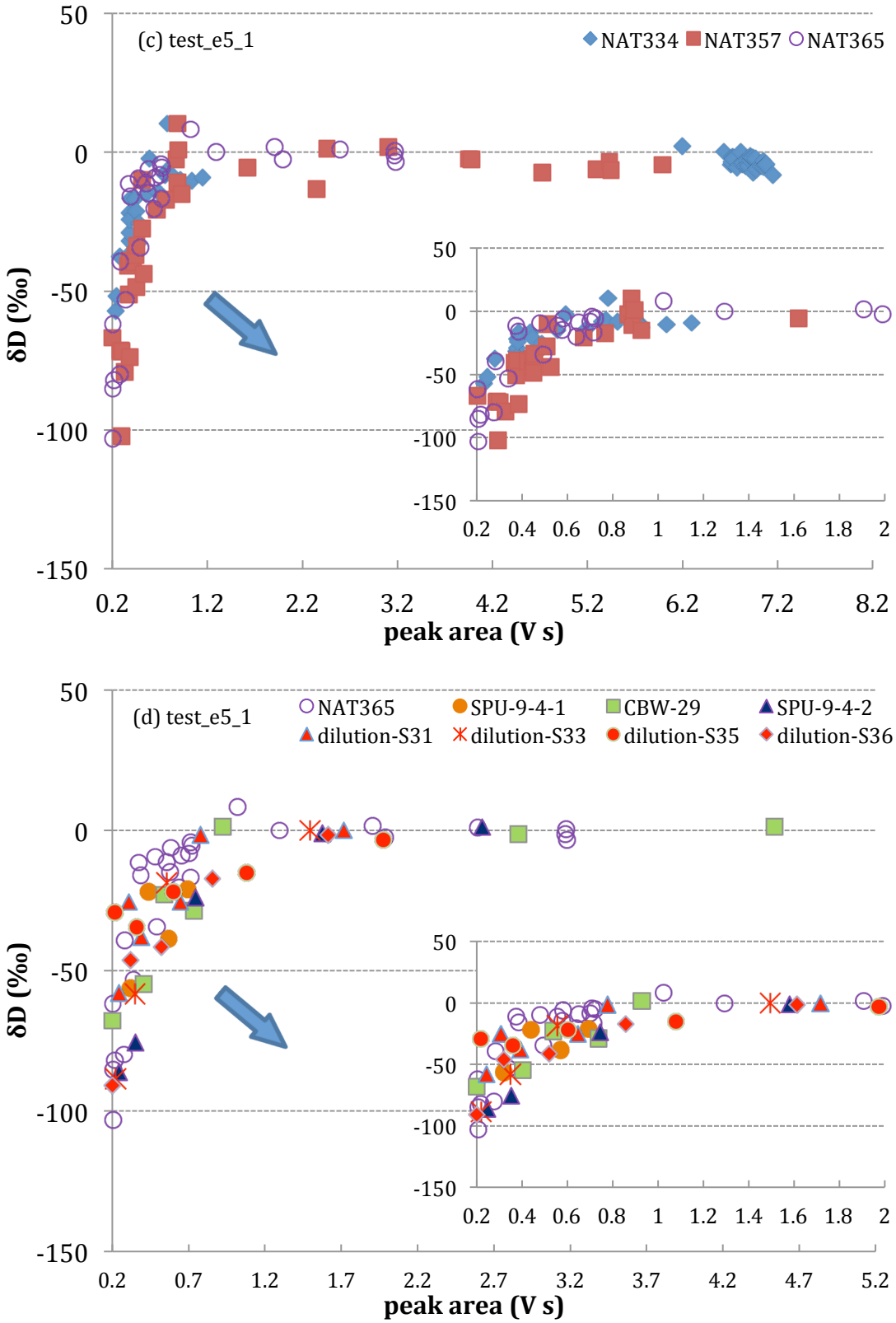

Fig. 3.5a-d The variation of δD with peak area for different air samples and two different integration methods "400-450s" and "test_e5_1" after scaling with mean δD values. The scaling is done by subtracting mean δD values for peak area > 3 V s (NAT334 and NAT357), > 2 V s (NAT365) and > 1 V s (all other air samples).

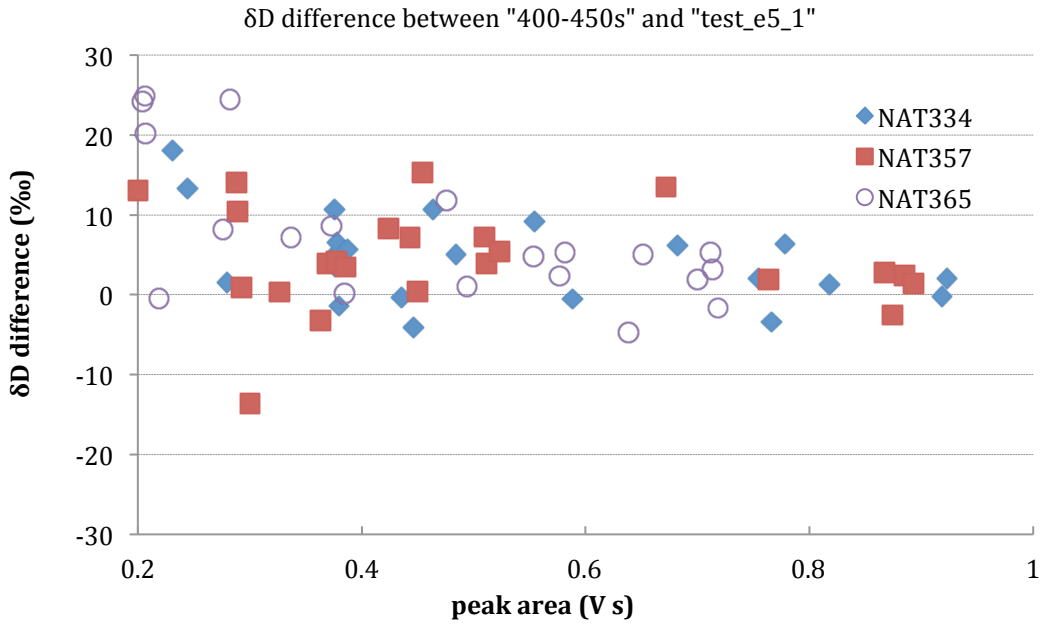

Fig. 3.6 The δD difference between the peak integration methods "400-450s" and "test_e5_1 for three reference gases shown in Fig. 3.5. The difference is calculated as $\delta D_{test\_e5\_1}$ - $\delta D_{400\text{-}450s}$.

The R^2 values of the logarithmic fits for three reference gases by use of integration methods “400-450s” and “test_e5_1” and mean and standard deviation for corresponding residuals are listed in Table 3.2. The large mean values for “NAT365” could be due to the reason that we do not have data between 0.8-1.0 V s for this reference gases, and the logarithmic plot was forced to 0‰ at 1V s. Overall both methods produce rather similar results, and method “400-450s” was chosen because it produces larger R^2 values for “NAT357” and “NAT365”, small mean for “NAT334” and “NAT357”, smaller standard deviation for “NAT357” and “NAT365”. In conclusion, the integration method “400-450s” is chosen.

3.1.2 Correction function for δD nonlinearity

3.1.2.1 Fit function

Fig. 3.7a-b shows the variation of δD with peak area smaller than 1 V s for two reference gases, by use of time-based background (TBD) 400-450s integration method. The logarithmic function is applied to the data and 67% prediction bounds are calculated. As can be seen from the two plots, the logarithmic function (f(x)=a*ln(x)+b) fits quite well the data with peak area of H_2 smaller than 1 V s. In addition, the error bars (σ) for the logarithmic plots in Fig. 3.7a-b are shown in Fig. 3.8a-b. It can be

seen that 67% of the observational data lie in the range of around ±15‰ of the logarithmic fits, when the peak area is between 0.2 V s to 1 V s.

In addition to fitting the data points in Fig. 3.7a-b with a logarithmic function, different functions are examined and the corresponding fit parameters are listed in Table 3.3. The R^2 and Root Mean Squared Error (RMSE) are considered to evaluate the goodness of the fit. It can be seen that the "linear" function does not fit well for Reference Gas "NAT334", while the "quadratic", "power" and "rational" functions show smaller RMSE, and larger R^2 values which indicate better fits. However, for different air samples these fit functions show very different and irregular coefficients, which enhance the difficulty to retrieve the "real" δD value from the experimental results ("x" and "f(x)" values in the fit functions). Compared with other fit functions, the logarithmic function is selected, because (1) the RMSE values is comparably small, especially for Reference Gas "NAT357"; (2) the coefficient b returns the δD value of the air sample, which indicates that the "real" δD value can be retrieved if a relation between the coefficients a and b is found.

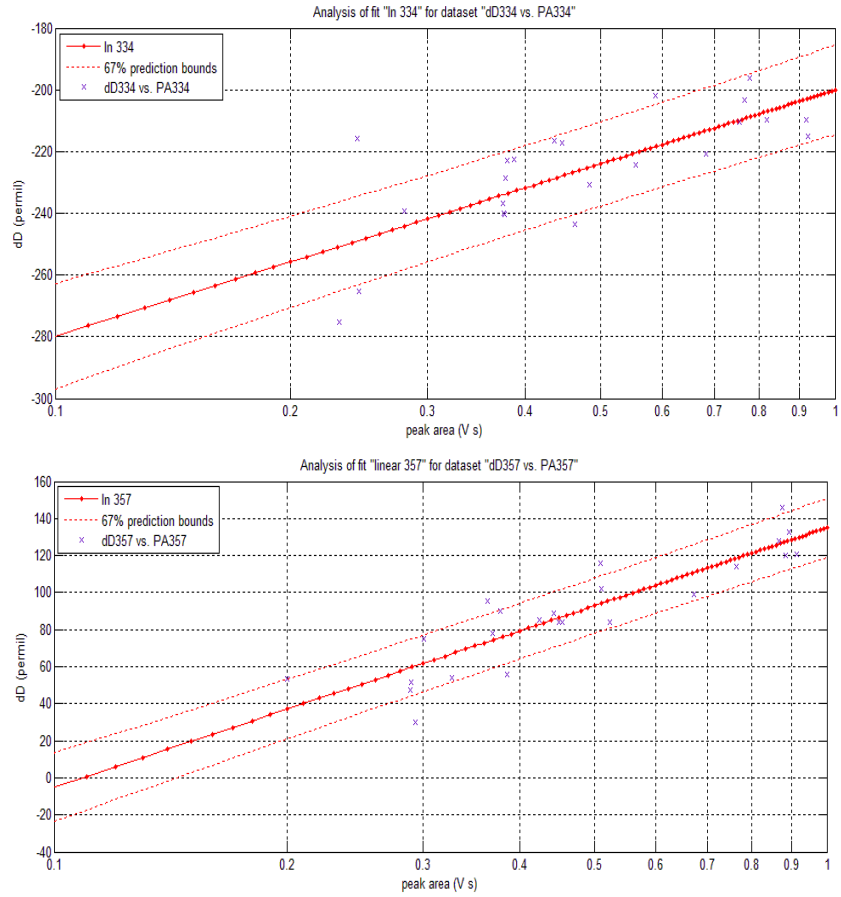

Fig. 3.7a-b The variation of δD with peak area (<1 V s) for two reference gases, using the time-based background 400-450s integration method. The low peak area of the reference gases is achieved by reducing the amount of reference gases measured, i.e. measured at low pressure. The x-axis is in logarithmic scale.

Table. 3.3 The parameters of different fit functions for the data points in Fig. 3.7a-b. The R^2 and RMSE refer to the Adjusted R^2, and root mean squared error, respectively. The 95% confidence level is calculated for parameters a, b and c. The Adjusted R^2 measures how successful the fit is in explaining the variation of the data, considering the residual degree of freedom.

NAT334	R^2	RMSE	function	a	b	c
linear	0.47	14.02	f(x) = a*x + b	62.2±28.4	-257.6±15.9	
quadratic	0.53	13.17	f(x) = a*x^2 +b*x + c	-135.7±145.0	217.4±168.2	-295.4±43.1
power	0.53	13.22	f(x) = a*x^b+c	-19.4±77.8	-0.86±1.95	-186±90
rational	0.53	13.22	f(x) = (a*x + b) / (x + c)	-189.0±41.7	-22.0±123.3	0.027±0.460
ln(x)	0.52	13.39	f(x) = a*ln(x)+b	34.6±13.8	-200.1±11.8	

NAT337	R^2	RMSE	function	a	b	c
linear	0.74	15.29	f(x) = a*x +b	113.7±28.8	30.51±16.2	
quadratic	0.75	15.01	f(x) =a*x^2 + b*x + c	-122.1±166.1	258.2±198.7	-5.5±51.2
power	0.74	15.32	f(x) = a*x^b+c	529.1±3474.9	0.13±1.18	-392.8±4545.2
rational	0.75	15.13	f(x) = (a*x + b) / (x + c)	224.7±169.9	-15.2±39.2	0.55±1.36
ln(x)	0.76	14.72	f(x) = a*ln(x)+b	60.8±14.6	134.9±12.6	

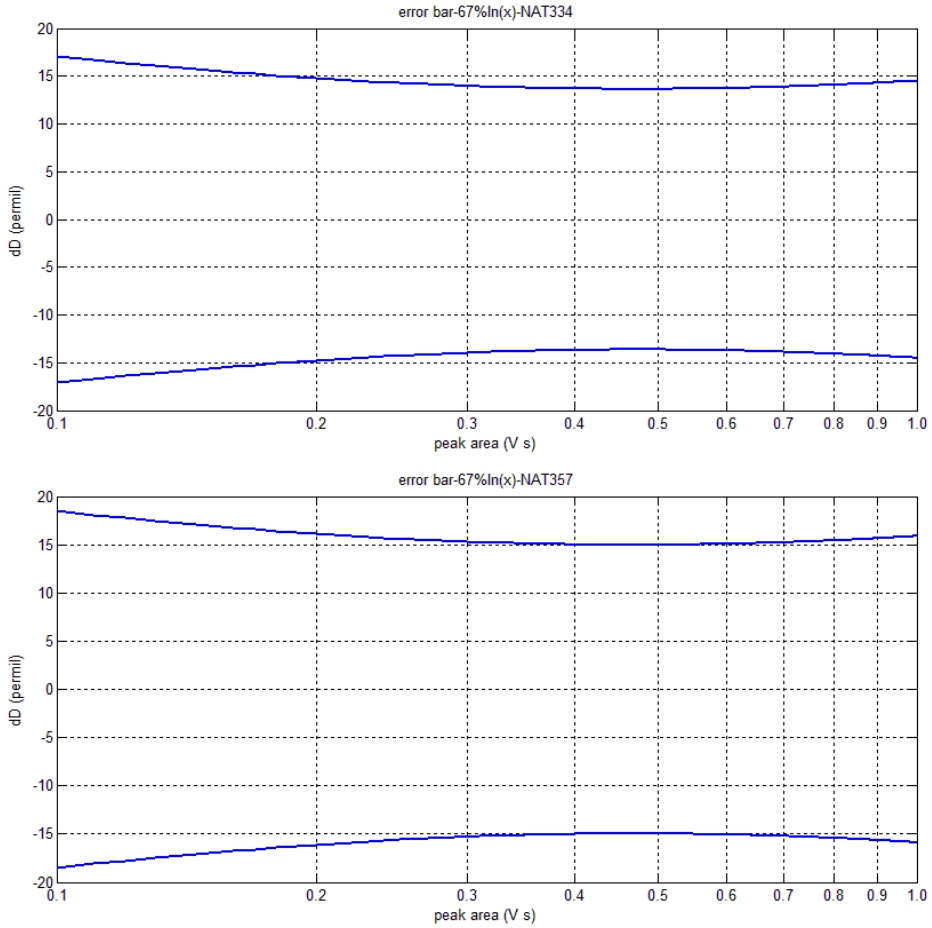

Fig. 3.8a-b The error bar (67% prediction bounds, i.e. 1 σ) for the logarithmic fits in Fig.3.7a-b.

3.1.2.2 Correction function for all experiments with δD influence

This section discusses the possibility to retrieve the true δD from the measured δD at low peak area, by considering that the correction function for δD at low peak area is different for air samples with different δD values. Fig. 3.9 shows the comparison of the logarithmic fits (f(x)=a*ln(x)+b) for three scaled reference gases with 67% confidence level. The R^2 for the fit functions are 0.53, 0.75 and 0.74 for reference gas "NAT334", "NAT357" and "NAT365" respectively. It shows that the optimum fit can be different for different reference gases with large difference in δD, e.g. "NAT334" (δD=-200.2±4.8 ‰) and "NAT357" (δD=133.3±3.0 ‰). The fits are close to each other for reference gases with similar δD ("NAT357" and "NAT365").

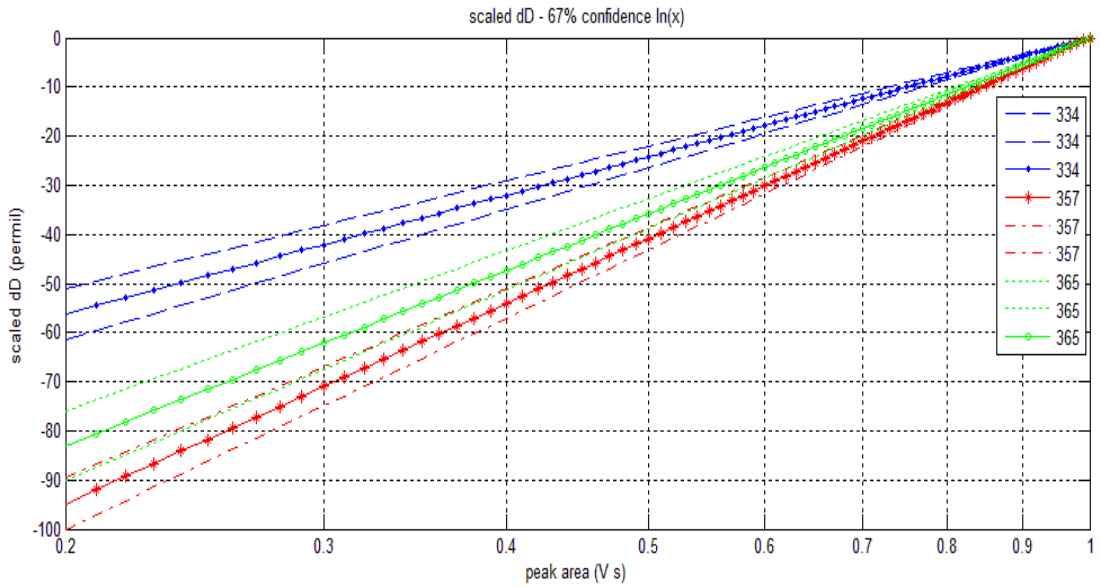

Fig. 3.9 The comparison of the logarithmic fits (f(x)=a*ln(x)+b) for three scaled reference gases with 67% confidence level. The scaling is done by subtracting mean δD values for peak area larger than 3 V s, which are -200.2±4.8, 133.3±3.0 and 119.2±5.6 ‰ for reference gas "NAT334", "NAT357" and "NAT365" respectively. The coefficient b is fixed to zero for all three fits. The R^2 for the fit functions are 0.53, 0.75 and 0.74 for reference gas "NAT334", "NAT357" and "NAT365" respectively.

In order to determine a possible relationship between the coefficient "a" of the logarithmic functions and δD for the corresponding reference gases, we carried out more experiments to get different coefficient a for different air samples, including (1) three normal flasks (different δD) at low pressure; (2) four dilution flasks (different δD) at normal pressure. The relationship between the coefficient "a" and δD for all experiments are shown in Fig. 3.10. When all the experiments are taken into account, i.e. the influence of the pressure is negligible, the coefficient a and δD can be fitted with the function:

$$a = (0.07\pm0.02)\ \delta D + (50.42\pm2.64) \qquad (28)$$

Consequently, the general fit function for the δD and peak area is:

$$f(x)=[(0.07\pm0.02)\ \delta D + (50.42\pm2.64)]\ \ln(x) + \delta D \qquad (29)$$

where f(x) and x are the δD value and peak area of hydrogen given by the GC/IRMS. In this way, we calculate the δD value for low-peak-area samples. For convenience, Eq. (29) is transformed into:

$$\delta D_{true} = \frac{\delta D_{measured} - 50.42\ ln(x_{PA})}{1+0.07\ ln\ (x_{PA})} \qquad (30)$$

where δD_{true} is the δD after correction, $\delta D_{measured}$ and x_{PA} are δD and corresponding peak area of HH given by the GC/IRMS. The error (Fig. 3.11) for δD_{true} depends on $\delta D_{measured}$ and x_{PA}. This error consists of two parts: (1) measurement error (standard deviation of all data at each peak area); (2) error of the logarithmic fit. The error for δD is around 5‰ when the peak area is 1 V s (similar to 120 ppb measured at 700 mbar with our GC/IRMS). This error increases to 35‰ when the peak area is 0.2 V s (similar to an air sample with 20 ppb of H_2 measured at 700 mbar with our GC/IRMS). The error is relatively small compared to other published studies.

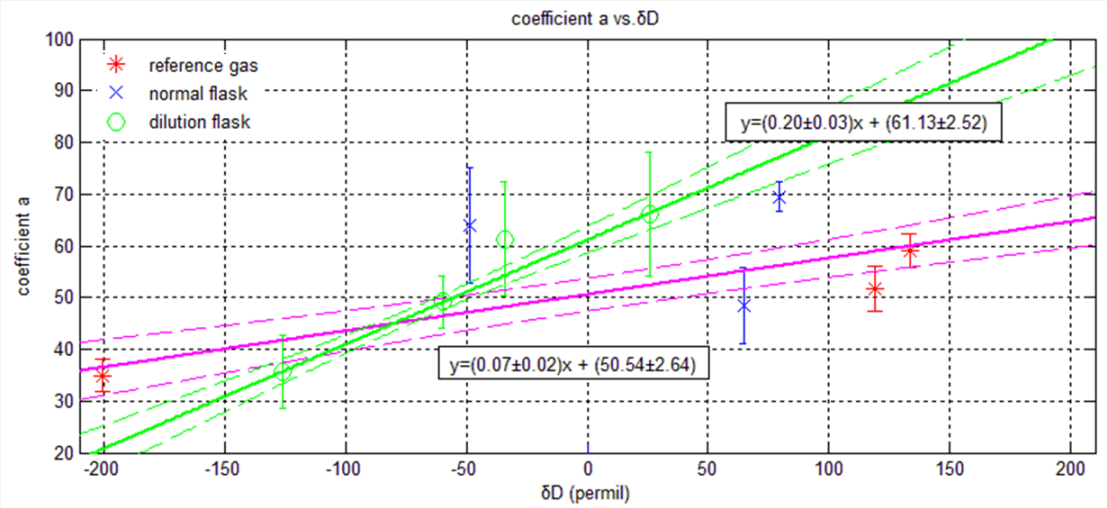

Fig. 3.10 The relation between coefficient a of the logarithmic fits (δD versus peak area) and δD for the corresponding reference gases. The 67% confidence level is plotted. The function of the linear plot for all the data (purple) is: y = (0.07±0.02) x + (50.42±2.64), while for dilution flasks (green) is: y = (0.20±0.03) x + (61.13±2.52).

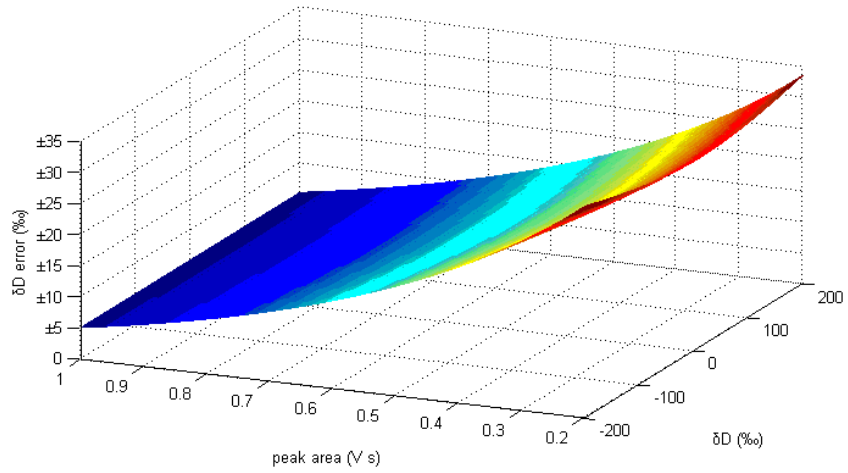

Fig. 3.11 The error for δD at different peak area when considering all experiments (three reference gases, three normal flasks and four dilution flasks in Fig. 3.10).

3.1.2.3 Correction function for dilution experiments with δD influence

When the pressure effect is taken into account, i.e. considering the dilution experiments at normal pressure only (green circle in Fig. 3.10), the fit function for the δD and peak area is:

$$f(x)=[\ (0.20\pm0.03)\ x + (61.13\pm2.52)]\ \ln(x) + \delta D \qquad (31)$$

i.e.

$$\delta D_{true} = \frac{\delta D_{measured} - 61.13\ ln(x_{PA})}{1+0.2\ ln\ (x_{PA})} \qquad (32)$$

The error for the δD at different peak area is shown in Fig. 3.12.

For the δD correction of our Speuld samples that generally have δD values higher than 100‰, Function (32) can give >10‰ higher δD than Function (30) when peak areas x_{PA}=0.5 (V s) are considered. However, both functions have shortcoming and it is difficult to decide which one to use. When all experiments are considered (Function (30)), there is no obvious trend for the data with δD values higher than -50‰. However, when the dilution flasks are considered only (Function (32)), we do not have dilution flask experiments at high δD values (>100‰).

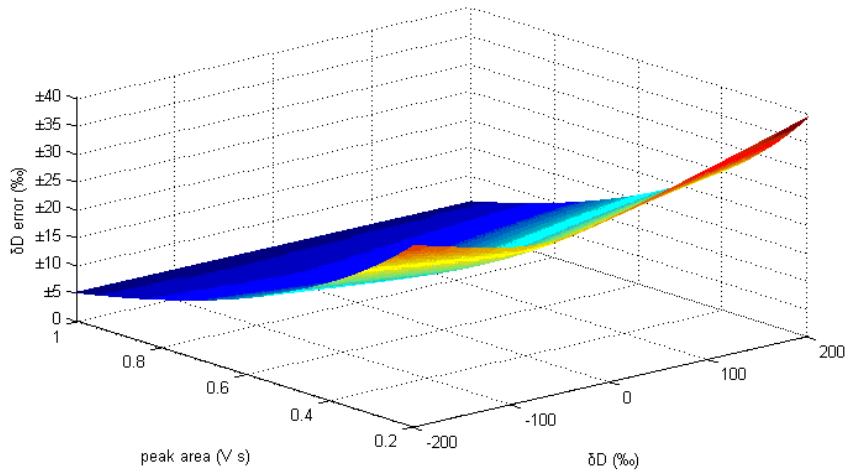

Fig. 3.12 The error bar for δD at different peak area when considering the dilution flasks (green circles in Fig. 3.10) measured at normal pressure (~700 mbar) only.

3.1.2.4 Correction function for high-δD experiments with δD influence

Since all our Speuld samples have δD values higher than 50‰, it is reasonable to consider the coefficient "a" in Fig. 3.10 in this specific region only. Consequently, the mean coefficient "a" for δD values higher than 50 ‰ is calculated to be 61.52±11.80. By using this method, the calibration for the δD value and its error bar will depend on the peak area only. The error bar is shown in Fig. 3.13.

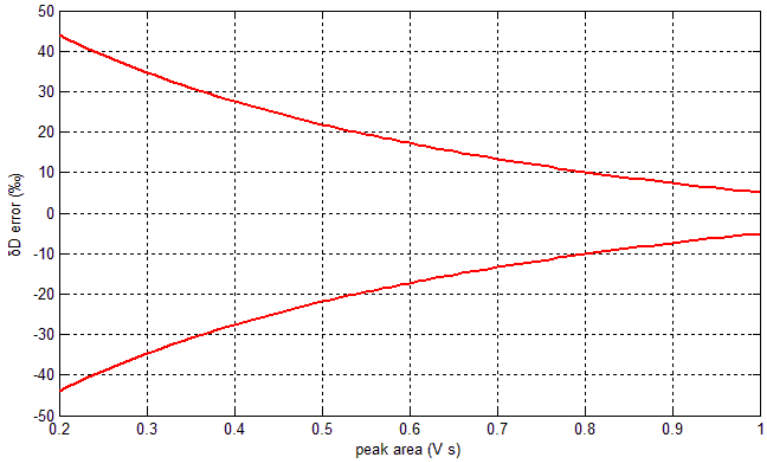

Fig. 3.13 The error bar for δD at different peak area when considering the experiments with δD values higher than 50 ‰ only. The coefficient "a" for the logarithmic function is 61.52±11.80.

3.1.2.5 Correction function for all experiments with one function

As shown in Fig. 3.5a-b, it seems appropriate to apply one fit to all the experiments including reference gases, normal flasks and dilution flasks. The comparison of different fit functions is shown in Table 3.4. I prefer the logarithmic function (y=a*ln(x)) because it is simple and it can be further potentially used to find out the dependence of "coefficient a" on δD of the sample (Fig. 3.10). Thus, I use this function to fit all the data and the result is shown in Fig. 14 here. The fit coefficient "a" is 49.1. If we fit all the data with only one function (Fig. 3.14), then the error bar is shown in Fig. 3.15. The correction function for the δD is:

$$\delta D_{true} = \delta D_{measured} - 49.1*\ln(x_{PA}) \qquad (33)$$

This is the correction function used in this thesis.

Table. 3.4 The parameters of different fit functions for all the data, by use of integration method "400-450s". The R^2 and RMSE refer to the Adjusted R^2, and root mean squared error, respectively. The 68% confidence level is calculated for parameters a, b and c. The Adjusted R^2 measures how successful the fit is in explaining the variation of the data, considering the residual degree of freedom.

400-450s	R^2	RMSE	function	a	b	c, d
linear	0.57	17.74	f(x) = a*x +b	95.4±8.8	-81.6±4.7	
quadratic	0.67	15.51	f(x) =a*x^2 + b*x + c	-178.2±37.9	293.5±42.2	-128.4±10.4
cubic	0.67	15.46	f(x) =a*x^3 + b*x^2+ c*x+d	240.9±191.5	-581.8±318.6	497.5±162.7, -158.7±25.2
4th degree	0.67	15.52				
5th degree	0.67	15.51				
exponential	0.67	15.44	f(x) = a*exp(b*x) + c*exp(d*x)			
power	0.68	15.33	f(x) = a*x^b+c	-46.1±38.5	-0.63±0.33	44.26±42.2
rational	0.68	15.31	f(x) = (a*x + b) / (x + c)	27.5±14.0	-29.8±10.2	0.10±0.10
ln(x)	0.66	15.67	f(x) = a*ln(x)+b	49.1±3.7	4.5±3.4	
ln(x)	0.66	15.79	f(x) = a*ln(x)	44.5±1.8		

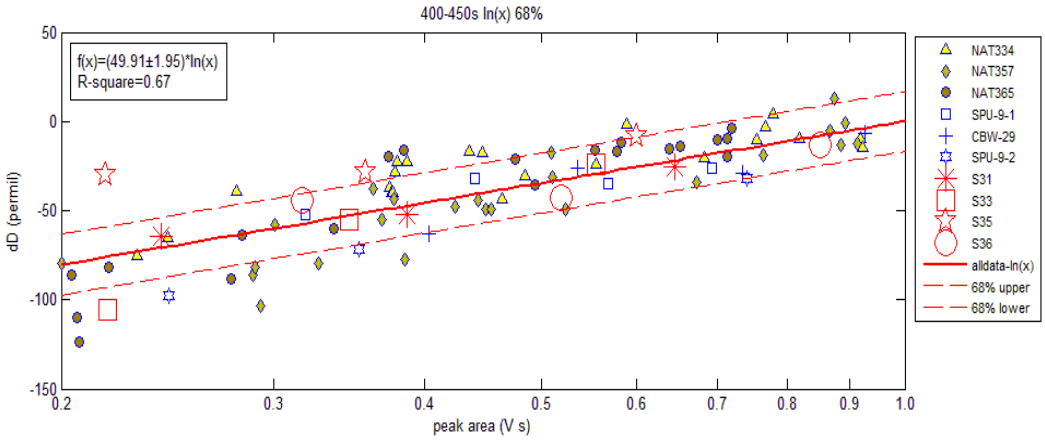

Fig. 3.14 The logarithmic fit to all the data points. The dilution flasks are S31, S33, S35 and S36. The normal flasks measured at low pressure are "SPU-9-1", "CBW-29" and "SPU-9-2".

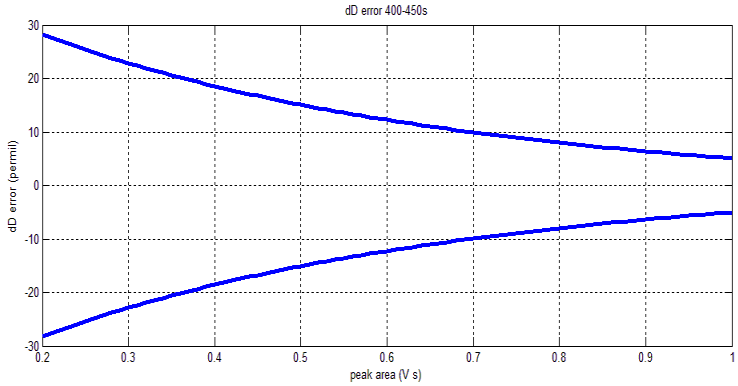

Fig. 3.15 The error bar for δD when applying for logarithmic fit to all the data points at peak area smaller than 1 V s (Fig. 3.14).

3.2 The Keeling plot and the Rayleigh fractionation equation

Assume a small air parcel (single source) with H_2 mixing ratio a (total air molecules x_1; H_2 molecules y_1) and isotopic signature δ_a (HD molecules z_1), being mixed with a big background air parcel with H_2 mixing ratio "b" (total air molecules x_2 ($x_1 << x_2$); H_2 molecules y_2) and isotope signature δ_b (HD molecules z_2). Then the mixed air parcel will obtain the H_2 mixing ratio (a+b) (total air molecules x_2 and H_2 molecules y_1+y_2) and isotopic signature δ_{a+b} (HD molecules z_1+z_2). From the mass balance equation and the approximation of [HD]/[HH] = 2[D]/[H], we have:

$$\frac{y_1+y_2}{x_2}\left[\frac{(z_1+z_2)/(y_1+y_2)}{\left(\frac{D}{H}\right)_{ref}}-1\right]=\frac{y_1}{x_2}\left[\frac{(z_1)/(y_1)}{\left(\frac{D}{H}\right)_{ref}}-1\right]+\frac{y_2}{x_2}\left[\frac{(z_2)/(y_2)}{\left(\frac{D}{H}\right)_{ref}}-1\right] \quad (34)$$

i.e.

$$(a+b)\,\delta_{a+b} = a\,\delta_a + b\,\delta_b \quad (35)$$

This is the equation that expresses the linear correlation between δ_{a+b} and 1/(a+b). The δ-value measured is proportional to the reciprocal of the mixing ratio. Theoretically, if we plot δ_{a+b} against 1/(a+b) and fit the data with a linear function, then the intercept the fit represents the isotopic signature of the source. This curve is the so-called Keeling plot, which was first used by Keeling (1958, 1961) to identify the sources that caused the increase of atmospheric CO_2 mixing ratio in a forest. The Keeling plot is valid only when there is a single source of H_2 and no sink exists.

In contrast, if there is a single sink of H_2 and no source exists, then we can derive the Rayleigh fractionation equation. Assuming the removal rate coefficient for HH and HD are k and k' respectively, then the time evolution of HH and HD can be expressed as Eq. (36) and (37).

$$\frac{dc}{dt} = kc \quad (36)$$

$$\frac{dc'}{dt} = kc' \quad (37)$$

The solutions are of the form:

$$c = c_i\, e^{-kt} \quad (38)$$

$$c' = c_i' e^{-k't} \qquad (39)$$

where c and c_i are the mixing ratio of HH at time t and initially, while c' and c_i' are those for HD. The transformation of Eq. (38) and (39) yields:

$$\ln\frac{c}{c_i} = -\mathrm{kt} \qquad (40)$$

$$\ln\frac{c'}{c_i'} = -\mathrm{k't} \qquad (41)$$

Combining Eq. (40) and (41), yields:

$$\ln\frac{c'}{c_i'} = \frac{k'}{k}\ln\frac{c}{c_i} \qquad (42)$$

Further transformation yields:

$$\ln\frac{c'}{c_i'} - \ln\frac{c}{c_i} = \left(\frac{k'}{k} - 1\right)\ln\frac{c}{c_i} \qquad (43)$$

Rearranging the equation, yields:

$$\ln\frac{c'/c}{c_i'/c_i} = \left(\frac{k'}{k} - 1\right)\ln\frac{c}{c_i} \qquad (44)$$

$$\ln(\delta\mathrm{D} + 1) = (\alpha - 1)\ln\frac{c}{c_i} \qquad (45)$$

where δD here is relative to the initial (D/H) standard rather than the normal Vienna Standard Mean Ocean Water (VSMOW), but it is convenient to transfer these two standards; α (=k'/k) is called the fractionation constant. It can be seen from Eq. (45) that α can be obtained from plotting [ln(δD+1)] against [ln(c/c_i)]. Eq. (45) is the Rayleigh fractionation equation, which is valid only when no source exists.

3.3 Mass balance model

This section shows a mass balance model that has been used in Rice et al. (2011) to calculate the fractionation constant of soil uptake of H_2. But in addition to the fractionation constant, the equation to obtain the isotopic signature of H_2 emitted from the soil is derived.

As discussed in Section 3.2, the Keeling plot is valid when there is no sink while the Rayleigh plot (Rayleigh fractionation equation) is valid when there is no source of H_2. But in our experiments in Cabauw and Speuld, it is very likely that both source and sink of H_2 exist. Thus, it is necessary to derive an equation that is valid when source and sink exist simultaneously.

Based on the mass balance of HH, its time evolution can be expressed as

$$\frac{\mathrm{d\,c}}{dt} = \mathrm{P} - \mathrm{kc} \qquad (46)$$

Where c is the mixing ratio of HH, P is the production rate and k is the removal rate of HH, respectively. The solution is of the form:

$$c = (c_i - c_e)e^{-kt} + c_e \qquad (47)$$

where c, c_i and c_e (= P/k) are the mixing ratio of H_2 at time t, initially and at equilibrium, respectively. The equilibrium mixing ratio of H_2 refers to the mixing ratio where the production rate of H_2 is equivalent to the uptake rate.

From Eq. (47), we can get P and k by fitting an exponential function to the observed time evolution of HH, and further calculate the deposition velocity v_d ($v_d = k \times H$, where H is the effective chamber height).

Similar to equation (47), the solution for time evolution of HD can be expressed as:

$$c' = (c_i' - c_e')e^{-k't} + c_e' \qquad (48)$$

where c', c_i' and c_e' (= P'/k') are the mixing ratio of HD at time t, initially and at equilibrium, respectively.

The transformation of Eq. (47) and (48) yields:

$$\ln\frac{c-c_e}{c_i-c_e} = -\mathrm{kt} \qquad (49)$$

$$\ln\frac{c'-c_e'}{c_i'-c_e'} = -\mathrm{k't} \qquad (50)$$

Combining Eq. (49) and (50), yields:

$$\ln\frac{c'-c_e'}{c_i'-c_e'} = \frac{k'}{k}\ln\frac{c-c_e}{c_i-c_e} \qquad (51)$$

Therefore, the fractionation constant α (= k'/k) and kinetic isotope effect (KIE) ε (=k'/k-1) can be obtained by plotting $[\ln\frac{c'-c_e'}{c_i'-c_e'}]$ against $[\ln\frac{c-c_e}{c_i-c_e}]$. This mass balance model will be used in this thesis to calculate α for our samples.

Besides, if we express c_e in terms of production P and removal rate coefficient k, P=k/c_e and P'=k'/c_e' to Eq. (51), then the ratio P'/P can be obtained by plotting $[c_e'\ln\frac{c'-c_e'}{c_i'-c_e'}]$ versus $[c_e\ln\frac{c-c_e}{c_i-c_e}]$.

$$c_e'\ln\frac{c'-c_e'}{c_i'-c_e'} = \frac{P'}{P}\,c_e\ln\frac{c-c_e}{c_i-c_e} \qquad (52)$$

Once P'/P is known, then the δD of the soil emission can be obtained:

$$\delta\mathrm{D}_{soil} = \frac{P'/P}{2R_{VSMOW}} - 1 \qquad (53)$$

Chapter 4
Results and Discussion

4.1 Results

4.1.1 Background H_2 in Cabauw and Speuld

Fig. 4.1 shows the background mixing ratio and δD of H_2 at the two sampling sites on different days. The results are measurements of the first flask of each experiment. It should be noted that the air samples were collected about 20 cm above the soil, so the background defined here is not the usual background that is defined several meters or tens or hundreds of meters above the ground. As shown in Fig. 4.1, the Cabauw background air samples generally possess higher H_2 mixing ratio (blue circle) and lower δD (red triangle) than Speuld background air samples (green circle for H_2 mixing ratio, violet for δD). The typical values of H_2 mixing ratio and δD are 580 ppb and +120‰ for Cabauw air samples, compared to 440 ppb and +160‰ for Speuld air samples.

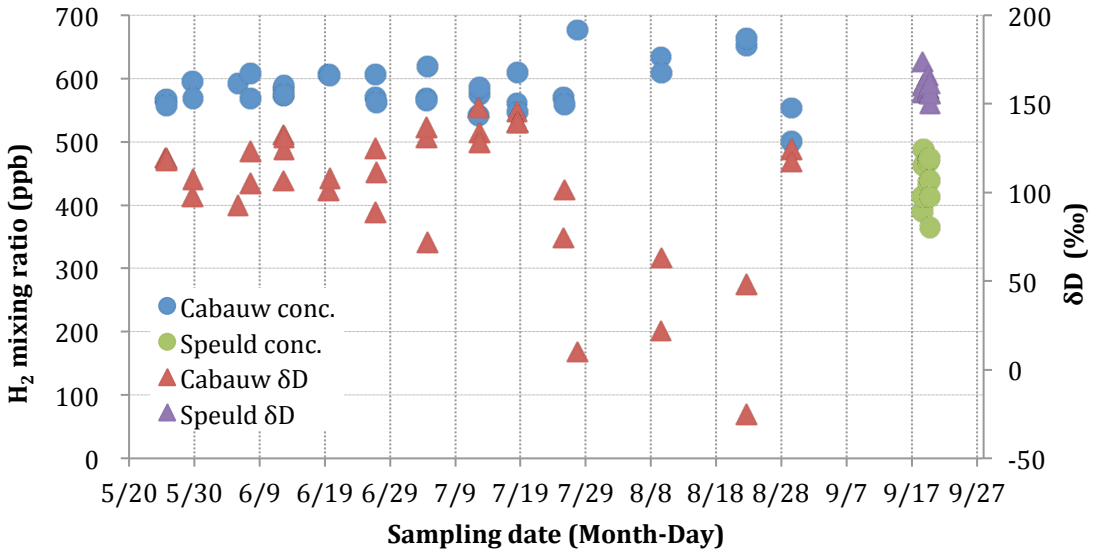

Fig. 4.1 The background (~20 cm above the soil) concentration and δD of H_2 at the two sampling sites on different day. The results are measurements of first flask of each experiment.

4.1.2 Time evolution of H_2, HD and δD for our experiments

Some Cabauw experiments show net soil production of H_2 and some present net soil uptake, while all Speuld experiments show net uptake of H_2. Fig. 4.2 illustrates examples for time evolution of H_2 and HD in

Cabauw and Speuld. Error estimates for H_2, HD and δD are included, which are not always visible for HD and also partly for H_2 because of the very small errors. The error for H_2 is about 3% of its mixing ratio. For HD, the error is 3%~4% of its mixing ratio. The error for δD ranges from 3.2‰ to 19.0‰ for data in this figure.

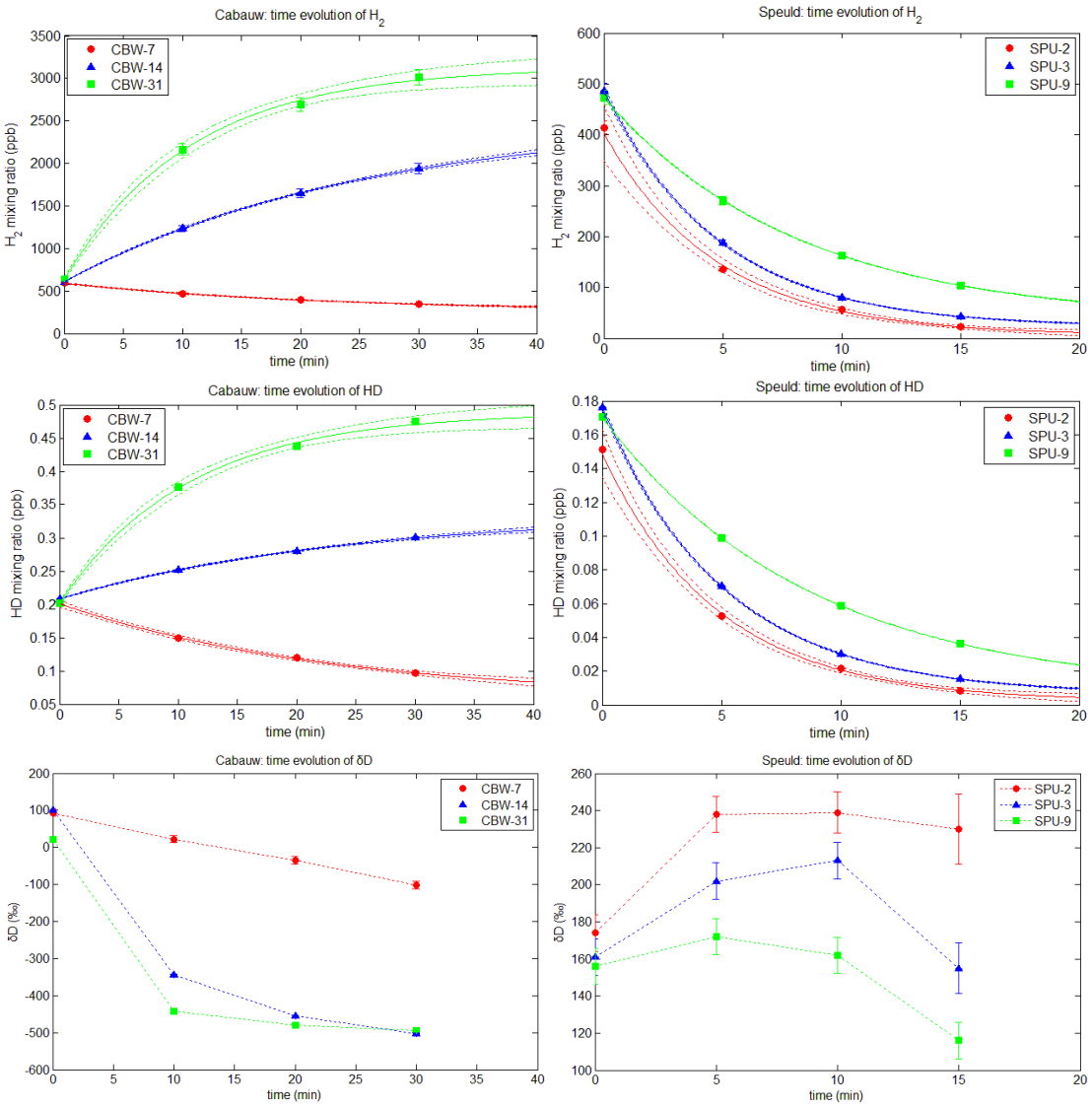

Fig. 4.2 Time evolution of H_2, HD and δD in Cabauw (left panel) and in Speuld (right panel). The H_2 and HD data are fitted with an exponential function of the form: $c = (c_0 - c_e)e^{-kt} + c_e$, where c_0 and c_e are H_2 or HD initially and in equilibrium, k is the soil uptake rate constant of H_2 or HD. The 68% confidence levels for the exponential fit function are shown. Error estimates for H_2, HD and δD are shown, which are not obvious for HD and some H_2 with very small errors. The error for H_2 is about 3% of its mixing ratio. For HD, the error is 3%~4% of its mixing ratio. The error for δD ranges from 3.2‰ to 19.0‰ for data in this figure. The connecting lines in the lower panels are only to guide the eye.

For experiment "CBW-31", the H_2 mixing ratio increases from 634 to 3016 ppb within 30 minutes, accompanied by an increase of the HD

mixing ratio from 0.20 to 0.47 ppb and an decrease of δD from +22‰ to -495‰. In comparison, the net production of H_2 is much smaller for experiment "CBW-14", with an increase in H_2 mixing ratio from 607 to 1939 ppb within 30 minutes, accompanied by an increase in HD mixing ration from 0.21 to 0.30 ppb and decrease of δD from +101‰ to -503‰. Within the same time span for experiment "CBW-7", H_2 mixing ratio drops from 592 to 345 ppb, and the corresponding HD mixing ratio drops from 0.20 to 0.10 ppb and δD declines from +93‰ to -102‰. In contrast, the soil uptake strength of H_2 is always stronger than emission strength in Speuld. For three experiments "SPU-2", "SPU-3" and "SPU-9" shown in Fig. 4.2 as examples, within 30 minutes H_2 mixing ratio decreases from 487, 473 and 413 ppb to 43, 104 and 53 ppb, respectively. Accordingly, HD mixing ratio drops from 0.18, 0.17 and 0.15 ppb to 0.02, 0.04 and 0.02 ppb, respectively. The δD does not show consistent increase or decrease trend for all these three Speuld experiments. For experiment "SPU-2", δD increases from +174‰ to +239‰ within the first 20 minutes and decreases to -230‰ during the last 10 minutes. For experiment "SPU-3", δD increases from +161‰ to +213‰ within the first 20 minutes, but decreases more significantly during the last 10 minutes with a decrease of 58‰ to reach +155‰. For experiment "SPU-9", the decrease of δD occurs earlier. The decrease of δD is observed at time t=20 min. It peaks at time t=10 min from +156‰ to +172‰ and drops to +116‰ at time t=30 min.

Exponential fits for H_2 (Eq. (19)) and HD (Eq. (20)) are applied to the data in Fig. 4.2. The 68% confidence levels for the exponential fit function are shown. As can be seen from Fig. 4.2, the exponential fits represent very well the trend of the data, which supports the constant source and first-order mole fraction dependent sink assumption in Eq. (18-20). But the exponential fit for "CBW-31" and "SPU-2" seems to have large uncertainty as seen from the 68% confidence level estimation. This implies that for some experiments the uptake rate coefficient k and production rate P obtained from the exponential fit can have large uncertainty. This will be further discussed in Section 4.2.

4.1.3 Emission and uptake strength of H_2

By applying exponential fits (see Fig. 4.2 as an example) to the measured H_2, apparent production rate P_{app} and apparent uptake rate constant k_{app} are obtained and then the actual P and k can be retrieved from P_{app} and k_{app} by use of the correction function discussed in Chapter 2. Table 4.1 shows the apparent production rate (P_{app}), apparent uptake rate constant

(k_{app}), apparent emission flux (F_{eapp}), apparent initial uptake flux (F_{uapp}) and apparent deposition velocity (v_{dapp}) for the small-chamber Cabauw experiments, as well as their actual values (P, k, F_e, F_u and v_d). The apparent emission flux F_{eapp} and apparent initial uptake flux F_{uapp} is calculated by used of Eq. (54) and Eq. (55).

$$F_{eapp} = \frac{P_{app} V_{chamber}}{S_{chamber} V_{molar}} \qquad (54)$$

$$F_{uapp} = \frac{k_{app}\, c_i\, V_{chamber}}{S_{chamber} V_{molar}} \qquad (55)$$

where $V_{chamber}$, $S_{chamber}$, V_{molar} and c_i are the volume of the sampling chamber, the area of the sampling chamber, standard molar volume (22.4 L/mol) and initial mixing ratio of H_2, respectively. The actual values P and k are calculated by applying the correction functions to P_{app} and k_{app} discussed in Section 2.2.2 and 2.2.3. Further, the actual values F_e and F_u are calculated by substituting P_{app} with P in Eq. (54) and k_{app} with k in Eq. (55). The experiments are classified as "Net Emission Experiments" (NEE) and "Net Uptake Experiments" (NUE), according to the comparison of H_2 mixing ratio initially and in equilibrium. The NUE include CBW-3, 9, 11, 15, 16, 18, 19, 20, 24, 25, 26, 29, 34, 35 and 37, while the NEE includes CBW-2, 6, 8, 12, 13, 22, 28, 31, 32, 33 and 36.

The emission flux F_e for the NUE was 1.27±0.70 μmol min^{-1} m^{-2}, which is equal to (4.70±2.60)×10^{-8} cm^3 cm^{-2} s^{-1}. This is similar to the flux given in Conrad and Seiler (1980), which is 5-7 ×10^{-8} cm^3 cm^{-2} s^{-1}. However, the emission flux was much higher for the NEE, 5.54±3.89 μmol min^{-1} m^{-2} ((20.67±14.53)×10^{-8} cm^3 cm^{-2} s^{-1}). The deposition velocity v_d for NUE was 0.12±0.07 cm/s with median value 0.12 cm/s, while for NEE it was 0.13±0.13 cm/s with median value 0.08 cm/s. The larger value for NEE is due to the large value 0.48 cm/s for "CBW-6", which may be due to the measurement errors. The v_d becomes 0.10±0.10 cm/s, excluding "CBW-6". The initial uptake flux F_u estimates the uptake strength of H_2 from the backgound atmosphere. It was 1.92±0.05 μmol min^{-1} m^{-2} for NUE and 1.50±0.96 μmol min^{-1} m^{-2} (excluding "CBW-6") for NEE.

Similar to Table 4.1, the P_{app}, k_{app}, F_{eapp}, F_{uapp} and v_{dapp} as well as their actual values P, k, F_e, F_u and v_d for large-chamber Cabauw experiments and all Speuld experiments are shown in Table 4.2 and Table 4.3. A small v_d of 0.02±0.01 was found in net-uptake large chamber experiments in Cabauw while a relatively large v_d of 0.18±0.05 was found in Speuld.

Table 4.1 The apparent production rate (P_{app}), apparent uptake rate constant (k_{app}), apparent emission flux (F_{eapp}), apparent initial uptake flux (F_{uapp}) and apparent deposition velocity (v_{dapp}) for the small-chamber Cabauw experiments, as well as their actual values (P, k, F_e, F_u and v_d). The small-chamber NUE include CBW-3, 9, 11, 15, 16, 18, 19, 20, 24, 25, 26, 29, 34, 35 and 37, while the small-chamber NEE includes CBW-2, 6, 8, 12, 13, 22, 28, 31, 32, 33 and 36. CBW-1 is not included in this thesis because it is the first experiment to test the sampler and only two samples are available. The results for large-chamber Cabauw experiments are shown in Table 4.2. The zero value of P_{app} and c_e for CBW-3 is possibly due to the influence of the sampling processes, which is not discussed in details in this thesis; only the retrieval function of actual P from P_{app} is discussed in Section 2.2.3.

	c_i ppb	c_e ppb	P_{app} ppb min^{-1}	k_{app} min^{-1}	F_{eapp} µmol min^{-1} m^{-2}	F_{uapp} µmol min^{-1} m^{-2}	v_{dapp} cm s^{-1}	P ppb min^{-1}	k min^{-1}	F_e µmol min^{-1} m^{-2}	F_u µmol min^{-1} m^{-2}	v_d cm s^{-1}
CBW-3	566	0	0	0.004	0.00	0.04	0.003	6	0.01	0.11	0.15	0.01
CBW-9	570	412	15	0.04	0.27	0.38	0.02	26	0.06	0.46	0.57	0.04
CBW-11	584	437	44	0.10	0.79	1.06	0.07	65	0.14	1.16	1.50	0.10
CBW-15	605	518	68	0.13	1.22	1.42	0.09	99	0.19	1.77	2.02	0.12
CBW-16	570	269	45	0.17	0.81	1.72	0.11	67	0.25	1.20	2.50	0.16
CBW-18	563	176	41	0.23	0.74	2.36	0.16	63	0.35	1.13	3.57	0.24
CBW-19	569	434	73	0.17	1.30	1.70	0.11	107	0.24	1.90	2.47	0.16
CBW-20	566	374	84	0.23	1.51	2.28	0.15	128	0.34	2.28	3.43	0.23
CBW-24	595	197	13	0.06	0.23	0.69	0.04	21	0.09	0.38	0.98	0.06
CBW-25	557	383	38	0.10	0.68	0.98	0.07	56	0.14	0.99	1.39	0.09
CBW-26	610	332	19	0.06	0.35	0.63	0.04	31	0.08	0.55	0.91	0.06
CBW-29	560	500	93	0.19	1.65	1.85	0.12	137	0.27	2.44	2.72	0.18
CBW-34	651	476	61	0.13	1.09	1.50	0.09	89	0.18	1.60	2.14	0.12
CBW-35	663	384	70	0.18	1.25	2.16	0.12	104	0.27	1.85	3.16	0.18
CBW-37	538	457	45	0.10	0.81	0.95	0.07	66	0.14	1.18	1.35	0.09
MEAN	584	356	47	0.13	0.85	1.32	0.08	71	0.18	1.27	1.92	0.12
STDEV	35	142	27	0.07	0.49	0.71	0.05	39	0.10	0.70	1.05	0.07
CBW-2	566	1511	320	0.21	5.71	2.14	0.14	479	0.32	8.56	3.19	0.21

CBW-6	597	880	374	0.42	6.67	4.53	0.28	700	0.73	12.50	7.75	0.48
CBW-8	610	2716	74	0.03	1.32	0.30	0.02	108	0.04	1.94	0.47	0.03
CBW-12	589	1134	60	0.05	1.08	0.56	0.04	88	0.08	1.57	0.81	0.05
CBW-13	574	814	45	0.06	0.81	0.57	0.04	67	0.08	1.20	0.83	0.05
CBW-22	542	664	146	0.22	2.60	2.13	0.15	220	0.33	3.93	3.19	0.22
CBW-28	570	3384	400	0.12	7.14	1.20	0.08	572	0.17	10.22	1.71	0.11
CBW-31	639	3153	286	0.09	5.11	1.04	0.06	407	0.13	7.27	1.46	0.09
CBW-32	600	4182	309	0.07	5.52	0.79	0.05	438	0.11	7.82	1.13	0.07
CBW-33	608	2171	133	0.06	2.37	0.66	0.04	189	0.09	3.38	0.95	0.06
CBW-36	553	1112	100	0.09	1.78	0.89	0.06	143	0.13	2.55	1.25	0.08
MEAN	586	1975	204	0.13	3.65	1.35	0.09	310	0.20	5.54	1.50[a]	0.10[a]
STDEV	28	1215	134	0.12	2.40	1.22	0.08	218	0.20	3.89	0.90[a]	0.10[a]

[a] Excluding “CBW-6”.

Table 4.2 The production rate (P), uptake rate constant (k), emission flux (F_e), initial uptake flux (F_u) and deposition velocity (v_d) for large-chamber Cabauw experiments. No correction function for k and P is applied for these experiments.

	c_i ppb	c_e ppb	P ppb min^{-1}	k min^{-1}	F_e µmol min^{-1} m^{-2}	F_{u_ini} µmol min^{-1} m^{-2}	v_d cm s^{-1}
CBW-4L	557	247	10	0.04	0.18	0.41	0.02
CBW-5L	595	197	13	0.06	0.23	0.69	0.03
CBW-7L	592	263	12	0.05	0.21	0.48	0.02
MEAN	581	235	12	0.05	0.21	0.52	0.02
STDEV	21	34	1	0.01	0.02	0.15	0.01
CBW-10L	573	1738	131	0.08	2.33	0.77	0.03
CBW-14L	608	2526	99	0.04	1.77	0.43	0.02
CBW-21L	620	3274	263	0.08	4.69	0.89	0.03

CBW-23L	574	1302	198	0.15	3.53	1.55	0.06
CBW-27L	547	763	99	0.13	1.76	1.26	0.05
CBW-30L	673	2977	256	0.09	2.91	0.66	0.04
MEAN	599	2097	174	0.09	2.83	0.93	0.04
STDEV	45	988	75	0.04	1.14	0.41	0.02

Table 4.3 The apparent production rate (P_{app}), apparent uptake rate constant (k_{app}), apparent emission flux (F_{eapp}), apparent initial uptake flux (F_{uapp}) and apparent deposition velocity (v_{dapp}) for the Speuld experiments, as well as their actual values (P, k, F_e, F_u and v_d). The actual values are calculated by applying the correction functions in Section 2.2.2 and 2.2.3. The zero value of P_{app} and c_e for SPU-11 is possibly due to the influence of the sampling processes, which is not discussed in details in this thesis.

	c_i ppb	c_e ppb	P ppb min^{-1}	k min^{-1}	F_{eapp} µmol min^{-1} m^{-2}	F_{uapp} µmol min^{-1} m^{-2}	v_{dapp} cm s^{-1}	P ppb min^{-1}	k min^{-1}	F_e µmol min^{-1} m^{-2}	F_{uapp} µmol min^{-1} m^{-2}	v_d cm s^{-1}
SPU-1	390	23	4.3	0.19	0.08	1.32	0.13	10.2	0.31	0.18	2.13	0.20
SPU-2	414	12	2.9	0.23	0.05	1.72	0.15	7.1	0.38	0.13	2.80	0.25
SPU-3	487	21	4.4	0.21	0.08	1.79	0.14	10.6	0.33	0.19	2.91	0.22
SPU-4	462	47	7.2	0.15	0.13	1.25	0.10	16.4	0.25	0.29	2.03	0.16
SPU-5	436	10	1.3	0.14	0.02	1.07	0.09	7.6	0.22	0.14	1.75	0.15
SPU-6L	321	42	10.7	0.26	0.12	0.94	0.11	10.7	0.26	0.12	0.94	0.11
SPU-7	472	36	4.3	0.12	0.08	1.00	0.08	13.4	0.20	0.24	1.65	0.13
SPU-8	468	29	5.1	0.18	0.09	1.47	0.12	12.5	0.28	0.22	2.37	0.19
SPU-9	473	36	4.5	0.12	0.08	1.05	0.08	13.5	0.20	0.24	1.72	0.14
SPU-10	439	3	0.4	0.13	0.01	1.02	0.09	6.6	0.21	0.12	1.67	0.14
SPU-11	365	0	0.0	0.13	0.00	0.84	0.09	5.0	0.21	0.09	1.37	0.14
SPU-12	413	44	11.6	0.26	0.21	1.93	0.17	20.2	0.43	0.36	3.17	0.29
MEAN	428	25	4.7	0.18	0.08	1.28	0.11	11.17	0.27	0.19	2.04	0.18
STDEV	50	16	3.6	0.05	0.06	0.36	0.03	4.38	0.08	0.08	0.66	0.05

Accordingly, the initial uptake flux F_u in Speuld was about three times of that in net-uptake large chamber experiments. Though weak, there was emission of H_2 from the Speuld forest soil, which can significantly affect the isotopic composition of H_2 for these samples. The emission flux F_e in Speuld was 0.19±0.08 μmol min^{-1} m^{-2}, which is 33 times smaller than that for NEE cases in Cabauw. Because the emission was weak in Speuld, the H_2 mixing ratio in equilibrium was very low here, c_e=25±16 ppb.

4.1.4 Fractionation during soil uptake

4.1.4.1 Speuld results

Based on the mass balance model described in Section 3.3 (Eq. (51)), the fractionation constant α (=k'/k) for soil uptake of H_2 is obtained, by applying the linear fit to $\ln[(c-c_e)/(c_i-c_e)]$ against $\ln[(c'-c_e')/(c_i'-c_e')]$. Table 4.4 lists the uptake rate constant (k), deposition velocity (v_d), fractionation constant (α) as well as its error estimate, kinetic isotope effect (ε), the R^2 of the linear fit for $\ln[(c-c_e)/(c_i-c_e)]$ against $\ln[(c'-c_e')/(c_i'-c_e')]$ based on our mass balance model and the soil cover information for each Speuld experiment. Errors of HH and HD mixing ratio at time t and equilibrium are considered. The R^2 close to 1 suggests that the linear function fits very well with all data for each experiment, which supports the validity of our mass balance model. α varies from 0.923 to 0.963. The mean α is 0.943, with the standard deviation of ±0.013. This is in good agreement with the value given by other authors (Table 1.3), which is 0.943±0.024 by Gerst and Quay (2001), 0.94±0.01 by Rahn et al. (2002) and 0.943±0.005 by Rice et al. (2011). The KIE ε is -57±13‰.

To obtain a more straightforward view of calculation of α with our mass balance model, we show $\ln[(c-c_e)/(c_i-c_e)]$ against $\ln[(c'-c_e')/(c_i'-c_e')]$ for all Speuld experiments in Fig. 4.3. A linear fit is applied to all the data and the overall α is 0.939±0.001, which is slightly different from 0.943±0.013, but it has a smaller error. Rice et al. (2011) suggested the overall α to be the fractionation constant of their soil experiments. But it is suggested that the average of all experiments (0.943±0.013) rather than fit all data with one linear fit (0.939±0.001) is more representative for the fractionation constant in Speuld, since the fit to all data can weaken the signal of each experiment.

Table 4.4 The uptake rate constant (k), deposition velocity (v_d), fractionation constant (α) as well as its error estimate, KIE (ε), R^2 of the linear fit for $\ln[(c-c_e)/(c_i-c_e)]$ against

$\ln[(c'-c_e')/(c_i-c_e')]$ based on our mass balance model and soil cover information for each Speuld experiment. The first experiment "SPU-1" is not included here as the δD of this experiment might have large uncertainty since the sampling time for this experiment was longer time than other Speuld samplings and the H_2 mixing ratio was very low for the final flask of this experiment.

	k min^{-1}	v_d $cm\ s^{-1}$	α =k'/k	KIE ε ‰	Error α	R^2	soil cover
SPU-2	0.38	0.25	0.963	-37	0.012	0.9998	D. fir, needles
SPU-3	0.33	0.22	0.942	-58	0.003	1.0000	D. fir, moss
SPU-4	0.25	0.16	0.923	-77	0.005	1.0000	D. fir, moss
SPU-5	0.22	0.15	0.927	-74	0.004	1.0000	D. fir, moss
SPU-6	0.26	0.11	0.949	-51	0.010	0.9999	D. fir, moss
SPU-7	0.20	0.13	0.947	-53	0.003	1.0000	beech, leaves
SPU-8	0.28	0.19	0.948	-52	0.007	0.9999	leaves removed
SPU-9	0.20	0.14	0.937	-63	0.003	1.0000	beech, leaves
SPU-10	0.21	0.14	0.932	-68	0.012	0.9998	spruce, moss
SPU-11	0.21	0.14	0.951	-49	0.021	0.9994	spruce, needles
SPU-12	0.43	0.29	0.959	-41	0.011	0.9998	needles removed
MEAN	0.27	0.18	0.943	-57	0.008	---	
STDEV	0.08	0.05	0.013	13	0.006	---	

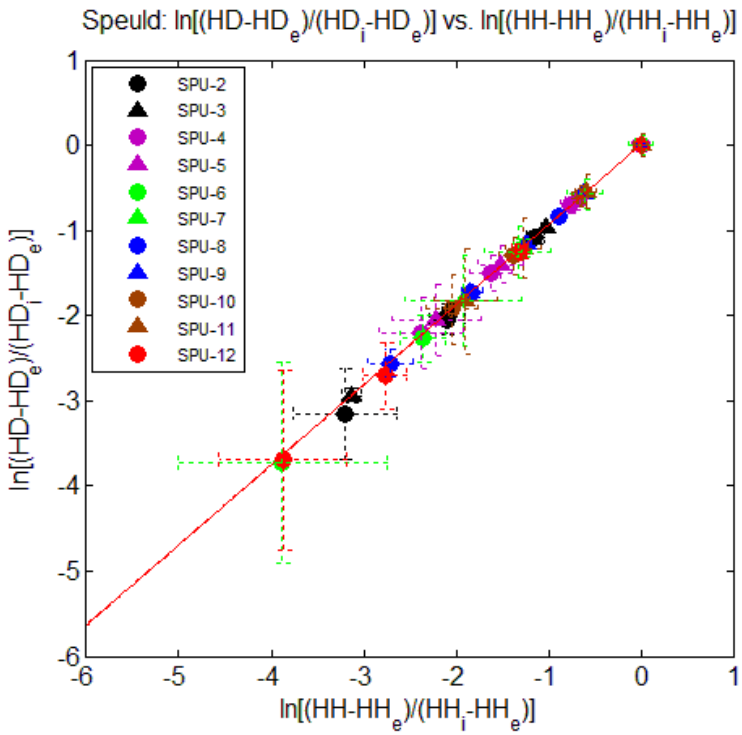

Fig. 4.3 The $\ln[(c-c_e)/(c_i-c_e)]$ against $\ln[(c'-c_e')/(c_i-c_e')]$ for all Speuld experiments in Table 4.4. A linear function is applied to all data and the slope of the linear curve refers to the fractionation constant. Error bars in both x and y direction for each data points are considered. The 95% confidence level is not visible because the linear correlation fits very well with the data.

It is interesting to look at the factors that may affect α. Rice et al. (2011) proposed a significant positive correlation between KIE ε and deposition

velocity v_d, which means a positive correlation between α and v_d. This correlation is investigated in this thesis as well (Fig. 4.4). But our Speuld experiments suggest that the correlation is weak (p-value > 0.5).

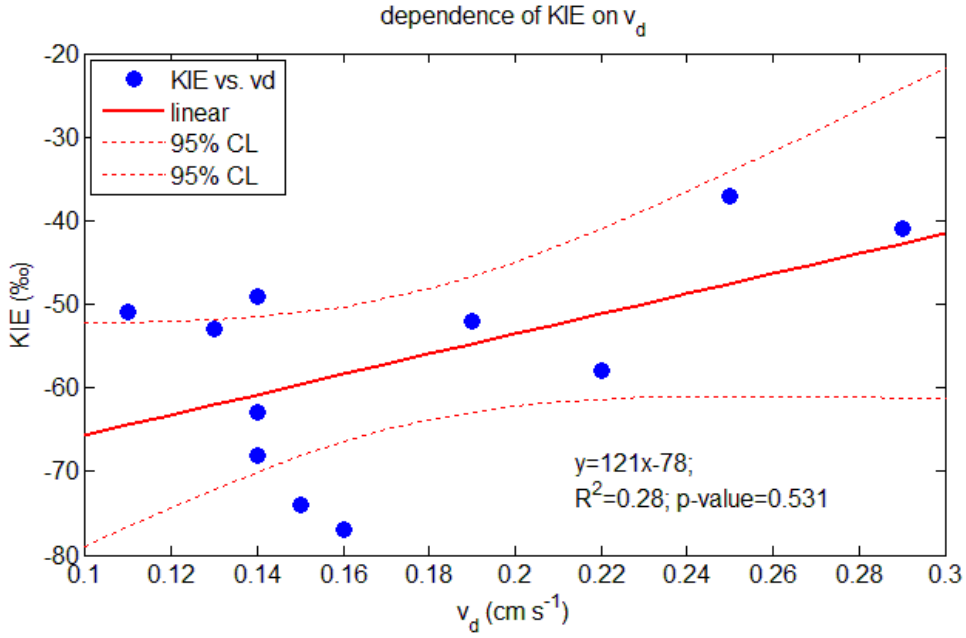

Fig. 4.4 The dependence of KIE on v_d. A linear fit (solid line) with 95% confidence level (dotted line) is applied, with correlation function KIE = 121v_d - 78. But the correlation is weak (R^2=0.28, p-value > 0.5).

To further investigate the factors determining α, information about the soil cover is provided. Though different types of soil cover show similar α and ε in general, a slight difference exists. In the region of Douglass fir, overall, soil covered with moss shows smaller α (more negative ε) than that with needles. Similarly, in spruce forest region, smaller α occurs for soil covered with moss rather than needles. In addition, the removal of leaves or needles does not significantly change α and ε. It suggests that the removal of obstacles (leaves or needles) above the soil might have no (or insignificant) influence on the isotope fractionation of soil uptake of hydrogen.

4.1.4.2 Cabauw results

Table 4.5 lists the fractionation constant (α) as well as its error estimate for selected Cabauw experiments. The α is calculated based on the mass balance model described in Section 3.3, by applying linear fit to $\ln[(c-c_e)/(c_i-c_e)]$ against $\ln[(c'-c_e')/(c_i'-c_e')]$. The R^2 of the linear fit is given. In addition, the H_2 mixing ratio in equilibrium (c_e), deposition velocity (v_d), and soil cover information for each selected Cabauw experiments are

given in Table 4.5 as well. Cases with comparable emission and uptake of H_2 and HD are not included since H_2 increases or decreases very slowly (less than 10 ppb within 10 minutes that is comparable to the uncertainty from the measurement). In addition, cases with abnormal behavior of HH, HD or δD that do not follow an exponential increase or decrease with time are not included here. The α is calculated to be 0.977±0.051, which is comparatively higher than that of Speuld experiments (0.943±0.013). The α has a wide range from 0.903 to 1.093 for the individual experiments. The unusual α (>1) is observed for "CBW-9" and "CBW-14". Similar to Fig. 4.3, Fig. 4.5 shows the overall α based on the mass balance model described in Section 3.3 for all the selected Cabauw experiments. The overall α is 0.953±0.006. The α for Cabauw experiments is not dependent on v_d (not shown here). It is suggested that the average of all experiments (0.977±0.051) rather than fit all data with one linear fit (0.953±0.006) is more representative for the fractionation constant in Cabauw. If all experiments are in one fit, their weight on the slopes depends on how much has been removed, so experiments with a lower c_e have a larger weight than experiments with a higher c_e. This is not what it should be to get an average and all experiments should be weighted equally.

Table 4.5 The H_2 mixing ratio in equilibrium (c_e), deposition velocity (v_d), fractionation constant (α) as well as its error estimate, kinetic isotope effect (ε), the R^2 of the linear fit for $\ln[(c-c_e)/(c_i-c_e)]$ against $\ln[(c'-c_e')/(c_i'-c_e')]$ based on our mass balance model and soil cover information for selected Cabauw experiments. Cases with comparable emission and uptake of H_2 and HD are not included since H_2 increases or decreases very slowly (less than 10 ppb within 10 minutes that is comparable to the uncertainty from the measurement). In addition, cases with abnormal behavior of HH, HD or δD that does not follow exponential increase or decrease with time are not included here.

	c_e ppb	v_d cm s^{-1}	α =k'/k	KIE ε ‰	Error α	R^2	soil cover
CBW-5	194	0.03	0.903	-97	0.007	0.9999	few clover, grass
CBW-7	259	0.02	0.972	-28	0.008	0.9999	few clover, grass
CBW-9	415	0.04	1.093	93	0.010	0.9999	grass
CBW-14	2510	0.02	1.033	33	0.009	0.9999	clover, grass
CBW-16	268	0.16	0.988	-12	0.013	0.9999	bare soil, few grass
CBW-18	176	0.24	0.983	-17	0.013	0.9999	grass
CBW-19	434	0.16	0.941	-60	0.015	0.9999	grass
CBW-20	373	0.23	0.934	-66	0.041	0.9994	bare soil
CBW-21	3268	0.03	0.949	-51	0.006	0.9999	clover, grass
CBW-30	2989	0.04	0.969	-31	0.009	0.9999	clover, grass
CBW-31	3132	0.09	0.984	-16	0.004	1.0000	clover, grass
MEAN	1274	0.10	0.977	-23	0.012	---	
STDEV	1363	0.09	0.051	51	0.010	---	

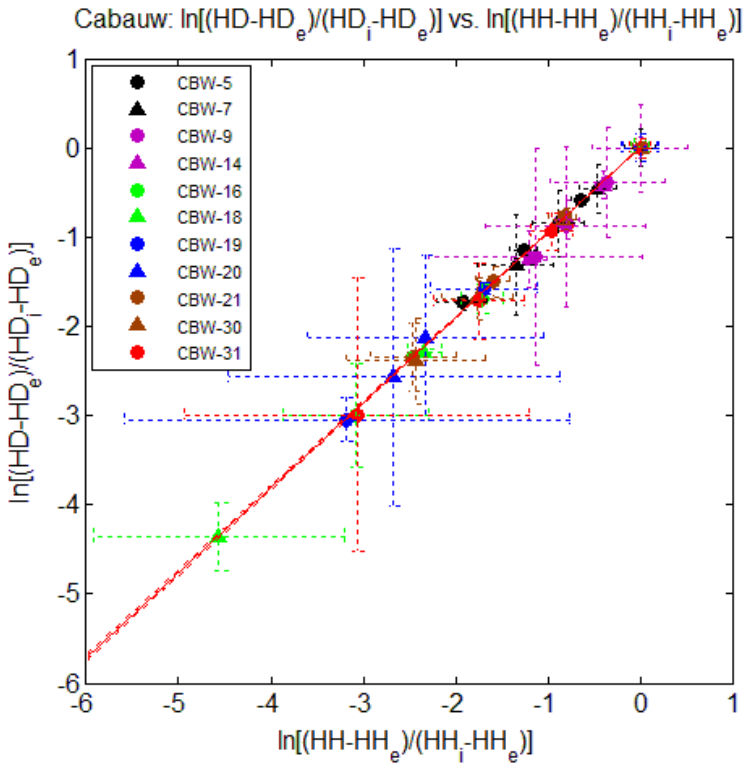

Fig. 4.5 The calculation of mean fractionation constant based on the mass balance model described in Section 3.3 (Eq. (23)) for some Cabauw experiments. The 95% confidence level is shown.

4.1.5 Isotopic signature δD of H_2 emitted from the soil

4.1.5.1 δD_{soil} calculated from the mass balance model

Section 3.3 discusses the mass balance model to obtain the isotopic signature δD of H_2 emitted from the soil (here denoted as δD_{soil}), as shown in Eq. (52) and Eq. (53).

$$c_e' \ln\frac{c' - c_e'}{c_i' - c_e'} = \frac{P'}{P}\, c_e \ln\frac{c - c_e}{c_i - c_e} \qquad (52)$$

$$\delta D_{soil} = \frac{P'/P}{2R_{VSMOW}} - 1 \qquad (53)$$

where c, c_i and c_e are mixing ratio of H_2 at time t, initially and at equilibrium, and c', c_i' and c_e' are those of HD. P and P' are the emission rate of H_2 and HD from the soil and R_{VSMOW} is the D/H ratio of the Standard (Vienna) Mean Ocean Water. Fig. 4.6 shows three examples in Cabauw of getting P'/P ratio from the plot with $c_e' \ln\frac{c' - c_e'}{c_i' - c_e'}$ against

$c_e \ln\frac{c-c_e}{c_i-c_e}$, while three examples in Speuld are shown in Fig. 4.7. It can be seen that the linear correlation fits the data very well for each experiment in both Cabauw and Speuld. The slope of the linear fit represents P'/P, which is 0.000218, 0.000139, 0.000154, 0.000365, 0.000267 and 0.000200 for "CBW-7", "CBW-14", "CBW-31", "SPU-2", "SPU-3" and "SPU-9" respectively. The P'/P ratio and corresponding δD_{soil} for all the experiments in Table 4.4 and Table 4.5 are shown in Table 4.6 and Table 4.7. The δD_{soil} ranges from -441‰ to +196‰ for the Speuld experiments and from -600‰ to +161‰ for Cabauw experiments. For cases with strong emission, which are "CBW-14", "CBW-21", "CBW-30" and "CBW-31", the hydrogen emitted from the soil is very deuterium depleted, with δD to be -555‰, -600‰, -583‰ and -507‰ respectively.

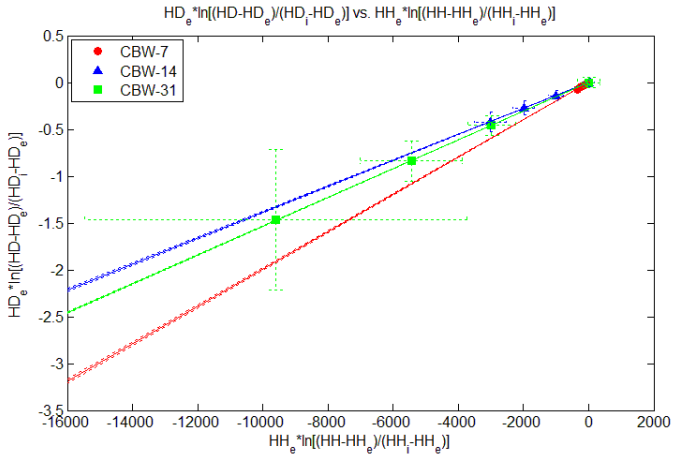

Fig. 4.6 Plot of $c_e' \ln\frac{c'-ce'}{ci'-ce'}$ against $c_e \ln\frac{c-ce}{ci-ce}$ for three soil experiments in Cabauw. The slope of the linear fit lines returns P'/P (see text).

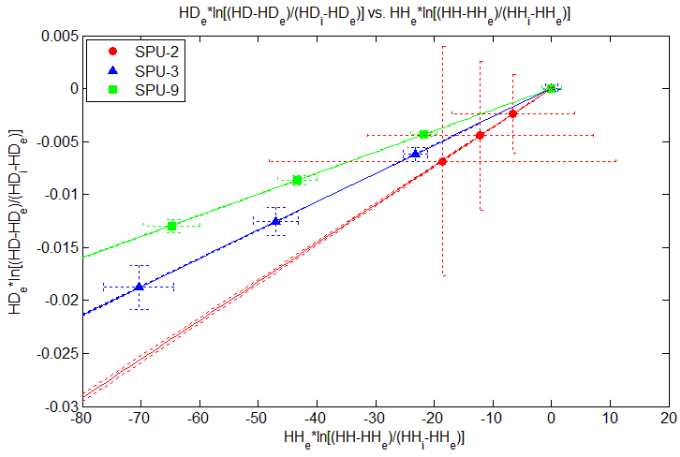

Fig. 4.7 Plot of $c_e' \ln\frac{c'-ce'}{ci'-ce'}$ against $\frac{P'}{P}\, c_e \ln\frac{c-ce}{ci-ce}$ for three soil experiments in Speuld. The slope of the linear fit lines returns P'/P (see text).

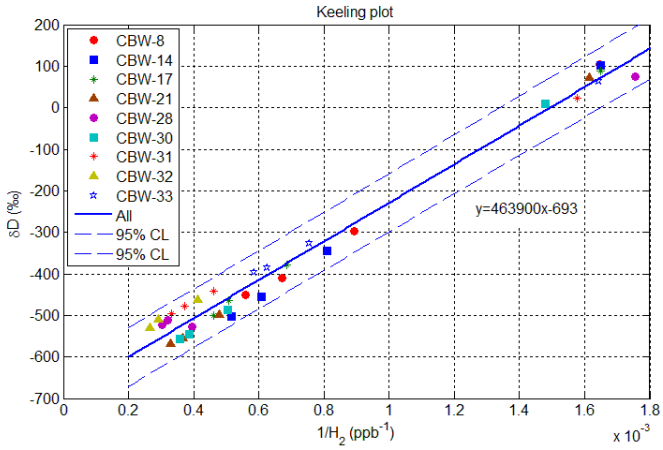

Fig. 4.8 Keeling plot to obtain the isotopic signature of biogenic H_2 emission. Only cases with strong H_2 emission flux and weak uptake rate constant (k/P<0.0005) are included.

Table 4.6 The P'/P ratio and corresponding δD of the soil emission in Speuld. The production rate P for SPU-11 is estimated to be zero as shown in Table 4.3.

	P'/P	R^2	δD (‰)	Error δD (‰)
SPU-2	0.000365	0.9998	171	15
SPU-3	0.000267	1.0000	-142	3
SPU-4	0.000304	1.0000	-23	4
SPU-5	0.000188	1.0000	-398	2
SPU-6	0.000373	0.9999	196	13
SPU-7	0.000262	1.0000	-160	3
SPU-8	0.000248	1.0000	-203	5
SPU-9	0.000200	1.0000	-360	2
SPU-10	0.000174	0.9998	-441	7
SPU-11	---	---	---	---
SPU-12	0.000330	0.9999	58	12
MEAN	0.000271	---	-130	---
STDEV	0.000071	---	229	---

Table 4.7 The P'/P ratio and corresponding δD of the soil emission in Cabauw.

	P'/P	R^2	δD (‰)	Error δD (‰)
CBW-5	0.000199	0.9999	-360	4
CBW-7	0.000218	0.9999	-299	5
CBW-9	0.000362	0.9999	161	11
CBW-14	0.000139	0.9999	-555	4
CBW-16	0.000314	0.9999	8	14
CBW-18	0.000331	0.9999	61	16
CBW-19	0.000311	0.9999	0	16
CBW-20	0.000319	0.9994	22	45
CBW-21	0.000125	0.9999	-600	3
CBW-30	0.000130	0.9999	-583	4
CBW-31	0.000154	1.0000	-507	2
MEAN	0.000236	---	-241	---
STDEV	0.000092	---	296	---

4.1.5.2 δD_{soil} calculated from the Keeling plot

In the absence of production, the isotopic signature of biogenic H_2 emission can be obtained from the Keeling plot (Section 3.2):

$$\delta D_{measured} = \delta D_{source} + \frac{1}{c_{measured}} c_{bg}(\delta D_{bg} - \delta D_{source}) \qquad (54)$$

where $\delta D_{measured}$, δD_{source}, δD_{bg}, $c_{measured}$ and c_{bg} are measured δD, δD of the source, δD of the background, measured H_2 mole fraction and background H_2 mole fraction respectively.

Fig. 4.8 shows the Keeling plot for selected experiments in Cabauw, including all experiments with strong H_2 emission flux and weak uptake rate constant (k/P<0.0005). The intercept of the Keeling plot represents the δD of the H_2 source. For all experiments shown in Fig. 4.8, δD ranges from -795‰ to -628‰. The overall δD obtained from all data in Fig. 4.6 is -693±71‰, which is similar to what is found for biogenic H_2 in Walter et al. (2011).

However, due to the influence of soil uptake on the Keeling plot, the δD of soil emitted H_2 obtained from the Keeling plot would underestimate the actual δD of soil emitted H_2, which will be discussed in Section 4.2.

4.2 Discussion

4.2.1 Emission and uptake strength

The emission flux F_e for NUE in Cabauw is 1.27±0.70 μmol min^{-1} m^{-2}, which is equal to (4.70±2.60)×10^{-8} cm^3 cm^{-2} s^{-1} when applying the standard molar volume 22.4 L/mol. The flux obtained from the NUE is similar to the flux given in Conrad and Seiler (1980), which is 5-7 ×10^{-8} cm^3 cm^{-2} s^{-1}. By applying the same method as Conrad and Seiler used, the total H_2 production from land is 3.4±1.6 Tg yr^{-1}, which is similar to the value used in other studies (Novelli et al., 1999; Ehhalt and Rohrer, 2009 and the references therein). However, the emission flux is much higher for NEE in Cabauw, with F_e to be 5.54±3.89 μmol min^{-1} m^{-2} ((20.67±14.53)×10^{-8} cm^3 cm^{-2} s^{-1}). The H_2 emission calculated from this flux is 14.1±8.8 Tg yr^{-1}. It can be seen that the emission flux of H_2 from soil can be very large. Many H_2 emission flux estimates are based on the value provided by Conrad and Seiler (1980) who conducted very few experiments of H_2 emission three decades ago. More experiments should

be conducted to get more data about the emission of H_2 from soil to constrain the global H_2 budget.

The deposition velocity v_d for NUE is 0.12±0.07 cm/s with median value 0.12 cm/s, while for NEE it becomes 0.10±0.10 cm/s with median value 0.08 cm/s. The weaker uptake strength for NEE cases may be related to the high H_2 mixing ratio in soils when there is strong emission (Conrad and Seiler, 1980). In this case, the microbes and enzymes consume a lot of H_2 produced within the soil and may not be able to consume a lot of H_2 from the atmosphere.

4.2.2 Fractionation constant α

The fractionation constant α for Cabauw experiments is generally larger than that for Speuld experiments as shown in Table 4.4 and Table 4.5. The α is even larger than 1 for "CBW-9" and "CBW-14", which was never reported in other studies before. In this thesis, no detailed explanation for the abnormal α of these two experiments can be given. It is possible that this is due to the measurement errors, however no obvious errors could be detected. If these two experiments are excluded in Table 4.5, then α for the selected Cabauw experiments in Table 4.5 is 0.958±0.028, which is slightly higher than that for the Speuld experiments (0.943±0.013).

One may be curious about the effect of our sampling method on the value of α. As discussed in Section 2, the correlation between the actual k and apparent k (k_{app}) is almost linear, which is shown in Eq. (24) and Eq. (25) for Cabauw experiments and Speuld experiments.

$$k_{CBW} = 1.15k_{app}^2 + 1.20k_{app} + 0.01 \qquad (24)$$

$$k_{SPU} = 0.95k_{app}^2 + 1.28k_{app} + 0.03 \qquad (25)$$

When k_{app} is about 0.1 min^{-1}, which is the general case for our experiments, Eq. (24) and Eq. (25) can be approximated as Eq. (55) and Eq. (56).

$$k_{CBW} = 1.20k_{app} \qquad (55)$$

$$k_{SPU} = 1.28k_{app} \qquad (56)$$

Eq. (55) and Eq. (56) can be applied to both the uptake rate of HH and HD. Since α is equal to k'/k, the apparent α calculated from the experiment data should be the same as the actual α. Thus, we suggest that the apparent α value of 0.943±0.013 and 0.977±0.051 calculated from our experiments in Speuld and Cabauw can be used as the actual α value.

4.2.3 Isotopic signature δD of H_2 emitted from the soil

As shown in Table 4.6 and Table 4.7, the δD of H_2 emitted from the soil is always larger than the theoretical value calculated for biological production of H_2 (~-700‰), which has also been verified experimentally in dedicated production experiments (Walter et al., 2012). The R^2 values of the linear fits close to one indicate the goodness of the linear fits. Our hypothesis to explain this is that part of the H_2 emitted from the soil is consumed by microbes or enzymes in the soil before entering into the atmosphere, and isotopic fractionation processes happen during this decomposition process that the microbes or enzymes prefer HH rather than HD.

Fig. 4.8 shows the value of δD_{soil} by use of the Keeling plot, which is estimated from the slop of the Keeling plot with the value of -693±71‰. It should be noted that only experiments with strong soil emission and weak soil uptake of H_2 are included in Fig. 4.8 to calculate the δD of the soil emission. Other Cabauw experiments with weaker soil emission and stronger soil uptake show abnormal values of δD_{soil}, sometimes even lower than -1000‰ (Fig. 4.9). Of course the δD value cannot be smaller than -1000‰, otherwise the D/H ratio of the sample air is negative, which is impossible. Thus, the δD of the soil emission calculated from the Keeling plot for our experiments does not represent the actual isotopic signature of the soil emission. This is probably the case since we use Keeling plot to get the source signature when the uptake is present, which should not be applied.

If we know the effect of uptake on the Keeling plot and get the correction function to retrieve the actual δD_{soil} (δD_{soil_true}) from the apparent δD_{soil} (δD_{soil_app}) calculated from the Keeling plot, then we can still use the Keeling plot to get information of the isotopic signature of the soil emission. Here we make a model to investigate this effect. Fig. 4.10 shows one of our simulation results, which is the influence of the k/P ratio on the Keeling plot with input of δD_{soil_true} of -700‰ and fractionation constant α of 0.94. It can be seen that the calculated δD_{soil} decreases from -700‰ to -1397‰ with the increase of k/P ratio from 0 to

0.0009. In principle, if we know the k/P ratio for our experiment, the apparent δD of the soil emission from the Keeling plot and the relation between the actual δD and apparent δD, we can retrieve the actual δD of the soil emission. Fig. 4.11 shows three examples about the change of the δD of the soil emission obtained from the Keeling plot as a function of k/P ratio. This provides the possibility to retrieve the actual isotopic signature of soil H_2 emission. Using the correlation between δD_{soil_ture} and apparent δD_{soil_app}, we calculate that δD_{soil_true} for experiments shown in Fig. 4.8 is about -550‰. In this thesis, no details about this calculation would be shown.

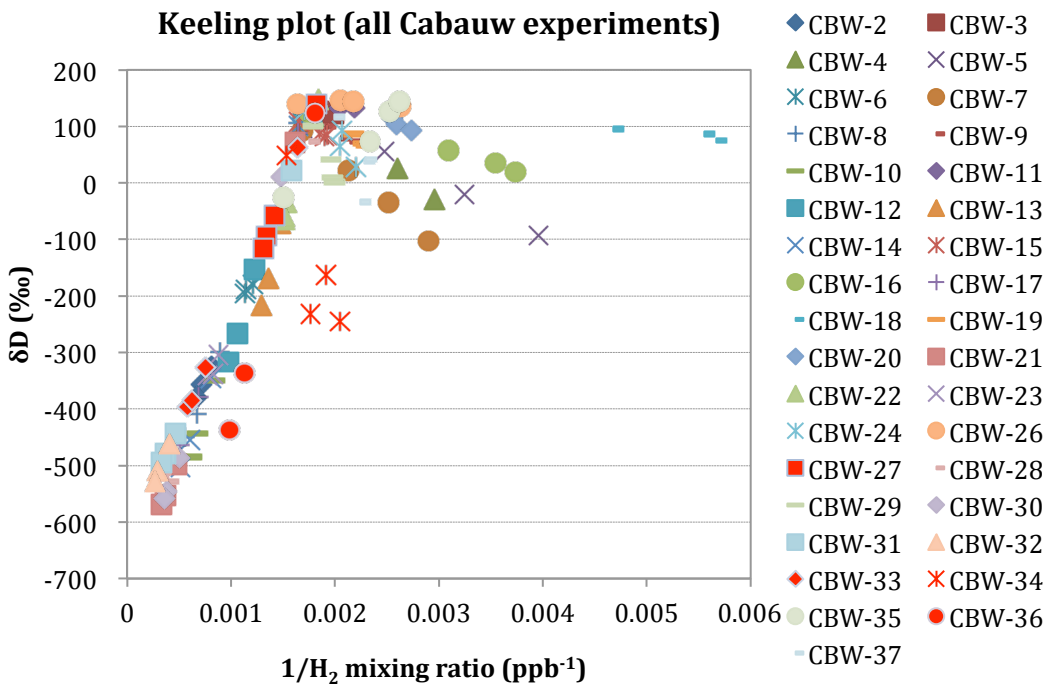

Fig. 4.9 The Keeling plot for all Cabauw experiments. CBW-1 is not included here because it is a test sampling and only 2 air samples are available.

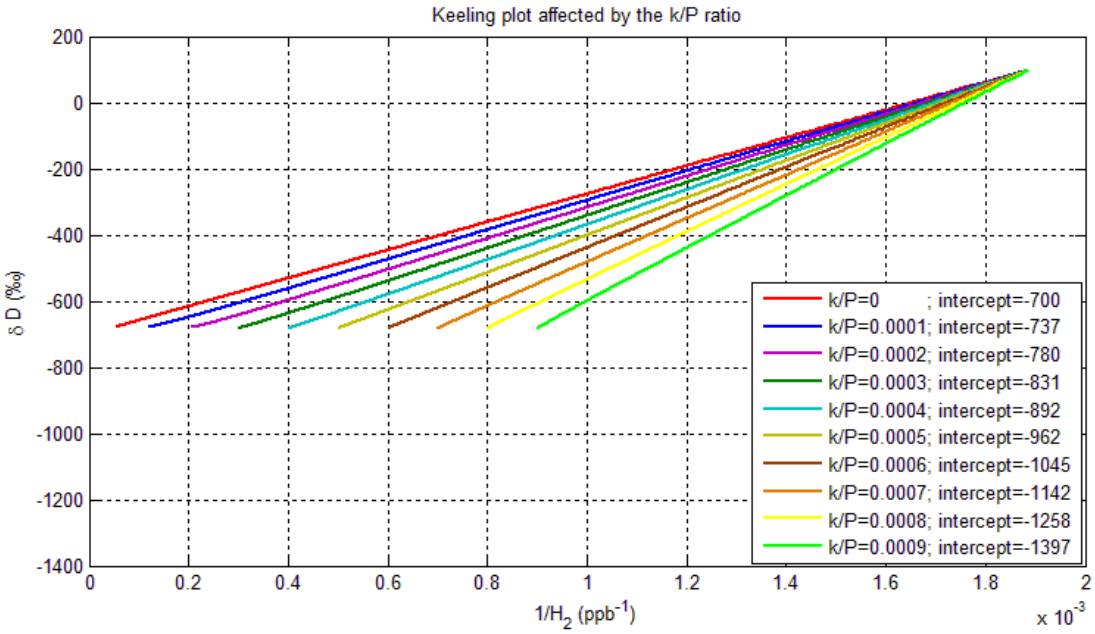

Fig. 4.10 Simulation results on the influence of k/P ratio on the Keeling plot. The δD of the soil emission used in the model is -700‰ and the fractionation constant α is 0.94.

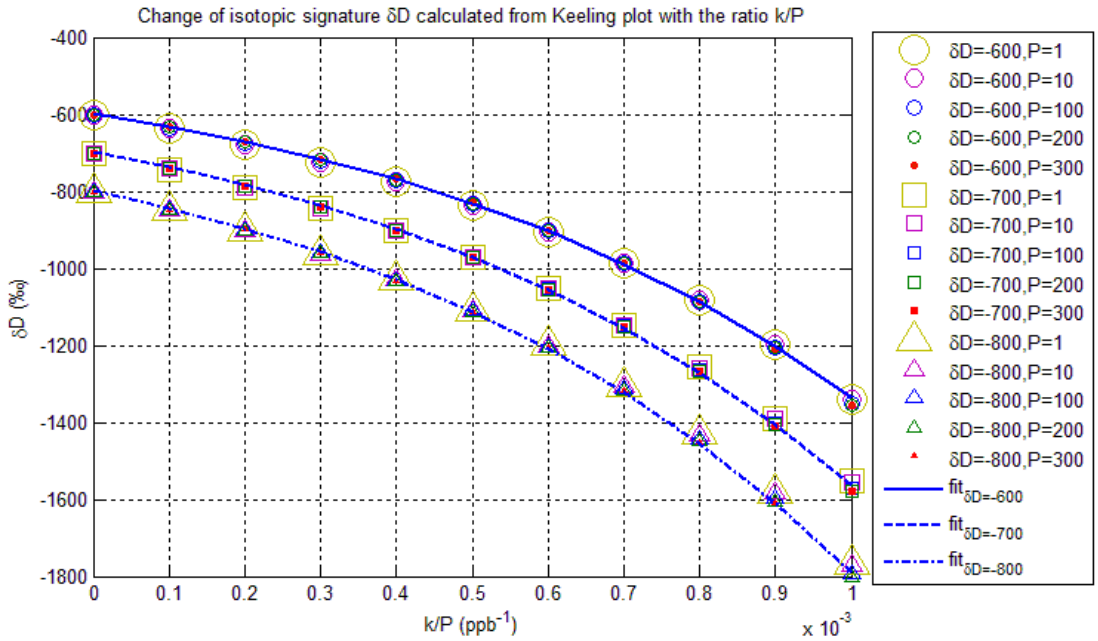

Fig. 4.11 The change of δD_{soil} obtained from the Keeling plot as a function of the ratio k/P. Three fits are applied to the data with input δD_{soil} of -600‰, -700‰ and -800‰, respectively. The function for these three fits is: $\delta D_{soil\_app} = \frac{\delta D_{soil\_true}}{3} e^{1550k/P}$. The error estimation for this function is not given in this thesis.

Chapter 5
Conclusion and Outlook

This thesis investigated the isotope effects associated with production and uptake of molecular hydrogen (H_2) in the atmosphere by soil. Our aim was to learn more about the fractionation constant α and isotopic signature of H_2 emitted from the soil δD_{soil} from experiments in Cabauw and Speuld. A total of 176 air samples were collected from the two sites, which makes this study the most extensive investigation of the isotope effects in soil uptake and deposition so far.

The volume of the sample flasks attached to the soil chamber is not negligible compared to the soil chamber. Therefore, the deposition rate coefficient and production rate cannot be simply derived from an exponential fit to the flask data. An analytical model has been developed to simulate the sampling process. This model is used to derive a correction function that allows to calculate the actual deposition rate coefficient and production rate from the apparent values which are produced by the exponential fit.

H_2 mixing ratios in the flasks from the soil deposition experiments are in many cases far lower than ambient H_2 mixing ratios, for which the analytical system was developed. Therefore, the non-linearity of the analytical system was thoroughly tested. The peak integration routine on the IRMS was optimized for small sample sizes and a correction function for samples with very low mixing ratios was derived. This allows measurement of all samples from our soil uptake experiments, including a realistic assessment of the error bars for low peak areas in the IRMS.

The experiments cover a wide range of conditions from almost exclusively uptake to very strong emission of H_2. The superposition of deposition and production complicates the analysis with simple traditional process models like Rayleigh plot and Keeling plot analysis. Therefore, the mass balance model developed by Rice et al. (2011) was used for evaluation. In addition, the temporal evolution of H_2 and HD were modeled separately in order to deduce the results.

The fractionation factor α is found to be 0.943 ± 0.013 for Speuld forest soil experiments and 0.977 ± 0.051 for Cabauw grassland experiments. The difference in α between these two locations may be due to different soil type, with different temperature, water content and microbes or enzymes. The relationship between the α value and these factors as well

as how these factors affect α are not discussed in this thesis. A positive correlation between α and deposition velocity v_d is not found in our experiments, which disagrees with the suggestion by Rice et al. (2011). From two of our Speuld experiments, α stays unchanged (or very slightly changed) after the removal of leaves or needles above the soil, which suggests the diffusion through the layer of leaves or needles is not the main factor controlling the soil uptake fractionation processes. But it should be noted that only two soil cover removal experiments were conducted and more experiments are needed to support this hypothesis.

The isotopic signals shown in our air samples suggest that there is generally H_2 emitted from the soil. In Cabauw, the emission strength can be very large at locations where clover is present. In these experiments, the δD value decreases with time, which indicates there is a deuterium-depleted H_2 source from the soil. This source is expected to be biogenic H_2 produced through nitrogen fixation inside the soil. The expected δD_{soil} for this biogenic H_2 is around -700‰, (Walter et al., 2011). By applying the Keeling plot to selected Cabauw experiments with strong emission and weak uptake of H_2, we obtained the apparent isotopic signature δD_{soil_app} of -693±71‰. But this number may overestimate the actual isotopic signature δD_{soil_true}, since we apply Keeling plot analysis to experiments with a mixture of soil production and removal processes rather than a single source without removal. A simple model is developed to quantify the effect of removal on the Keeling plot intercept, as a function of k/P. Therefore, it may still be possible to retrieve the true value of δD_{soil} from the Keeling plot, but this requires further work. As an alternative approach, we used a mass balance model to obtain δD_{soil} from each single experiment. The results suggests that δD_{soil} varies over a surprisingly wide range from about -600‰ to +200‰, and it is always larger than -700‰. One possible explanation is that part of the H_2 produced during nitrogen fixation within the soil is consumed by the microbes or enzymes within the soil before entering into the atmosphere, and the microbes or enzymes prefer HH than HD. This will necessitate more investigation in the future.

For future work, it would be interesting to investigate the effects of temperature, soil water content and soil cover on α. Besides, all our experiments suggest a source of H_2 from the soil and that is why we could not apply the Rayleigh fractionation equation to calculate α. The potential future experiments with only sink of H_2 would help us better constrain the α value. More experiments with strong emission and weak uptake of H_2 are needed to better understand the isotopic signature of H_2 produced from the soil.

References

Batenburg A M, Walter S, Pieterse G, et al. Temporal and spatial variability of the stable isotopic composition of atmospheric molecular hydrogen: observations at six EUROHYDROS stations[J]. Atmos. Chem. Phys, 2011, 11: 6985-6999.

Batenburg, A. M., 2012. Global scale observations of atmospheric molecular hydrogen and its stable isotopic composition, PHD Thesis, Utrecht University, Utrecht, The Netherlands.

Beljaars A. C. M. and F. C. Bosveld (1997). Cabauw data for the validation of land surface parametrization schemes. J. of Climate, 10, 1172-1193.

Bottinga Y. Calculated fractionation factors for carbon and hydrogen isotope exchange in the system calcite-carbon dioxide-graphite-methane-hydrogen-water vapor[J]. Geochimica et Cosmochimica Acta, 1969, 33(1): 49-64.

Burns, R. C., and R. W. F. Hardy, Nitrogen fixation in Bacteria and Higher Plants, Springer, New York, 1975.

Chen H, Winderlich J, Gerbig C, et al. Validation of routine continuous airborne CO2 observations near the Bialystok Tall Tower[J]. Atmospheric Measurement Techniques, 2012, 5(4): 873-889.

Conrad R, Seiler W. The role of hydrogen bacteria during the decomposition of hydrogen by soil[J]. FEMS Microbiology Letters, 1979, 6(3): 143-145.

Conrad R, Seiler W. Contribution of hydrogen production by biological nitrogen fixation to the global hydrogen budget[J]. Journal of Geophysical Research: Oceans (1978–2012), 1980, 85(C10): 5493-5498.

Conrad R, Seiler W. Decomposition of atmospheric hydrogen by soil microorganisms and soil enzymes[J]. Soil Biology and Biochemistry, 1981, 13(1): 43-49.

Conrad R, Weber M, Seiler W. Kinetics and electron transport of soil hydrogenases catalyzing the oxidation of atmospheric hydrogen[J]. Soil Biology and Biochemistry, 1983, 15(2): 167-173.

Conrad R, Seiler W. Influence of temperature, moisture, and organic carbon on the flux of H2 and CO between soil and atmosphere: Field studies in subtropical regions[J]. Journal of Geophysical Research, 1985, 90(D3): 5699-5709.

Conrad R. Compensation concentration as critical variable for regulating the flux of trace gases between soil and atmosphere[J]. Biogeochemistry, 1994, 27(3): 155-170.

Constant P, Poissant L, Villemur R. Isolation of Streptomyces sp. PCB7, the first microorganism demonstrating high-affinity uptake of tropospheric H2[J]. The ISME journal, 2008, 2(10): 1066-1076.

Constant, P., Chowdhury, S. P., Pratscher, J., and Conrad, R., Streptomycetes contributing to atmospheric molecular hydro- gen soil uptake are widespread and encode a putative high- affinity [NiFe]-hydrogenase, Environ. Microbiol., 12: 821–829. doi:10.1111/j.1462-2920.2009.02130.x, 2010.

De Wit, J. C., van der Straten, C. M., and Mook, W. G.: Determination of the absolute hydrogen isotopic ratio of V-SMOW and SLAP, Geostandards Newsletter, 4 (1), 33-36, doi: 10.1111/j.1751-908X. 1980.tb00270.x, 1980.

Ehhalt, D. H. 1966. Tritium and deuterium in atmospheric hydrogen. *Tellus* **18**, 249–255.

Ehhalt D H, Schmidt U, Heidt L E. Vertical profiles of molecular hydrogen in the troposphere and stratosphere[J]. Journal of Geophysical Research, 1977, 82(37): 5907-5911.

Ehhalt, D. H. and Rohrer, F.: The tropospheric cycle of H2: a critical review, Tellus B, **61** (3), 500–535, doi:10.1111/j.1600-0889.2009.00416.x, 2009.

Ehhalt D H, Rohrer F. The dependence of soil H2 uptake on temperature and moisture: a reanalysis of laboratory data[J]. Tellus B, 2011, 63(5): 1040-1051.

Friedman, I. and Scholz, T. G. 1974. Isotopic composition Of atmospheric hydrogen, 1967–1969. *J. Geophys. Res.* **79**, 785– 788.

Gerst S, Quay P. The deuterium content of atmospheric molecular hydrogen: Method and initial measurements[J]. Journal of Geophysical Research: Atmospheres (1984–2012), 2000, 105(D21): 26433-26445.

Gerst S, Quay P. Deuterium component of the global molecular hydrogen cycle[J]. Journal of Geophysical Research: Atmospheres (1984–2012), 2001, 106(D5): 5021-5031.

Grenier, N.P., Hydroxyl radical kinetics by kinetic spectroscopy, V, Reactions with H2 and CO in the range 300-500 °K, J. Chem. Phys., 51, 5049-5051, 1969.

Gonfiantini, R., Stichler, W., and Rozanski, K.: Standards and intercomparison materials distributed by the International Atomic Energy Agency for stable

isotope measurements, in: Reference and intercomparison materials for stable isotopes of light elements: Proceedings of a consultants meeting held in Vienna, 1-3 December 1993, IAEA-TECDOC-825, International Atomic Energy Agency, 1993.

Guo R, Conrad R. (2008). Extraction and characterization of soil hydrogenases oxidizing atmospheric hydrogen. Soil Biol Biochem 40: 1149–1154.

Hammer S, Levin I. Seasonal variation of the molecular hydrogen uptake by soils inferred from continuous atmospheric observations in Heidelberg, southwest Germany[J]. Tellus B, 2009, 61(3): 556-565.

Häring V, Klüber H D, Conrad R. Localization of atmospheric H2-oxidizing soil hydrogenases in different particle fractions of soil[J]. Biology and fertility of soils, 1994, 18(2): 109-114.

Hauglustaine D A, Ehhalt D H. A three-dimensional model of molecular hydrogen in the troposphere[J]. Journal of Geophysical Research: Atmospheres (1984–2012), 2002, 107(D17): ACH 4-1-ACH 4-16.

Haumann, F. A., Batenburg, A. M., Pieterse, G., Gerbig, C., Krol, M. C., and Röckmann, T.: Emission ratio and isotopic signatures of molecular hydrogen emissions from tropical biomass burning, Atmos. Chem. Phys. Discuss., 13, 11213-11245, doi:10.5194/acpd-13-11213-2013, 2013.

Heij, G. J., and J. W. Erisman. 1997. Acid atmospheric deposition and its effects on terrestrial ecosystems in The Netherlands. The third and final phase (1991-1995). Studies in Environmental Science, Vol. 69. Amsterdam, The Netherlands: Elsevier Science.

Hoefs J. Stable isotope geochemistry[M]. Springer, 2009.

Holloway J R, O'DAY P A. Production of CO2 and H2 by diking-eruptive events at mid-ocean ridges: Implications for abiotic organic synthesis and global geochemical cycling[J]. International Geology Review, 2000, 42(8): 673-683.

IPCC, 2007: Climate Change 2007: The Physical Science Basis. Contribution of Working Group I to the Fourth Assessment Report of the Intergovernmental Panel on Climate Change [Solomon, S., D. Qin, M. Manning, Z. Chen, M. Marquis, K.B. Averyt, M. Tignor and H.L. Miller (eds.)]. Cambridge University Press, Cambridge, United Kingdom and New York, NY, USA, 996 pp.

Jacobsen, M. Z., Colella, W. G., and Golden, D. M.: Cleaning the air and improving health with hydrogen fuel-cell vehicles, Science, 308, 1901-1905, doi: 10.1126/science.1109157, 2005.

Jacobsen, M. Z.: Effects of wind-powered hydrogen fuel cell vehicles on stratospheric ozone and global climate, Geophys. Res. Lett., 35 (L19803), doi: 10.1029/2008GL035102, 2008.

Jager C. J., T. C. Nakken and C. L. Palland (1976). Bodemkundig onderzoek van twee graslandpercelen nabij Cabauw. N.V.Heidemaatschappij beheer, Arnhem, maart 1976. (In Dutch)

Jordan, A. and Steinberg, B.: Calibration of atmospheric hydrogen measurements, Atmos. Meas. Tech., **4**, 509–521, doi:10.5194/amt-4-509-2011, 2011.

Lee, H., Rahn, T., and Throop, H. L.: A novel source of atmospheric H_2: abiotic degradation of organic material, Biogeosciences Discuss., 9, 8641-8662, doi:10.5194/bgd-9-8641-2012, 2012.

Novelli, P. C., Lang, P. M., Masarie, K. A., Hurst, D. F., Myers, R. and co-authors. 1999. Molecular hydrogen in the troposphere: global distribution and budget. J. Geophys. Res. **104**, 30 427–30 444.

Ogden J M. Prospects for building a hydrogen energy infrastructure[J]. Annual Review of Energy and the Environment, 1999, 24(1): 227-279.

Petrenko V V, Martinerie P, Novelli P, et al. A 60-yr record of atmospheric carbon monoxide reconstructed from Greenland firn air [J]. Atmos. Chem. Phys. Discuss, 2012, 12: 18993-19037.

Pieterse G, Krol M C, Batenburg A M, et al. Global modelling of H2 mixing ratios and isotopic compositions with the TM5 model[J]. Atmos. Chem. Phys, 2011, 11(14): 7001-7026.

Price, H., Jaegle, L., Rice, A., Quay, P., Novelli, P. C. and co-authors. 2007. Global budget of molecular hydrogen and its deuterium content: constraints from ground station, cruise, and aircraft observations. J. Geophys Res. **112**, D22108, doi:10.1029/2006JD008152.

Popa, M. E., Vermeulen, A. T., van den Bulk, W. C. M., Jongejan, P. A. C., Batenburg, A. M., Zahorowski, W., and Röckmann, T.: H2 vertical profiles in the continental boundary layer: measurements at the Cabauw tall tower in the Netherlands, Atmos. Chem. Phys., **11**, 6425–6443, doi:10.5194/acp-11-6425-2011, 2011.

Rahn, T., Kitchen, N., and Eiler, J. M.: D/H ratios of atmospheric H2 in urban air: Results using new methods for analysis of nano- molar H2 samples, Geochim. Cosmochim. Acta, 66, 2475–2481, 2002.

Rahn, T., Eiler, J. M., Boering, K. A., Wennberg, P. O., McCarthy, M. C. and co-author. 2003. Extreme deuterium enrichment in stratospheric hydrogen and the global atmospheric budget of H2. Nature **424**, 918– 921.

Rhee T S, Mak J, Röckmann T, et al. Continuous‐flow isotope analysis of the deuterium/hydrogen ratio in atmospheric hydrogen[J]. Rapid communications in mass spectrometry, 2004, 18(3): 299-306.

Rhee, T. S., Brenninkmeijer, C. A. M. and Röckmann, T. 2006a. The overwhelming role of soils in the global atmospheric hydrogen cycle. Atmos. Chem. Phys. **6**, 1611–1625.

Rhee, T. S., Brenninkmeijer, C. A. M., Braß, M. and Bru¨hl, C. 2006b. Isotopic composition of H2 from CH4 oxidation in the stratosphere and the troposphere. J. Geophys, Res. **111**, D23303, doi:10.1029/2005JD006760.

Rice A, Dayalu A, Quay P, et al. Isotopic fractionation during soil uptake of atmospheric hydrogen[J]. Biogeosciences, 2011, 8(3): 763-769.

Röckmann, T., Rhee, T. S., and Engel, A.: Heavy hydrogen in the stratosphere, Atmos. Chem. Phys., **3**, 2015–2023, doi:10.5194/acpd-3-3745-2003, 2003

Röckmann, T., Álvarez, C. X., Walter, S., van der Veen, C., , Wollny, A. G., Gun- the, S. S., Helas, G., Pöschl, U., Keppler, F., Greule, M., and Brand, W. A.: Iso- topic composition of H2 from wood burning: Dependency on combustion efficiency, moisture content, and δD of local precipitation, J. Geophys. Res., **115** (D17308), doi: 10.1029/2009JD013188, 2010.

Sander S P, Golden D M, Kurylo M J, et al. Chemical kinetics and photochemical data for use in atmospheric studies evaluation number 15[J]. 2006.

Sato, M., & McGee, K. A. (1981). Continuous monitoring of hydrogen on the south flank of Mount St. Helens. US Geol. Surv. Prof. Pap, 1250, 209-219.

Schmidt, U., Molecular hydrogen in the atmosphere, Tellus, 56, 78-90, 1974.

Schmidt U. The latitudinal and vertical distribution of molecular hydrogen in the troposphere[J]. Journal of Geophysical Research: Oceans (1978–2012), 1978, 83(C2): 941-946.

Schuler, S. and Conrad, R. 1990. Soils contain two different activities for oxidation of hydrogen. FEMS Microbiol. Ecol. **73**, 77–84.

Schultz, M. G., T. Diehl, G. P. Brasseur, and W. Zittel (2003), Air pollution and climate-forcing impacts of a global hydrogen economy, Science, 302, 624 – 627.

Simmonds P G, Derwent R G, O'Doherty S, et al. Continuous high-frequency observations of hydrogen at the Mace Head baseline atmospheric monitoring station over the 1994–1998 period[J]. Journal of Geophysical Research: Atmospheres (1984–2012), 2000, 105(D10): 12105-12121.

Smith-Downey N V, Randerson J T, Eiler J M. Temperature and moisture dependence of soil H2 uptake measured in the laboratory[J]. Geophysical research letters, 2006, 33(14).

Smith-Downey N V, Randerson J T, Eiler J M. Molecular hydrogen uptake by soils in forest, desert, and marsh ecosystems in California[J]. Journal of Geophysical Research: Biogeosciences (2005–2012), 2008, 113(G3).

Tromp, T. K., Shia, R.-L., Allen, M., Eiler, J. M. and Yung, Y. L. 2003. Potential environmental impact of a hydrogen economy on the stratosphere. Science **300**, 1740–1742.

Vogel, B., Feck, T., Grooβ, J.-U., and Riese, M: Impact of a possible future global hydrogen economy on Arctic stratospheric ozone loss, Energy Environ. Sci., 5, 6445-6452, doi: 10.1039/c2ee03181g, 2012.

Vollmer, M. K., Walter, S., Mohn, J., Steinbacher, M., Bond, S. W., Röckmann, T., and Reimann, S.: Molecular hydrogen (H2) combustion emissions and their iso- tope (D/H) signatures from domestic heaters, diesel vehicle engines, waste inciner- ator plants, and biomass burning, Atmos. Chem. Phys., **12**, 6275–6289, doi:10.5194/ acp-12-6275-2012, 2012.

Walter S, Laukenmann S, Stams A J M, et al. The stable isotopic signature of biologically produced molecular hydrogen (H_2)[J]. Biogeosciences Discussions, 2011, 8: 12521-12541.

Warwick, N. J., S. Bekki, E. G. Nisbet, and J. A. Pyle (2004), Impact of a hydrogen economy on the stratosphere and troposphere studied in a 2-D model, Geophys. Res. Lett., 31, L05107, doi:10.1029/2003GL019224.

WMO, GAW Report No. 192 - WMO: Guidelines for the Measurement of Atmospheric Carbon Monoxide (WMO TD No. 1551), 49 pp, July 2010.

Wösten J. H. M., G. J. Veerman an J. Stolte (1994). Waterretentie- en doorlatendheidskarakteristieken van boven- en ondergronden in Nederland: Staringreeks. Vernieuwde uitgave 1994. Technisch Document 18, Wageningen. (In Dutch)

Xiao, X., Prinn, R. G., Simmonds, P. G., Steele, L. P., Novelli, P. C. and co-authors. 2007. Optimal estimation of the soil uptake of molec- ular hydrogen from the Advanced Global Atmospheric Gases Ex- periments and other measurements. J. Geophys. Res. **112**, D07303, doi:10.1029/2006JD007241.

Yashiro H, Sudo K, Yonemura S, et al. The impact of soil uptake on the global distribution of molecular hydrogen: chemical transport model simulation[J]. Atmos. Chem. Phys, 2011, 11: 6701-6719.

Yonemura, S., Kawashima, S. and Tsuruta, H. 1999. Continuous measurements of CO and H2 deposition velocities onto an andisol: uptakecontrol by soil moisture. Tellus **51B**, 688–700.

Yonemura, S., Yokozawa, M., Kawashima, S., and Tsuruta, H.: Model analysis of the influence of gas diffusivity in soil on CO and H2 uptake, Tellus 52B, 919–933, 2000.

Yver C E, Pison I C, Fortems-Cheiney A, et al. A new estimation of the recent tropospheric molecular hydrogen budget using atmospheric observations and variational inversion[J]. Atmospheric Chemistry and Physics, 2011, 11(7): 3375-3392.

Acknowledgement

I feel great to do my master in IMAU and take this fascinating master project under the supervision of Thomas and Elena. I want to say thank you to many people. Without your help and support, this project would definitely not progress that much and become that interesting.

A big big thank to Thomas and Elena for your guidance, care, inspiration and opportunities. I experienced "special" guidance from you; one "discourages" (not exactly) me and one encourages me; one makes me very stressful and one lets me release a bit the stress; one spends almost every working day (even non-working day) with me teaching me as much as possible patiently and one effectively uses his every single minute to guide me to the right way…I appreciate a lot this balance, and I benefit a lot from it. I know that you were trying to give me as more opportunities as possible to learn. As Thomas said, you will miss Elena someday. For sure I will miss all the moments all of us working and talking together.

I appreciate the help from Anneke, Carina, Michel and Henk on the measurements in the lab and samplings in Cabauw and Speuld. You teach me to use tools, hands and brain to operate and fix things. The hydrogen system was not always working well, and many thanks for your kindly communicating with it for me. The system looked very complicated to me at the beginning and I made quite some mistakes and break down things. It is the confidence you gave me that enables me to learn to understand it.

Many thanks to my classmates and all the IMAUers. You are always willing to help. I feel like studying and living in a big family where everything can be solved and I am not alone. I enjoy sharing the life in Holland with you. Sara is one of the members from this big family who encourages me and gives me a lot of advices on the studies and life. Thanks to Geert-Jan for giving me a lot of suggestions during my course studies and master project.

Thanks to Chris, Ravi, Dayla, Jenny, Wei Chen, Min, Ketian, Anthi, Ioanna, Mila, Yunus…for sharing your time in Utrecht with me. And, for the food…Ravi, I will never forget that you cooked for me everyday when I was preparing for the exams and working on the master project.

And many to thank in heart.